2009

Progressive Water-Oil Transition Zone Due to Transverse Mixing Near Wells

Shengkai Duan
Louisiana State University and Agricultural and Mechanical College, shengkane@yahoo.com

PROGRESSIVE WATER-OIL TRANSITION ZONE DUE TO TRANSVERSE MIXING NEAR WELLS

A Dissertation

Submitted to the Graduate Faculty of the
Louisiana State University and
Agricultural and Mechanical College
In partial fulfillment of the
Requirements for the degree of
Doctor of Philosophy

in

The Craft & Hawkins Department of Petroleum Engineering

By
Shengkai Duan
B.S., Xi'An Petroleum Institute, 1993
M.S., University of Louisiana at Lafayette, 2003
August; 2009

ACKNOWLEDGEMENTS

At this opportunity, the author wishes to express his most sincere gratitude and appreciation to Dr. Andrew K. Wojtanowicz, Professor of petroleum engineering, for his valuable guidance and genuine interest as research advisor and chairman of the examination committee. He provided me with many technical skills in analyzing and problem-solving.

Deep appreciation is extended to Dr. Christopher D. White, for his great ideas and encouragements. I also want to thank other members of the committee, Dr. Julius Langlinais and Dr. Richard Hughes for their support and constructive suggestions; Dr. Mayank Tyagi and Dr. Jerzy Stopa (AGH University of Science and Technology of Poland) gave me valuable discussions on mathematical models. Great appreciation is extended to Darryl Bourgoyne and Gerry Masterman for all of their technical assistance during fabricating and running the experiments. Special thanks are also extended to the Petroleum Engineering faculty and staff for their help.

I want to thank my friends Bobby Kurniawan, Subhash Kalla, and other graduate students of the department for their friendship. The author also thanks the Louisiana Board of Regents for providing the sponsorship that made this research possible.

The author expresses his outmost gratitude to his wife Xin Li and his daughter Xindi (Cindy) Duan for their consistent love and encouragement over these five years.

Finally, the work is dedicated to my parents, Hongyi Duan and Sumei He, and my brother, Yingsheng Duan, for their unconditional love and patience.

TABLE OF CONTENTS

ABSTRACT

This study derives from observations made in petroleum research and practices of chemical industry that efficient mixing takes place in segregated flow of immiscible fluids flow in granular packs and static mixers. A hypothesis was formulated that transverse mixing (TM) may occur in a segregated inflow of oil and water to wells resulting in a progressive transition zone, more water production, and reduced oil productivity. “Mixing” is broadly interpreted here to address the entire range of stirring, splitting, dispersion and diffusion processes between two fluids.

Initial study showed that a commercial reservoir simulator would not model any transition zone in the segregated oil-water flow (at high pressure gradient) as it lacks a mathematical description of the phenomenon. Initial analysis identified two effects that may contribute to TM: shear mixing due to velocity contrast and momentum transfer due to tortuosity and stream collisions.

The shear mixing effect has been studied in a Hele-Shaw (H-S) flow cell, and water fingering and scattered water blobs in the form of waves are observed. However, the instability observed in these experiments may not be directly applicable to any real porous media due to the much larger vertical dimension of the Hele-Shaw cell as compared to the gap.

The momentum transfer (collision) effect has been studied by considering criteria for inertial force resulting from tortuous flow at grains and gravity force. TM criterion has been developed using modified Richardson number.

Only early TM has been confirmed with granular-pack flow cell experiments due to dimensional restrictions. The results showed only water invading oil layer above the initial water/oil interface. Also, TM increased for higher pressure gradients and larger grain sizes and reduced for more viscous oil.

A mathematical model of early TM has been derived by solving a diffusion equation with a constant flow velocity and constant water saturation (S_{wooi}) at the initial W/O interface. The model would reasonably match experimental results thus enabling determination of the transverse dispersion coefficient – similar to miscible dispersion – appeared to be proportional to the average flow velocity.

The TM effect in wells was qualified by converting the linear TM model to radial flow model and integrating within the well's inflow zone. The results showed TM would increase water production by 2.5%, and reduce oil rate by 8.3% thus reducing well's productivity.

Limitations and shortcoming of the study are discussed together with recommendations for future research.

CHAPTER 1

INTRODUCTION

1.1 Background, Observations, and Motivation

According to the recent statistics (Seright *et al*, 2003), more than seven barrels of water are produced for each barrel of oil in the United States on average. Worldwide, an average of three barrels of water is produced for each barrel of oil. The annual cost of disposing water is estimated to be $5-10 billion for the United States and approximately $40 billion worldwide. Production and research data have shown that most water is produced from the transition zone where water and oil inflow to wells concurrently (Reed and Wheatley, 1984 and Duan and Wojtanowicz, 2006). Therefore, in order to improve oil recovery, it is important to study mechanisms producing transition zone in the vicinity of a wellbore.

Static transition zone exists with no flow as a result of capillary pressure (Dake, 2002). A dynamic transition zone develops in two-phase frontal displacement flow across its interface, when viscous and inertial forces are significant, for instance, crossflow due to permeability difference (Katz and Tek, 1961). However, dynamic transition zone caused by mechanical mixing has been little studied to date (Duan and Wojtanowicz, 2008).

In the chemical industry, Jaszczur *et al* (2005) and Brye O. and Sawley M. (1998) reported that a segregated two-phase flow would become mixed after flowing through a static mixer, because the mixer has the internal structure which changes the flow path of the two fluids. In the oil industry, Perkins and Johnston (1969) observed a symmetrical mixing zone above and below oil and water (W/O) interface in a linear, granular-pack flow cell. Theoretically, the mixing mechanism in porous media should be similar to that in static mixers.

In this work the experiments reported by Perkins, have been modeled using the same properties of rocks and fluids and a commercial simulator. The results showed absence of any transition zone reported by Perkins. The only possible explanation was that commercial simulators do not model the mechanical mixing effect. Therefore, the motivation of this research was to identify factors causing transverse mixing, verify the transverse mixing effect experimentally, analyze distribution of fluid saturation, and assess the effect on well productivity.

1.2 Hypothesis

Based on the experimental observations and reservoir simulations, it is presumed in this work that the size of transition zones close to wells is larger than that away from the wells because of higher fluid flow velocity near wellbores. Also, the transition zone expansion at wells is not modeled by current commercial numerical simulators because it results from physical mechanism not included in the simulators. These two hypothetical mechanisms are the shear effect and momentum transfer and they are caused by the unbalanced capillary, gravity, shear, and inertial force. Also, on macroscopic scale, other factors, such as formation's heterogeneity, permeability, and pressure difference, may lead to transverse mixing as well.

1.3 Objective and Methods

The main objective is to verify the existence of transverse mixing phenomenon by physical experiments, derive a model and criteria for analyzing the results, evaluate the intensity of mixing effect, and qualify the possible reduction of oil well productivity resulting from the effect.

The major methods used in this research include:

- Physical experiments:

- Hele-Shaw experiments: identify the contribution of shear effect on the water oil interface to transverse mixing.
- Granular-pack flow model: verify transverse mixing and determine the immiscible transverse dispersion coefficient.

- Analytical modeling to quantify immiscible dispersion effect.
- Numerical simulation coupled with analytical model to assess the effect of transverse mixing on well productivity.
- Mixing criteria: investigate mixing zone size near the wellbore.

1.4 Dissertation Outline and Logic

This dissertation is organized in ten chapters, where the first chapter explains the reason for undertaking this study, its objective and approach. Chapter 2 presents a literature research to identify controlling factors of transverse mixing. It includes reviews of interfacial instability due to shear effects, pore scale collision effects, and the non-Darcy effect. It also tackles the miscible dispersion, mathematical models, and experiments.

Chapter 3 presents interfacial stability experiments with constrained segregated water oil flow with no grain collision using a Hele-Shaw model. Continuous waves along the interface result from perturbations caused by the shear force, caused by the velocities difference of the fluids.

In Chapter 4, I attempted to establish criteria for mixing zone near a wellbore. Reynolds, Richardson and Weber numbers and Forchheimer's equations are applied to analyze the mixing zone. The criteria are used to compute the size of the transition zone.

Chapter 5 introduces a physical model of flow in granular-packed cell. It describes the model design and testing procedures. It also presents experimental results on video tapes and still photographs. The data gives a qualitative description of the phenomenon.

Chapter 6 derives a macroscopic mathematical model describing transverse mixing. The transverse dispersion coefficient (D_T) can be determined using the model for a constant flow velocity and constant water saturation (S_{wooi}) at the initial W/O interface. The analytical solution is also used to predict saturation profiles for various cases using the computed D_T.

In Chapter 7, experimental results are analyzed quantitatively by considering effects of velocities, viscosities, and size of grains and computing dispersion coefficient. The correlations plots show linear relationships between dispersion coefficient and velocity, and pseudo-dispersivity and grain size.

Chapter 8 gives a procedure for sizing the incremental transition zone around a well by coupling the analytical model from Chapter 7 with a commercial simulator. The procedure gives an estimate of the well's oil rate reduction due to transverse mixing.

Chapter 9 summarizes the main conclusions of this study, and provides a critique, and recommendations for future research.

CHAPTER 2

LITERATURE REVIEW

Factors affecting unstable transverse mixing at the flowing water/oil interface, in porous media, are reviewed in this chapter. Theoretical and experimental work conducted by previous investigators has been reviewed.

Mechanisms of shear force causing transverse mixing at laterally-constrained, sharp oil/water interface (no capillary pressure) have been studied using the Hele-Shaw flow cells. At high velocities, interface instabilities were observed, similar to the Kelvin-Helmholtz (K-H) instability of free interface (Duan and Wojtanowicz, 2007, and Kundu, 1990). It seems, however, that porous media, with small pore throats and capillary forces acting on the fluids, should reduce the effects of the shear force.

In porous media, momentum transfer at an interface surface is influenced by capillary forces. Non-Darcy flow and collision effects may also influence the interface mixing.

Relative magnitude of different forces at the interface is critical for mixing, and this analysis shall involve dimensionless groups. Transverse mixing of immiscible fluids seems to follow the same theory as mechanical mixing of miscible fluids. Hence, prediction of transverse mixing may be accomplished using the same scaling analysis methods.

2.1 Transverse Mixing due to Shear Force

In the absence of capillary pressure, transverse mixing originates solely from interface instability. Many approaches to the instability analysis have been evaluated. Velocity, force potential and force are commonly used for stability evaluation (Smirnov *et al.*, 2005 and Bentsen, 1985). For the flowing fluids having free surface (very small capillary force), forces at

the interface including shear force, gravity, and inertial force are critical for crossing motion (Samara, 1961).

Physical experiments can be used to investigate mechanisms of unstable interface. A Hele-Shaw cell is considered to be analogous to the flow in a two-dimensional, porous medium. The Hele-Shaw cell consists of two-parallel plates, separated by a small gap conduit for horizontal flow (Hele-Shaw, 1898). The cell is used for viscous fluid flow in porous media study, because

(1) Streamlines and various flow patterns (*e.g.*, fingering, tracer diffusion) become visible through an injection of colored fluids into the gap between the plates,

(2) The gap between two horizontal plates is somewhat analogous to homogeneous, permeable strata. (In both systems, the fluids velocity is proportional to the pressure gradient. Greenkorn *et al.* (1964) showed that the Navier-Stokes equations provide a mathematical proof of the Hele-Shaw analogy to flow in porous media.)

Greenkorn *et al.* (1964) applied Hele-Shaw experiments to observe various phenomena occurring at the interface (He also used the model to study the different flow patterns in a heterogeneous formation). Later, Gondret *et al.* (1997) found that wave properties at the interface in a two-dimensional flow are affected by the gap size between the two plates. The smaller the gap size is, the more stable the interface becomes.

2.1.1 Shear Effect at Non-Viscous Fluids' Interface

To date, shear effect at two phases' interface has been mostly studied using one non-viscous fluid (gas) and one viscous fluid. The velocity gradient was so large that shear force could generate waves. Flows with high Reynolds numbers may trigger turbulence. This phenomenon is the well-known K-H instability (Figure 2.1). Four characteristics of instable surface can be summarized as follows (Kundu, 1990),

(1) Vortex lines move with the fluid.

(2) The strength of the vortex tube, or the circulation, is constant along its length.

(3) A vortex tube cannot end within the fluid.

(4) The strength of a vortex tube remains constant in time.

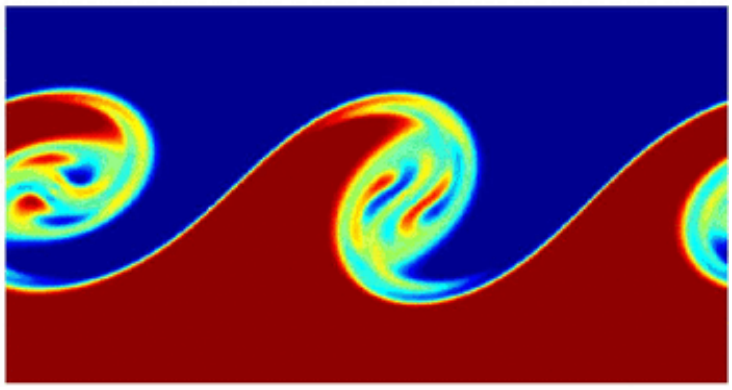

Figure 2.1 A computerized picture demonstrating K-H instability

(courtesy of Fringer, O. B. of Stanford University)

A perturbation originates from shear rate (τ) expressed as (Kundu, 1990)

$$\tau = \mu \frac{dv}{dz} \qquad \text{.....(2.1)}$$

Where, dz = distance between the two parallel faces that are experiencing the shear, [L]

The degree of instability may be evaluated with the gradient Richardson Number (R_i), which is (Kundu, 1990)

$$R_i = \frac{-\frac{g}{\bar{\rho}}\frac{d\bar{\rho}}{dz}}{(\frac{dv}{dz})^2} \qquad \text{.....(2.2)}$$

If the shear rate ($\frac{dv}{dz}$) is large enough, the modified Richardson number may drop below its stable value of ¼ and the K-H billows occur. The shear force resulting from the shear rate forms more unstable wavelengths into billows (*i.e.* large waves of water). At smaller values of

shear rate, gravity stratification would prevent disturbances from growing and the billows would disappear. Thus, high Richardson number (above 1/4) induces strong stratification and weak susceptibility to shear instabilities, while low Richardson number (below 1/4) means weak stratification and strong shear instabilities.

The wavelength of a stable wave can be calculated from the linear K-H theory as

$$\lambda = \frac{2\pi}{\frac{(\rho_1^2 - \rho_2^2)g}{\rho_1 \rho_2 (v_1 - v_2)^2}} \quad \text{.....(2.3)}$$

It is obvious that if the fluids, velocity difference $(v_1 - v_2)$ decreases, the wavelength will become shorter, and the interface would become more stable.

2.1.2 Shear Effect at Two Viscous Fluids' Interface

For two viscous fluids, the interface may become unstable by shear force resulting from velocity contrast that would depend upon the viscosity contrast. Moreover, in contrast to non-viscous fluids, interfacial tension between two immiscible viscous fluids may affect the stability of interface. Therefore, the K-H theory cannot apply directly to two viscous fluids without modifications.

If inertial force is larger than interfacial force, separated globules may form, which may cause the potential wave become discrete. Weber number is defined as the relative magnitudes of inertial force and surface tension of a fluid (Bear, 1972)

$$W_e = \frac{\rho(\Delta v)^2 d_p}{\sigma} \quad \text{.....(2.4)}$$

Where, d_p =diameter of particle, cm

Δv = velocity difference between water and oil, cm/s

ρ= density of water, g/cm^3

σ = fluid interfacial tension, dynes/cm

2.2 Transverse Mixing due to Momentum Transfer

Transverse mixing is applied in chemical industry. Segregated two-phase fluids can be completely mixed in static mixers (Figure 2.2). The static mixer has non-moving parts but is composed of complicated internal structure. Fluid collision and momentum transfer are major factor resulting in mixing.

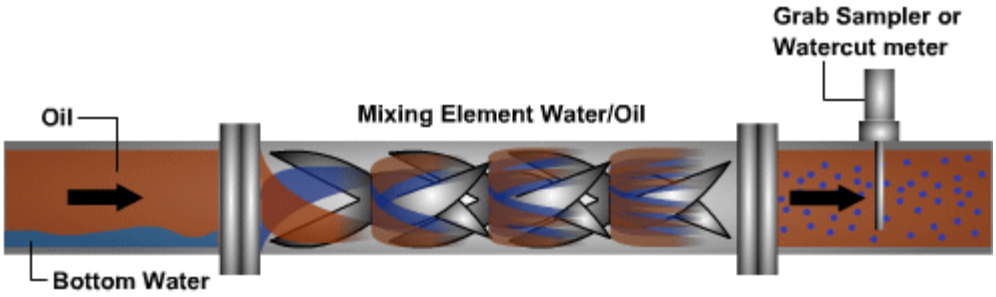

Figure 2.2 Schematic of water and oil interface change through a static mixer ("A typical application mixing crude and water into a homogeneous mixture"- simulation of mixed fluid at outlet of pipelines, EESIFLO)

In porous media, flow streams could diverge and converge following the tortuous flow path. Inertial forces resulting from these streams' momentum change should be estimated to describe transverse mixing. The relation of inertial force to other forces can be computed using dimensionless numbers.

The commonly known Richardson number (other than modified number in Eq. 2.2) is used to compute the ratio of inertial and gravity forces in the system (Bird *et al.*, 2001).

$$R_i = \frac{gh}{v^2} \qquad \text{.....(2.5)}$$

In pore throats, the Reynolds number calculates the ratio of inertial and viscous forces, which shows the intensity of inertial effect in viscous flow.

$$R_e = \frac{\rho v d}{\mu} \qquad \text{.....(2.6)}$$

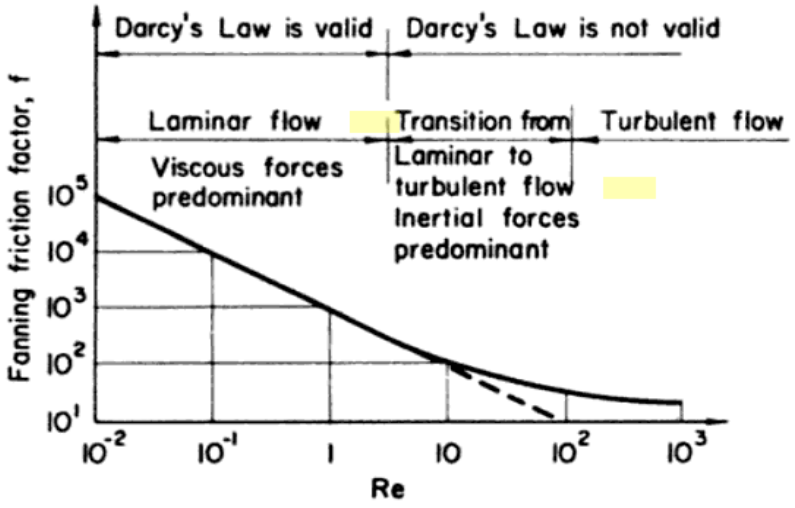

Figure 2.3 Schematic classification of flow through porous media
(After Bear, "Dynamics of Fluids in Porous Media", 1972)

From Figure 2.3, when Reynolds Number is greater than 10, the non-linear relationship between pressures drop and velocity should be considered, such as non-Darcy flow. Turbulent flow in porous media occurs when Reynolds number is larger than 100. Therefore, the inertial forces caused by high velocity should be the key factor in transverse mixing.

2.2.1 Transverse Dispersion in Two-Phase Flow

Kumar and Lake (1994) suggested that transverse dispersion is an important phenomenon in miscible displacement, slug processes, and gravity segregation. It is a macroscopic mixing caused by uneven concurrent laminar flow in fixed beds of real media (Niemann *et al.*, 1986). Perkins and Johnston (1969) also stated that stream splitting with mass transfer is a major phenomenon. It is expected that immiscible transverse dispersion may result from similar mechanisms in term of flow collision at grains (Figure 2.4). The angle and moment of fluids impinging on grains are different for the two fluids. Hence, analyzing the mechanism of transverse dispersion at the pore scale may be important.

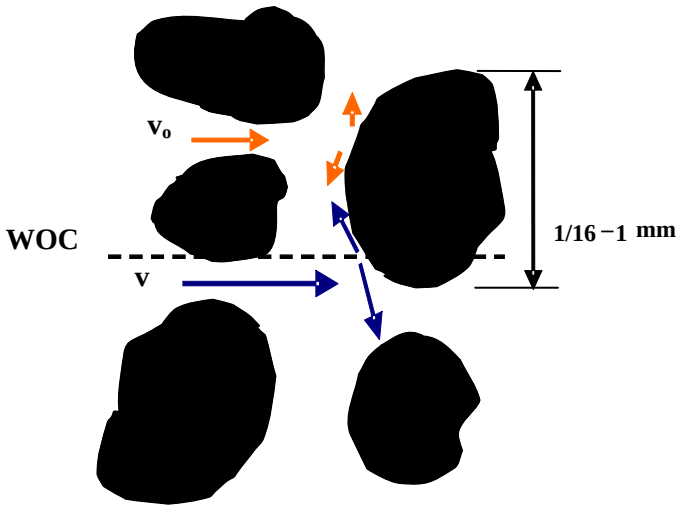

Figure 2.4 Fluid impinging upon a grain

Perkins and Johnston (1969) reported from their experiments that transverse dispersion of water reduces oil flow. A globule of water might become isolated from the main water stream and dispersed into oil. They concluded that transverse mixing depends on flow distance, particle size, fluid velocity, and heterogeneity coefficient. They put six questions at the end of their paper addressing problems needed to be solved to better understand the vertical mixing phenomenon.

Analytical mechanistic analysis of transverse mixing in Appendix C is partially based on the above theories.

2.2.2 Non-Darcy Effect

Laminar flow becomes unstable when a single phase flows at high velocity. The linear (Darcy) relationship between pressure drop and velocity cannot describe fluid flow and is replaced with the Forchheimer equation (Forchheimer, 1901).

$$\frac{\partial p}{\partial x} = \frac{\mu}{k} v + \beta \rho v^2 \quad \text{.....(2.7)}$$

In the equation (2.7), the non-Darcy coefficient (β) is related to inertia and computed by theoretical and empirical correlations (Li and Engler, 2001). For the viscous non-Darcy flow in porous media, Reynolds number may be a very small value, smaller than unity. The size

restrictions and areal distributions of pores and throats are represented by tortuosity (a factor measuring flow path change), which has a linear relationship with non-Darcy coefficient. Since tortuosity may cause transverse mixing, then, we may presume that transverse mixing may be related to non-Darcy flow.

2.2.3 Cross Flow vs. Transverse Mixing

Cross flow involves a significant vertical flow between layers in a reservoir. The cross flow would cause a transition zone if the two layers are water and oil. Similar to the theoretical model of cross-flow (Katz and Tek, 1961), transverse mixing by momentum change may result in saturation changes across the interface. By this concept, the mixing could occur between two layers of fluids in a non-stratified medium (Perkins and Johnston, 1969). Generally, at high velocity, transverse mixing reduces non-uniformities or gradients in the structure of bulk flow. However, if capillary and gravity forces dominate the system, *i.e.*, the fluid flows at low velocity, the mixing does not occur. Several researchers have tried to explain hydrodynamic dispersion using this concept. Jha *et al.* (2006) noted, "Mixing results from velocity variations through throats and bodies, where the converging-diverging flow around sand grains causes the interface to stretch, split and rejoin."

2.2.4 Hydraulic Jump

The gravity potential is a key to find the transverse mixing range. The theory of hydraulic jump is considered to explain the mechanism of continuous mixing (Kundu, 1990). The hydraulic jump concept applies to large-scale flowing system. But in the pore scale, the conservation of energy theory is also applicable in considering capillary effects. The Froude number is defined as (Kundu, 1990)

$$F_r = \frac{v_{up}}{\sqrt{gH_{down}}} \quad \text{.....(2.8)}$$

A highly energized flow may transfer from supercritical (Fr >1) to subcritical (Fr <1) through a jump. Then, the dispersed water stream "jump" into the oil stream.

The height of jump in porous media (Eq. 2.9) may be derived from energy balance. We assume that a high capillary number exists during dispersion. Applying Bernoulli's equation (Batchelor, 1967) to the process, and assuming no lose of energy, we have:

$$\frac{p_{up}}{\rho g} + H_{up} + \frac{v_{up}^2}{2g} = \frac{p_{down}}{\rho g} + H_{down} + \frac{v_{down}^2}{2g} \quad \text{.....(2.9)}$$

Assuming: $p_{up} = p_{down}$ and $H_{up}=h_{up}/2$, and $H_{down}=h_{down}/2$, we have:

$$\frac{h_{up}}{2} + \frac{v_{up}^2}{2g} = \frac{h_{down}}{2} + \frac{v_{down}^2}{2g} \quad \text{.....(2.10)}$$

And the solution is,

$$h_{down} = \frac{1}{2}(-1 + \sqrt{1 + 8Fr_{up}^2})h_{up} \quad \text{.....(2.11)}$$

Where,

h_{up} = fluid depth before jump, ft

h_{down} = fluid depth after jump, ft

H_{up} = middle fluid depth before jump, ft

H_{down} = middle fluid depth after jump, ft

v_{up} = velocity before jump, ft/s

v_{down} = velocity after jump, ft/s

In summary, Fr >1 is a sufficient condition for a transverse mixing since it indicates that kinetic energy is more than potential energy. H_{down} may be estimated from the velocity at the mixing interface confined by the height in Eq. (2.11).

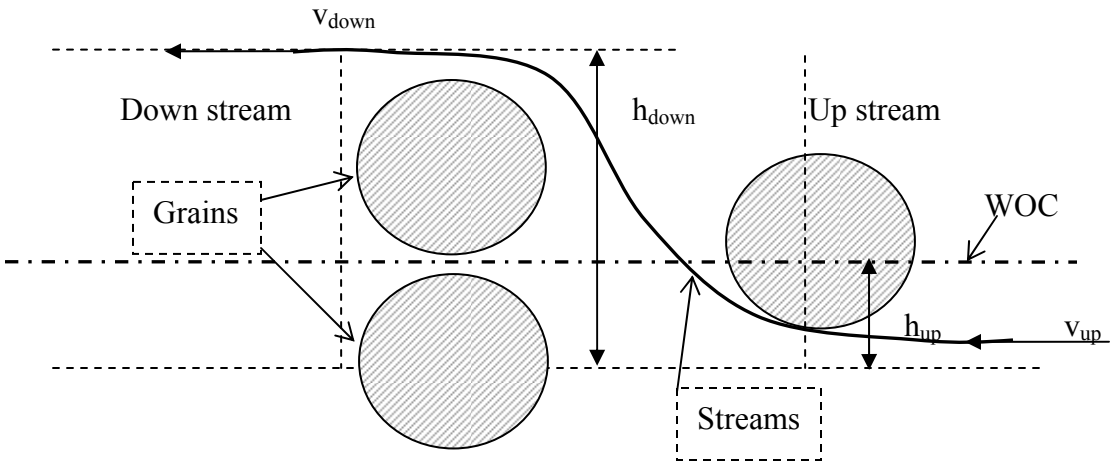

Figure 2.5 Sketch of the hydraulic jump

2.3 Miscible Transverse Dispersion Model

Diffusion is considered to be molecular transport mechanism between two miscible liquids (Lake, 1996). Diffusion is a slow process, so when the flow velocity is greater than diffusion velocity, dispersive flow dominates. The term "dispersion" is commonly used to feature mechanical aspects of the flow with drag forces, velocity, distances, etc. In the sense of mechanical dispersion, the mechanism of immiscible fluids is similar to that of miscible fluids (Perkins and Johnston, 1969).

To better understand the immiscible dispersion mechanism in porous media, several effects have been identified such as local velocity gradients, locally heterogeneous streamline lengths, and mechanical mixing (Lake, 1996 and CMG GEM Manual, 2006). These dispersion effects have been jointly described by a pseudo-mechanistic mathematical model of dispersion.

A general dispersion equation is

$$\frac{\partial C}{\partial t} = D_L \frac{\partial^2 C}{\partial x^2} + D_T \frac{\partial^2 C}{\partial x^2} - v\frac{\partial C}{\partial x} \quad \text{.....(2.12)}$$

Where, D_L = longitudinal dispersion coefficient, $[L^2/T]$

D_T = transverse dispersion coefficient, $[L^2/T]$

C = concentration

Since D_L has no effect on vertical concentration distribution in a segregated flow, the equation is simplified and has been solved by Perkins and Johnston (1963)

$$C = \frac{1}{2}[1 \pm \text{erf}(\frac{x}{2\sqrt{D_o t}})] \quad \text{.....(2.13)}$$

Where, D_o = molecular diffusion coefficient, $[L^2/T]$

For miscible fluids, the dispersion coefficient relates to diffusion coefficient as (Perkins and Johnston, 1969),

$$\frac{D_T}{D_o} = \frac{1}{F'\phi} + 0.0157\frac{\sigma' d_p v}{D_o} \quad \text{.....(2.14)}$$

Where, d_p = grain diameter, [L]

σ' = a measure of the heterogeneity of the porous pack

F' = formation electrical resistivity factor

Similarly, Lake and Hirasaki (1981) have simplified this equation for miscible fluids as,

$$D_T = \frac{D_o}{F'\phi} + \alpha_T v \quad \text{.....(2.15)}$$

Note that the second term in Eq. (2.15) is mechanical dispersion coefficient defined in fluid mechanics as:

$$D = \alpha v \quad \text{.....(2.16)}$$

Where, D = dispersion coefficient, $[L^2/T]$

α = dispersivity, [L]

v = velocity, [L/T]

2.4 Scaling Criteria for Transverse Mixing

Physical experiments are used to verify the theoretical results. In this research, we must design a physical flow model capable of simulating flow in the high-velocity zone near a

wellbore. Therefore, the physical model must generate flow conditions dominated by inertial and viscous forces. The scaling analysis below could be useful for designing the model parameters.

Dimensionless groups are applied to analyze force distribution in the flow. These groups can point to various limiting cases where one factor is clearly dominant over another. Systems with the same dimensionless groups will have the same dimensionless response. Zhou *et al.* (1997) suggested the following five dimensionless groups describing multiphase flow in porous media.

Gravity number: $N_{gv} = \frac{\Delta\rho g L k}{h_O Q \mu_o}$ ……(2.17)

Modified gravity number: $N_{gv} \frac{M}{1+M}$ ……(2.18)

Transverse capillary number: $N_{cv} = \frac{L p_c^* k}{h_o^2 Q \mu_o}$ ……...(2.19)

Threshold capillary pressure: $p_c^* = 4\sigma\cos\theta(\frac{c\phi}{k})^{1/2}$ ……(2.20)

Modified Transverse capillary number: $N_{cv} \frac{M}{1+M}$ ……..(2.21)

Where, $M = \frac{k_w}{\mu_w}\frac{\mu_o}{k_o}$

Since our experiment requires a viscous dominated flow condition, following the work of Zhou et al (1997) and based on Figure 2.6, we have,

$\frac{N_{gv} M}{1+M} < 0.1$ ……...(2.22)

$\frac{N_{cv} M}{1+M} < 0.1$ ……..(2.23)

Where,

c = constant depending on the medium, 0.02 for glass beads-packs

g = gravity acceleration factor, ft/s^2

h_o = thickness of oil layer, ft

L = flow length, ft

M = mobility ratio, dimensionless

Q = flow rate, ft^3

v = fluid velocity, cm/s

$\Delta\rho$ = density difference between oil and water, $10^3 kg/m^3$

θ = contact angle, degree

σ = interfacial tension, dyne/cm

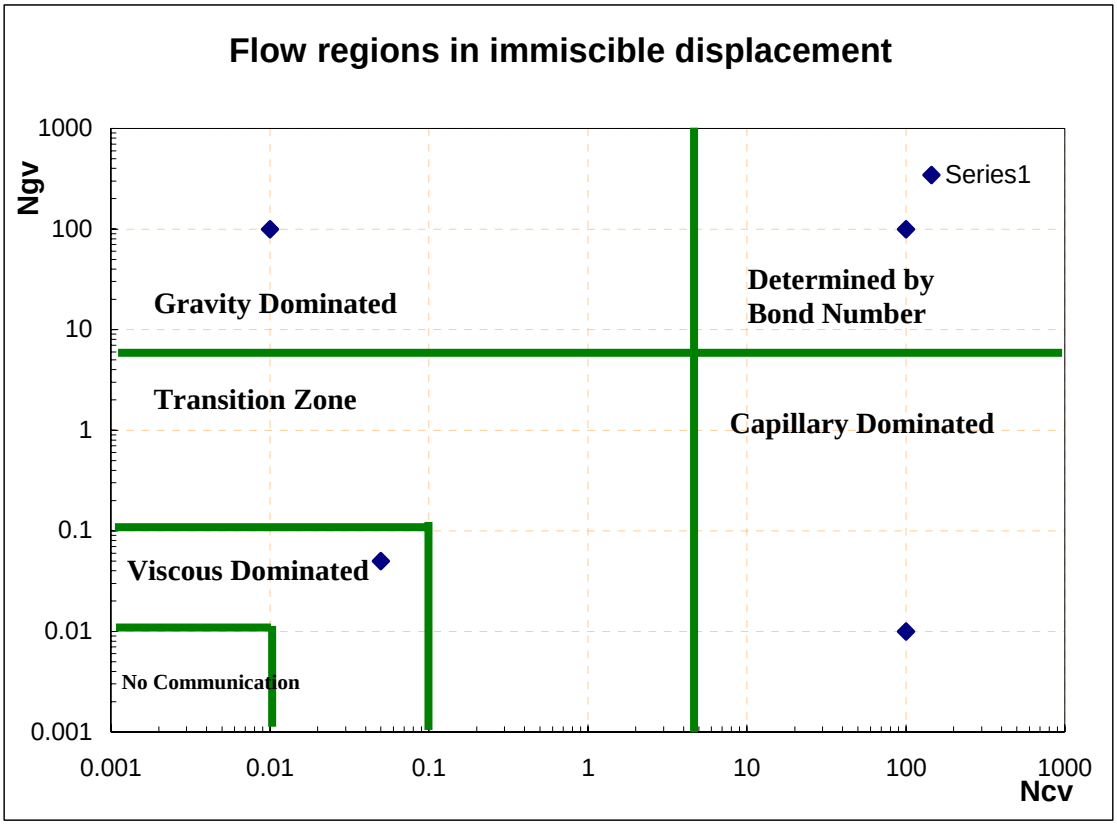

Figure 2.6 Different domination based on dimensionless analysis (Zhou et al, 1997)

Thus, the dimensions of our physical model (see Chapter 6) should give values of both terms in Eqs. 2.22 and 2.23 for oil and water smaller than 0.1.

2.5 Summary

1. The available literature suggests that interfacial instability and transverse mixing at the water/oil interface may result from shearing rate and momentum transfer. The latter effect is caused by tortuous flow path and collision at grains.
2. There is analogy between immiscible and miscible fluids in mechanical mixing; it is possible that transverse mixing may be analyzed using dispersion principles.
3. Dimensionless groups are useful for determining flow conditions dominated by inertial and viscous force. Also, possibly, criteria for transverse mixing may be defined using those groups.

CHAPTER 3

TRANSVERSE MIXING DUE TO INTERFACE INSTABILITY

In this chapter, the design, installation, and analysis of experiments with a Hele-Shaw (H-S) flow cell are reported. The objective of the experiments is to analyze a shear mixing process at the interface of two fluids (oil and water) flowing parallel to each other at different superficial velocities. The results show development of a mixing zone above the unstable interface. The zone comprises water globules dispersed into the oil layer as they separate from an unstable and wavy interface. Force balance in transverse direction shows that only gravity and viscous forces are major factors in the experiments as capillary mechanism is absent in the Hele-Shaw cell. In an actual oil field, the effect of transverse mixing demonstrated by the H-S cell could fully apply to the segregated two-phase flow in formations, with natural or hydraulic fractures producing oil and water with negligible capillary effect. Little information has been published in literatures on mixing of two vertically segregated, viscous fluids in a Hele-Shaw cell.

Capillary effect may become dominant when the gap between two plates reduces and the vertical space becomes the same size as the gap. Therefore, such interface stability of flow in porous medium affected by shear force should be reexamined with a granular flow cell. Hence, this study may be considered a complementary experiment in regard to instability as observed in the Hele-Shaw flow cell.

3.1 Hele-Shaw Experiments

3.1.1 Design of Key Parameters

Considering safety of the experiment, the highest flow velocity in the Hele-Shaw cell should be determined from the maximum pressure drop of 14 psi. Pressure gradient between inlets of outlet is expressed by

$$\frac{dp}{dl} = \frac{\mu v}{4000h^2} \quad \text{.....(3.1)}$$

For different viscous oils, are computed. Velocities and Reynolds number in (Eq. (3.2)) have been computed together with the required volume of liquids

$$N_{Re} = \frac{928\rho v d}{\mu} \quad \text{.....(3.2)}$$

All the parameters, properties, and results are listed in Tables 3.1 through 3.3;

Table 3.1 Parameters prediction for experimental design – 1
Mineral Oil Flow (1/2 height of the cell)

Case #	Geometry of experiment			Q	Δp/Δl	A	μ*	v	Time	Volume	N_{Re}	Pressure	SG*
	length(ft)	Height(ft)	width(ft)	(GPM)	(psi/ft)	(ft^2)	(cP)	(ft/s)	min	Gallon		psi	d.less
1-1	2.875	0.448	0.0009	0.003	1.11	0.0004	30	0.018	30	**0.1**	0.055	**3.2**	0.85
1-2	2.875	0.448	0.0009	0.005	1.67	0.0004	30	0.027	30	**0.2**	0.083	**4.8**	0.85
1-3	2.875	0.448	0.0009	0.007	2.45	0.0004	30	0.04	30	**0.2**	0.122	**7**	0.85
1-4	2.875	0.448	0.0009	0.008	2.79	0.0004	30	0.045	30	**0.3**	0.139	**8**	0.85
1-5	2.875	0.448	0.0009	0.013	4.46	0.0004	30	0.072	30	**0.4**	0.222	**12.8**	0.85
1-6	2.875	0.448	0.0009	0.015	4.88	0.0004	30	0.079	30	**0.4**	0.243	**14**	0.85

Table 3.2 Parameters prediction for experimental design – 2
Mixed Oil Flow (1/2 height of the cell)

Case #	Geometry of experiment			Q	Δp/Δl	A	μ*	v	Time	Volume	N_{Re}	Pressure	SG*
	length(ft)	Height(ft)	width(ft)	(GPM)	(psi/ft)	(ft^2)	(cP)	(ft/s)	min	Gallon		psi	d.less
2-1	2.875	0.448	0.0009	0.006	1.11	0.0004	17	0.032	30	**0.18**	0.173	**3.2**	0.85
2-2	2.875	0.448	0.0009	0.009	1.67	0.0004	17	0.048	30	**0.3**	0.259	**4.8**	0.85
2-3	2.875	0.448	0.0009	0.013	2.45	0.0004	17	0.07	30	**0.4**	0.38	**7**	0.85
2-4	2.875	0.448	0.0009	0.015	2.79	0.0004	17	0.08	30	**0.4**	0.431	**8**	0.85
2-5	2.875	0.448	0.0009	0.024	4.46	0.0004	17	0.127	30	**0.7**	0.69	**12.8**	0.85
2-6	2.875	0.448	0.0009	0.026	4.88	0.0004	17	0.14	30	**0.8**	0.756	**14**	0.85

Table 3.3 Parameters prediction for experimental design – 3
Water Flow (1/2 height of the cell)

Case #	Geometry of experiment			Q	Δp/Δl	A	μ*	v	Time	Volume	N_{Re}	Pressure	SG*
	length(ft)	Height(ft)	width(ft)	(GPM)	(psi/ft)	(ft^2)	(cP)	(ft/s)	min	Gallon		psi	d.less
3-1	2.875	0.448	0.0009	0.1	1.11	0.0004	0.8	0.54	30	**3**	49.9	**3.2**	1.01
3-2	2.875	0.448	0.0009	0.15	1.67	0.0004	0.8	0.81	30	**4.5**	74.8	**4.8**	1.01
3-3	2.875	0.448	0.0009	0.22	2.45	0.0004	0.8	1.19	30	**6.6**	109.7	**7**	1.01
3-4	2.875	0.448	0.0009	0.25	2.79	0.0004	0.8	1.35	30	**7.5**	124.7	**8**	1.01
3-5	2.875	0.448	0.0009	0.4	4.46	0.0004	0.8	2.17	30	**12**	199.4	**12.8**	1.01
3-6	2.875	0.448	0.0009	0.438	4.88	0.0004	0.8	2.37	30	**13.1**	218.4	**14**	1.01

*At room temperature - 70 F

From the calculation, the velocities have similar magnitude of the actual near-wellbore flow velocity (Duan and Wojtanowicz, 2007).

3.1.2 Properties of Working Fluids

Dyed water, mineral oil and Soltrol solutions of different viscosities are chosen for working fluids. The water is deionized and gas-free. At normal temperature and pressure conditions, the water is chemically inactive. Therefore, the dispersed water globules have constant density and viscosity anywhere and anytime. The outflow fluids from the cell are tested to assure complete separation and consistent properties.

3.2 Design of the Hele-Shaw Flow System

The system consists of a Hele-Shaw cell, tanks, pumps, and pipelines (Figure 3.1). Based on the results of separation time tests, the water-oil mixture does not have sufficient time to be separated in a closed system. Hence, an open flow system has been designed.

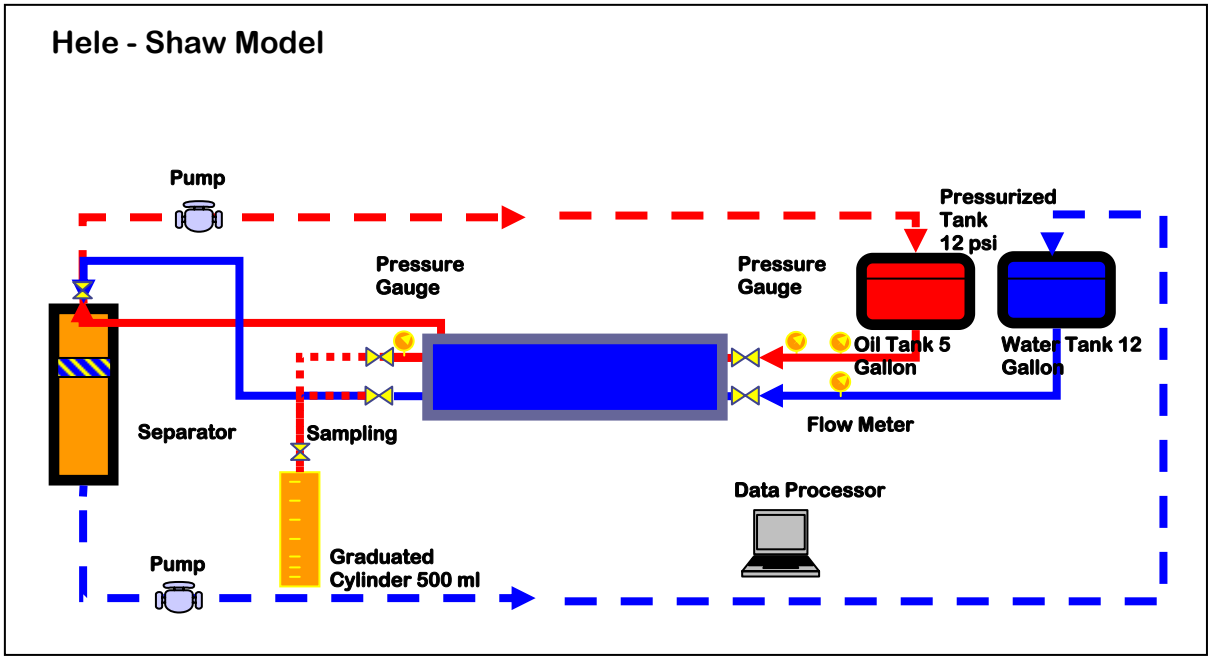

Figure 3.1 Schematic of fluid flow in Hele-Shaw system

Two utility transfer pumps were used for delivering the working fluids from the tanks to the cell as shown in Figure 3.1. Each pump has capacity of 6 gallons per minute and a 48-ft

hydraulic head. One half inch plastic pipes are used to reduce the restriction of the steel pipes at the 1-inch inlet. Two pressure gauges are installed at the ends of the cell to monitor pressure drawdown.

The Hele-Shaw cell is shown in Figure 3.2. Its dimensions are 2.875×0.9×0.001 ft (length/height/gap). The cell comprises two parallel glass plates at 0.28 mm gap designed to withstand 14 psi pressure. In flowing tests of different liquids, larger pressure drops were obtained comparing the computed value in Table (3.1 to 3.3) for the same flow rates. The reason is that the position of pressure gauge is not exactly at located at the ends of the cell, and pressure loss across the joint of the tube and gap of plates should be considered. A safety valve has been installed at the inlet so that inflow pressure limit can be solved.

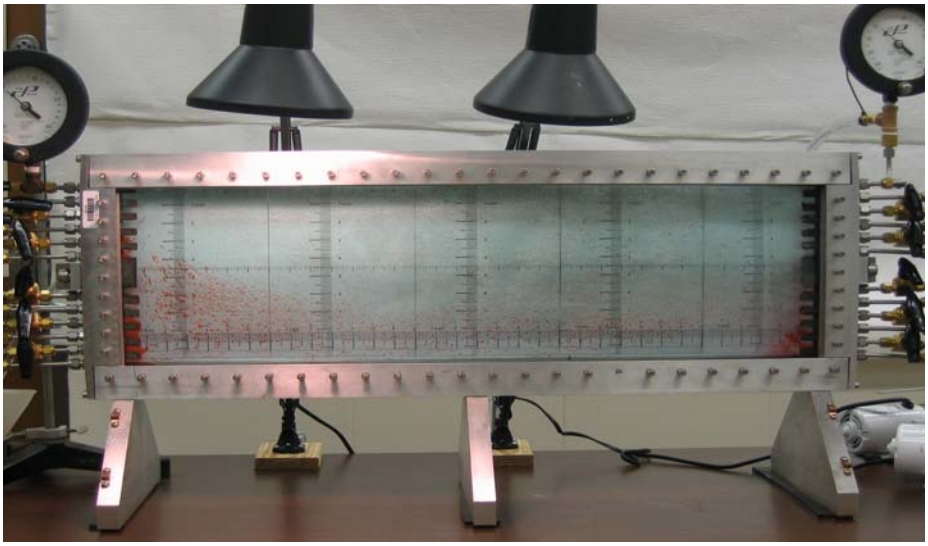

Figure 3.2 A picture of Hele-Shaw model

3.3 Testing Procedure

Each flow test (run) is performed using the following procedure:

1) Fill the cleaned and empty cell with oil;

2) Pump water slowly to fill the bottom half of the cell;

3) Check connections and valves for possible leakages;

4) Wait until horizontal oil/water interface stabilizes;

5) Open inlet valves, gradually increase the pump rate of oil and water using pre-determined volume; observe flow patterns change at the interface.

6) Measure the stabilized pressure, flow rate, and water content at the outlets.

7) Videotape the stabilized flow, and analyze the waves and scattered water blobs.

8) Repeat the run with the same oil viscosity or inlet pressure.

3.4 Analysis of Experimental Results

3.4.1 Stable Water Oil Interface at Low Flow Velocity

A stable interface (Figure 3.3) is observed when the water velocity is 0.05ft/s and oil velocity is 0.003 ft/s at the outlets. In this run the water/oil ratio is 17:1.

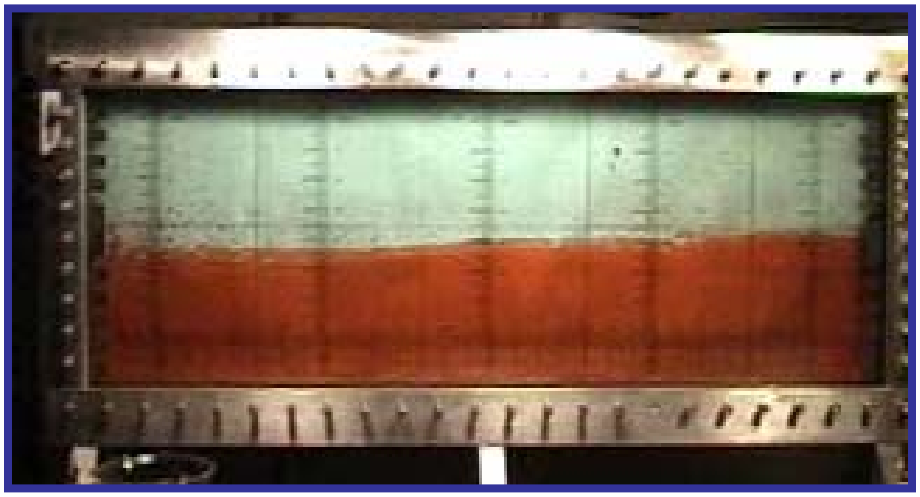

Figure 3.3 A stabilized water oil interface at low velocity – Run 3-1

A stable water-oil interface should be obtained at a static condition in the model. In this situation, Young's equation (Eq. 3.3) is applied assuming a capillary between the two slabs (Figure 3.4). The water oil interface is found at bottom oil and the top of the water. Gravity and interfacial tensions are the key factors influencing the stable conditions.

The forces at the interface are shown in Figure 3.5. In static condition,

$$\sigma_{wo}\cos\theta = \sigma_{wW} - \sigma_{oW} \quad \text{.....(3.3)}$$

Where,

θ = contact angle of water to wall, degree

σ_{wW} = interfacial tension at water and glass wall surface, dynes/cm

σ_{oW} = interfacial tension at oil and glass wall surface, dynes/cm

σ_{wo} = interfacial tension at water and oil surface, dynes/cm

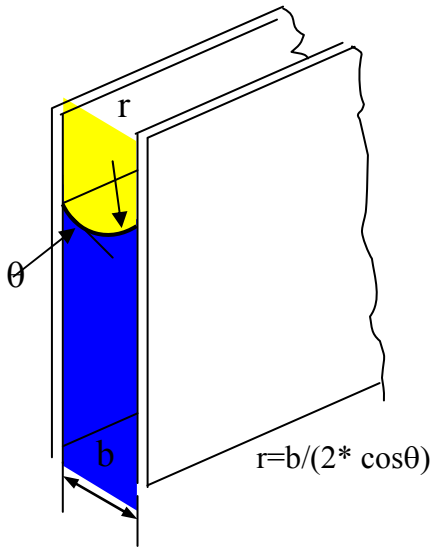

Figure 3.4 Interfacial tension of two fluids' between a slab

The gap between two plates equalizes the diameter of the curvature in capillary computation. The capillary pressure between the water and glass wall is (Bear, 1972)

$$p_{cwo} = \frac{2\sigma_{wo}\cos\theta}{r} \quad \text{.....(3.4)}$$

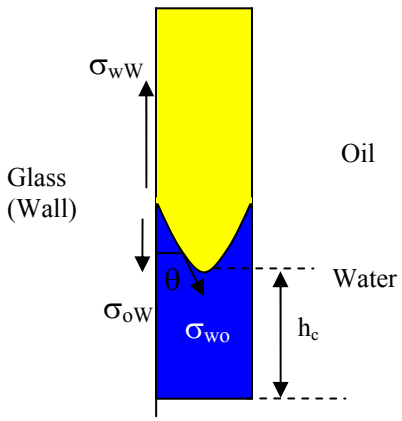

Figure 3.5 Stresses exerted on the fluid surface – cross-section view

If the interface stays static, then

$$p_{cwo} - \Delta\rho g h_c = 0 \quad \text{.....(3.5)}$$

Where, h_c, is the raised hydraulic height due to capillary pressure, cm

When fluids flow at relatively low velocity (Figure 3.6), the effect of shear force may not be neglected. Two more pressure components must be added to Eq. (3.5); they are the pressure difference across the interface and shear rates at interface.

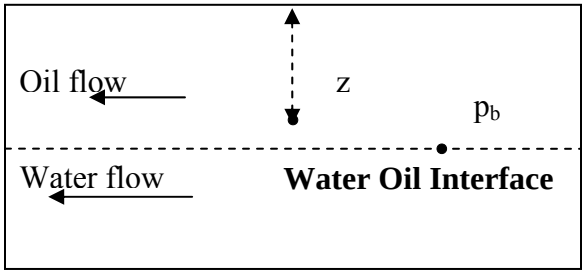

Figure 3.6 Potentials in a segregated flow

Bentsen (1985) stated that the potential of any fluid in any position is defined by

$$\Phi = gz\cos\alpha + \int_{p_b}^{p+p_c} \frac{dp}{\rho} \quad \text{.....(3.6)}$$

Where, z = a point above the interface

p_b = the static pressure at the interface, psi

In the Hele-Shaw flow experiments, the potential of water at W/O interface is

$$\Phi_w = (\Phi_w)_w + \frac{p_b + p_{wsW} + p_{sL}}{\rho_w} \quad \text{.....(3.7)}$$

Where, $(\Phi_w)_w$ = potential of water calculated by Darcy's Law

p_{wsW} = the shear force at the interface of the water and the glass wall, psi

p_{sL} = the shear force at the interface of the water and the oil, psi

The shear force at the interface of fluids can be calculated by the following equation

$$p_{sL} = \mu\gamma = \mu \frac{dv}{dL} \quad \text{.....(3.8)}$$

Where, μ = the viscosity, cp

γ = the shear rate, 1/s

L = the vertical distance of two velocity, cm

Similarly for oil stream, the potential of the oil at the W/O interface is

$$\Phi_o = (\Phi_o)_o + \frac{p_b + p_{osW}}{\rho_o} \quad \text{.....(3.9)}$$

p_{osW} = the shear force at the interface of the oil and the wall, psi

In the experiments, the pressure drop between inlets and outlets is always the same for water and oil flow. Hence, $(\Phi_o)_o$ is equal to $(\Phi_w)_w$. The differences between Eq. (3.9) and Eq. (3.7) are the shear forces, p_{sL} and difference of p_{wsW} and p_{osW}.

3.4.2 Unstable Water Oil Interface at High Flow Velocity

Fluid interface remains flat until it is perturbed by a growing shear force. When the velocity difference is large, it induces enough shear force to break the force balance at the interface. Small perturbations due to shear force at the interface will generate individual water fingers. Then, divergence of these fingers above the interface will develop into a series of waves. In other words, water fingers may invade into the oil layer where oil/water velocity difference is large enough. A series of tests were conducted to observe is instability. Pictures taken during the experiments indicate that the interface is perturbed in various ways.

3.4.2.1 Interface Behavior with High-Viscosity Oil

In experiments with viscous oil, the velocity of 30 cp oil has less than 0.01 ft/s in a pressure difference of 2 psi while the water velocity is 0.1 ft/s. Water fingering and dispersing to oil bulk flow is evident because water has higher mobility than the oil (Figure 3.7).

In this case, the interfacial tension of Soltrol to water is 32.8 dynes/cm (Soltrol Introduction manual), and the mineral oil to water is 52 dynes/cm (Mineral Oil Introduction manual). The value of the Weber number (Eq. 2.4) is 40. Weber number larger than 1 indicates that water could protrude from its bulk flow because the shear force is larger than the capillary force as mentioned in 2.1.2.

Figure 3.7 Interface Instability with high-viscosity oil – water fingering at interface – Run 3-2

Therefore, water fingers are observed above the original interface in Figure 3.7. The pressure difference in lateral flow may keep driving the split water fingers move forward. In the vertical direction, however, the shear force is not large enough to protrude water globules into a high viscous oil layer.

3.4.2.2 Interface Behavior with Low-Viscosity Oil

For lower viscosity oil, the velocity of 17-cp oil is less than 0.05 ft/s, while the water velocity is 0.8 ft/s. A perturbed interface is observed after a 15.5-inch flat flow. Once water waves form, water flow into oil bulk flow and expand in both the longitudinal and the transverse directions (Figure 3.8).

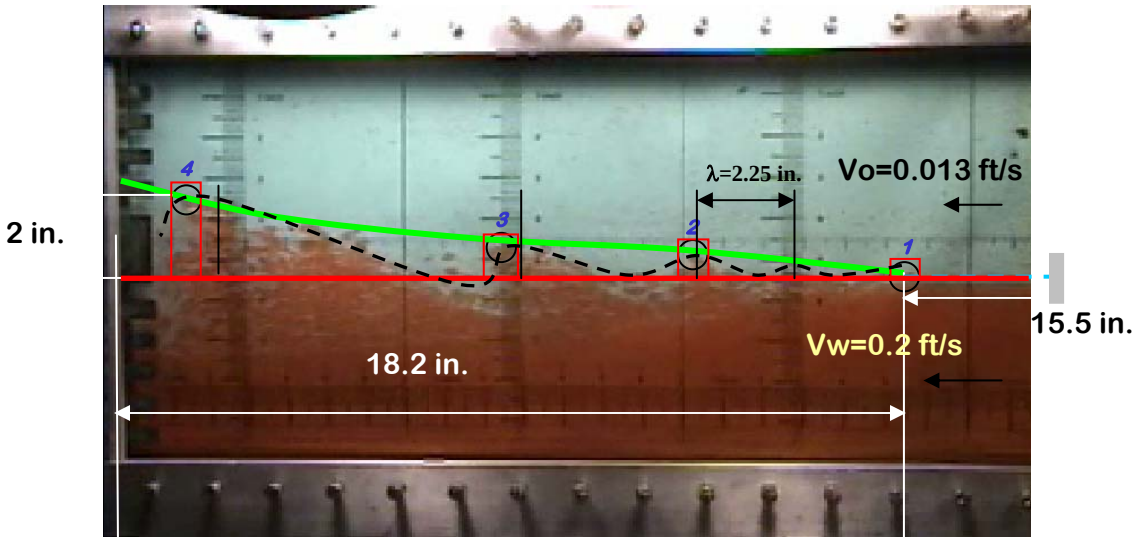

Figure 3.8 Instability in low viscous oil – wave along the interface – Run 3-3

Individual water blobs are released from the water waves due to shear force, and dispersed into the oil bulk flow. The wavelength increases along the flowpath.

In comparison of Figures 3.7 and 3.8, the properties of the waves (length, number, amplitude) are different. There is a trend of an increasing wavelength and amplitude with increasing velocity contrast.

A characteristic of unstable two phase interface is wave ratio (λ_a). It is a function of transverse and longitudinal velocities. This parameter is defined as the ratio of vertical difference of two waves' tips and their horizontal distance in Eq. (3.11).

$$\lambda_a = \frac{a_n - a_{n-1}}{x_n - x_{n-1}}, \text{ n=1, 2, …N} \quad \text{.....(3.11)}$$

Where, a = the wave's amplitude, in

x = the wave's horizontal position, in

N = integer value

Wave ratio has been computed with measured data shown in Figure 3.8 – Case 3-3. In this case, the farthest globules from the original interface represent the "tips" of the waves. All the measurements are listed in Table 3.4. The results show that the greater the wave ratio is, the

more intense the transverse mixing becomes (Table 3.4). This trend also indicates that instability of the interface would continue if the cell was longer.

Table 3.4 Wave ratio in Figure 3.8 – Case 3-3

Position	Height Difference between Two Tips of Waves (inch)	Horizontal Distance between Two Tips of Waves (inch)	Ratio of Vertical and Horizontal Displacement
3-4	1.2	8	0.15
2-3	0.5	5.5	0.09
1-2	0.2	4	0.05

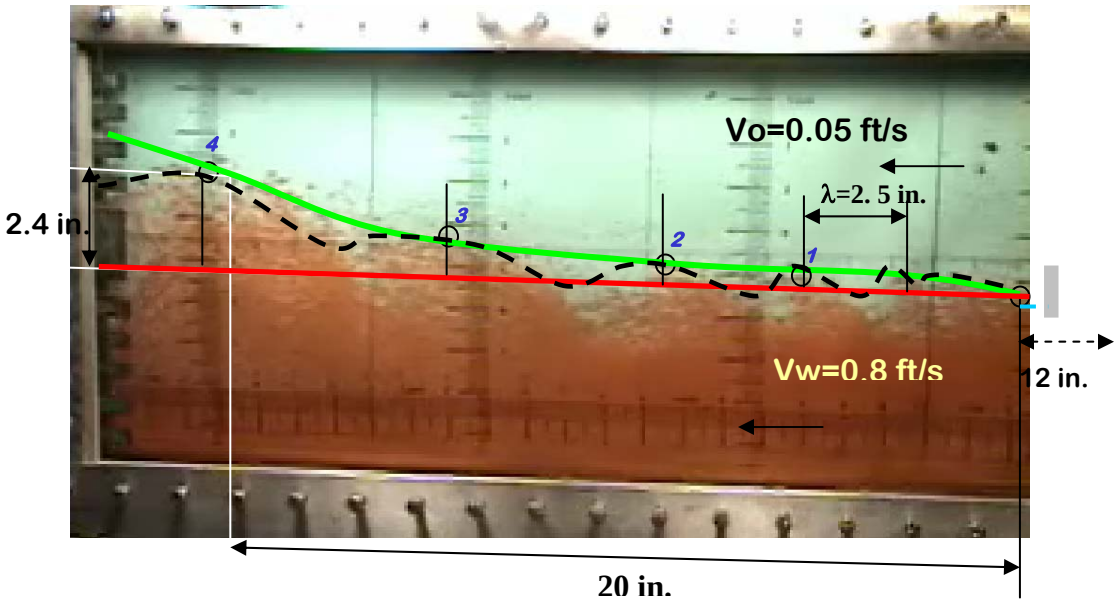

Figure 3.9 Waves after perturbation formed at high velocity – Run 3-4

Table 3.5 Wave ratio in Figure 3.9 – Case 3-4

Position	Height Difference between Two Tips of Waves (inch)	Horizontal Distance between Two Tips of Waves (inch)	Ratio of Vertical and Horizontal Displacement
3-4	1.1	6.5	0.17
2-3	0.5	5	0.10
1-2	0.2	3.5	0.06

In Case 3-4, the water flow velocity is increased from 0.2 to 0.8 ft/s. Comparing to the result for lower velocities, there is an increase of the ratio at higher velocity - as shown in Table

3.5. Evidently, at high velocity the fingering water has more momentum to transversely flow into the oil stream.

3.4.2.3 Perturbation due to Shear Rate

In the studies done by Meignin et al. (2000), with a Hele-Shaw model, an onset of perturbation was called an "instability threshold". The criterion was based on two parameters: ratio of shear force and interfacial tension, and Weber number.

As we know, the shear force can be calculated by the following equation (Bird, *et al.*, 2001)

$$F_s = \mu\gamma A = \mu \frac{dv}{dz} A \quad \text{.....(3.12)}$$

The force retaining the interfacial stability is interfacial tension; the force is expressed as (Bear, 1972)

$$F_c = \frac{2\sigma\cos\theta}{r} A_b \quad \text{.....(3.13)}$$

In Eqs. 3.12 and 3.13,Where, v = fluid's velocity, m/s

A = interface area of flow, m^2

A_b = area of blob, m^2

Table 3.6-1 The properties of fluids

Water viscosity	μ	0.8	cp
Flow area at stable interface	A	0.000084	m^2
Stable length	L	12	In
Interfacial tension	σ	32.8	dynes/cm
Radius of blob	R	0.00027	m
Area of blob	A_d	0.0000002	m^2
Density of blob	ρ_b	1	g/cm^3
Flow velocity	v	0.90	m/s
Velocity difference	Δu_b	0.73	m/s

Table 3.6-2 The calculation of Weber number

Shear force	F_s	0.000146	N
Capillary force	F_c	0.000057	N
Weber number	W_e	2032.15	

Interfacial instability occurs when $F_s > F_c$. As an example, let us consider properties of fluids listed in Table 3.6-1 and the calculated Weber number shown in table 3.6-2.

Note that the equality of W_e=1 is expected whenever the form of globules is restored (in Eq. 2.4). In this case, the inequality of W_e>>1 means that applied forces exceed the restoring forces formed by the surface tension. In experiments, scattered globules are observed in the unstable waves.

On the other hand, the Reynolds number is as following (Smith and Greenkorn, 1969)

$$R_e = \frac{\rho u_b d_g}{\mu} \quad \text{.....(3.14)}$$

Where, u_b = velocity of blob, m/s

μ = fluid's viscosity, cp

d_g = size of gap between the plates, mm

The flow regime is transient flow between laminar and turbulence when Reynolds numbers is about 100 according to Figure 2.6. The R_e is calculated as 90 in the experiment shown in Figure 3.8. The water flow is at high Reynolds number laminar flow. As a result, eddies may occur; that is, aggravated waves would build-up at the water oil interface.

3.4.2.4 Sustained Transverse Mixing of Blobs

Scattered blobs have been observed after perturbation. Some red water blobs never went back to water stream and remained in oil layer (in Figure 3.9). Since the measurable driving force is only in horizontal pressure difference, the other forces resulting in the sustained blobs may be the combination of surficial tension and gravity.

Table 3.7 Comparison of surficial tension and gravity for water blobs

Blob radius	r=	1	inch
Gap	b=	0.011	inch
Interfacial tension	s=	30	dynes/cm
Interfacial force	p_c=	214.75	$10^{-3}N/m^2$
Interfacial area	A=	0.446	cm^2
Interfacial force	F_C=	9.6E-06	N
Gravity of blob	F_G=	5.5E-06	N

The capillary force holding the blob is larger than the gravity of the blob in Table 3.7. Using parametric analysis on the size of blobs, the results show that the bigger blobs have more possibility (F_G>F_C) to fall back to water bulk flow.

3.4.2.5 Comparison of Analytical and Experimental Results - Water Cut

Watercut is an important response indicating the effects of transverse mixing at the two phases' interface (in porous media, watercut is a function of the mobility ratio in the segregated flow by Darcy's Law). Water and oil rates were computed from the observed pressure difference and liquid thickness in Table 3.8 and 3.9 (static water oil contact was observed). Watercut can be computed for Eq. 3.15.

Table 3.8 Calculated water rate based on the observed pressure difference

Geometry of experiment			Q	Δp/Δl	A	μ	v	Time	Volume	N_{Re}	Pressure
length(ft)	height(ft)	width(ft)	(GPM)	(psi/ft)	(ft^2)	(cP)	(ft/s)	min	Gallon		psi
2.875	0.336	0.0009	0.0885	1.31	0.00031	1	0.64	30	**2.7**	58.8	**3.8**
2.875	0.336	0.0009	0.11336	1.68	0.00031	1	0.82	30	**3.4**	75.4	**4.8**
2.875	0.336	0.0009	0.1968	2.92	0.00031	1	1.42	30	**5.9**	130.8	**8.4**

Table 3.9 Calculated oil rate based on the calculated pressure difference (Table 3.8)

Geometry of experiment			Q	Δp/Δl	A	μ	v	Time	Volume	N_{Re}	Pressure
length(ft)	height(ft)	width(ft)	(GPM)	(psi/ft)	(ft^2)	(cP)	(ft/s)	min	Gallon		psi
2.875	0.560	0.0009	0.00864	1.31	0.00051	17	0.04	30	**0.3**	0.2	**3.8**
2.875	0.560	0.0009	0.01105	1.67	0.00051	17	0.05	30	**0.3**	0.3	**4.8**
2.875	0.560	0.0009	0.01928	2.92	0.00051	17	0.08	30	**0.6**	0.5	**8.4**

With the flow rate for each layer, and using the following simple formula,

$$WCT = \frac{Q_w}{Q_w + Q_o} \quad \text{.....(3.15)}$$

The calculated water cut for all the tests in Table 3.8 and 3.9 are equal to 91.1%. The calculated water cut may not change since both streams rates follow Darcy's Law.

Three experimental results in Table 3.10 show higher watercut the outlets. The watercut does not remain constant as flow rates change: the higher the pressure drop, the higher the water cut (See Figure 3.10). The reason may be that the intensity of shearing effect increases the amplitude of dispersed water waves. In other words, more water invading oil layer causes larger transverse mixing, in turn, bigger water cut.

Table 3.10 Observed watercut calculated from the experiments

	P_{Inlet}	P_{Outlet}	Q_{total}	Q_{water}	Q_{Oil}	WCT	ΔP	v_w
	psi	psi	ml/min	ml/min	ml/min	fraction	psi	ft/s
Run_#1	3.8	0	162	150	12	0.926	3.8	0.21
Run_#2	5	0.2	235	218	17	0.928	4.8	0.31
Run_#3	9.25	0.9	881	820	61	0.931	8.4	0.90

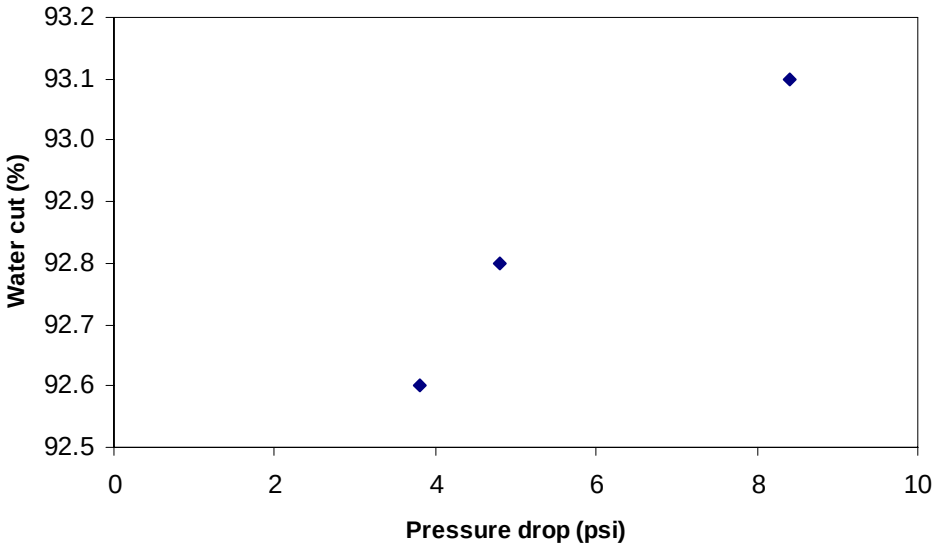

Figure 3.10 Increase of water cut with enlarged pressure difference

3.5 Discussion

In the Hele-Shaw cell, the interface is laterally constrained but vertically free. Transverse mixing at this interface is caused by the shear rate. In the experiments, the water globules were

cast into the oil stream, as the vertical force balance was lost, while the horizontal pressure distribution remained unchanged. The "transition zone" is formed comprising water waves. This transition zone smoothes out the velocity difference between water and oil layers.

Locations of the dispersed water globules above the interface were measured. The results are shown in Table 3.11 and plotted in Figure 3.11. In the plot, the horizontal arrows represent the stable flow section that becomes shorter with increasing velocity. The section's length depends on the velocity contrast and interfacial tension. At the end of the section, transverse mixing begins. The mixing zone is built of waves with varying amplitudes. When shear force is larger than interfacial tension, individual water globules are broken off the water waves, and enter the oil phase. Hence, the mixing zone comprises scattered water globules and water waves.

Table 3.11 Location of water blobs

v_o=0.015 v_w=0.12 ft/s		v_o=0.013 v_w=0.2 ft/s		v_o=0.05 v_w=0.9 ft/s	
x	z	x	z	x	z
in.	in.	in.	in.	in.	in.
5	1.1	1.2	2	3	2.4
7	0.8	4.8	1.2	7.5	1.5
10.1	0.5	9.6	0.8	15	0.7
15.5	0.2	14.5	0.5	20	0.4
19	0	19.5	0.05	23	0.1

*x= distance from the outlet
z= height of mixing zone

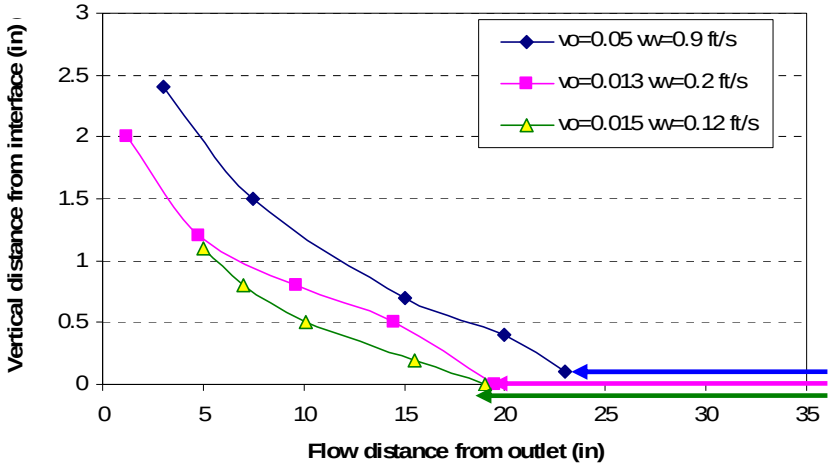

Figure 3.11 Onset and pattern of water dispersion

Meignin et al. (2000) reported on the effect of the gap size on the interface instability of Hele-Shaw cells. For viscous fluid and air, he defined the instability threshold as a critical velocity at the onset of instability. He also defined the critical wavelength corresponding to the most unstable frequency which is a function of velocity. His results showed that the instability threshold and the wavelength increased with the enlargement of gap size of the Hele-Shaw cell (Figure 3.12). As wavelength correlating with amplitude (wave height), size (thickness) of the mixing zone would reduce for smaller gap size. For gap sizes of the order of pore sizes in porous rocks, mixing zone may be negligible small – even in H-S flow cell – with sharp static interface.

In actual rocks, static interface is not sharp, and its size is controlled by capillary pressure. In fact, the lower the rock's permeability is, the greater the capillary pressure, and capillary transition zone. Thus, reducing shearing rate (shear force) must occur at the fluid interface. Theoretical permeability of 0.28 mm gap is 6500 Darcy, evaluated according to Smith and Greenkorn (1969) equation,

$$k = \frac{d_g^{\,2}}{12} \qquad \text{.....(3.16)}$$

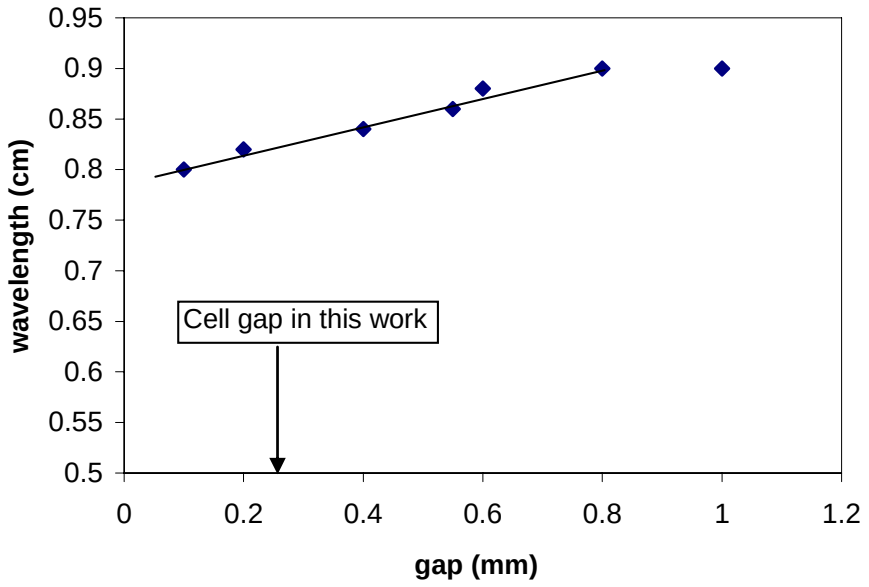

Figure 3.12 Wavelength decreases as plate gap reduces (Meignin et al., 2000)

Capillary pressure and shear force between the plates are shown in Table 3.6-2. Based on the calculations, for less permeable rocks the difference between capillary and shear force would dramatically increase. For example, for one Darcy permeability, the capillary pressure can be more than 30 times higher than the Hele-Shaw's permeability resulting in much smaller shear. Therefore, even in H-S cells, the instability of interface due to shear force may be negligibly small for gap sizes within the range of rock pore sizes.

3.6 Summary

1. In a complementary attempt to study oil/water interface instability and transverse mixing in porous media, a vertically segregated two fluid Hele-Shaw model is used. The model features sharp oil/water interface thus emphasizing shearing effect while disregarding tortuosity collision, and momentum transfer effect.
2. The unstable interface becomes a mixing zone built of water fingering and scattered water blobs in the form of waves. It appears that this mechanism is similar to the linear Kelvin-Helmholtz instability.
3. Experimental results show that the velocity difference (shearing rate) between water and oil is the key parameter to the onset of transverse mixing. Also length of unperturbed interface reduces with increasing velocity difference.
4. Shear force between the fluids due to the velocity difference must overcome viscous forces between fluids and solid walls, gravity and interfacial tension to generate any perturbation (i.e., waves).
5. Due to the much larger vertical dimension of the Hele-Shaw cell as compared to the gap, the instability observed in these experiments may not be directly applicable to any real porous media.

6. In most formation rocks, capillary force is larger than shear force, and the instability due to these shear forces may not be the dominant mechanism. However, in a fractured formation, such instability may exist.

CHAPTER 4

TRANSVERSE MIXING DUE TO PORE-SCALE MOMENTUM TRANSFER

In this chapter, momentum transfer has been studied by considering unbalanced forces and momentums between fluids at grains. With collisions, higher-momentum fluid may flow across their interface, and transition zone forms. Ratio of pore and throat size, determined by internal structure of porous media, is critical for extended mixing zone. The effects involve impingements between fluid/fluid and fluid/rock.

Using dimensionless groups, inertial, capillary, and gravity forces are compared using Weber and Richardson numbers. Critical conditions of transverse mixing are examined.

To illustrate the mixing mechanism caused by momentum transfer across an immiscible interface, a simplified pore-scale flow scenario of two segregated flow streams impinging on a rock grain has been modeled analytically in Appendix C. Computation show that for a given structure of the pore-grain system (homogeneous rock) fluid saturation change due to collision at grains and between fluids can be computed. However, the computations in Appendix C merely demonstrate the phenomenon by considering only one structure and segregated flow pattern. Other pore-grain structures and the patterns (heterogeneous rock) of segregated flow may strongly affect the fluid saturation change. Therefore, only complete network modeling of two-phase flow in porous media could effectively simulate the entire grain-by-grain process of momentum transfer resulting in growth of transition zone.

4.1 Criteria for Transverse Mixing

Flow instability in porous media, which leads to transverse mixing, is evaluated using the force potential theory (Bentsen, 1985). By assuming that true interstitial velocity can be calculated

from the flow rate, we may determine how transverse mixing could occur when the flow is diverted at grains.

On a microscopic scale, linear flow is diverted when the driving forces are unbalanced. Four major forces in porous media have been identified by Lake (1996): gravity, viscous force, capillary, and inertia. A comparison of these forces is critical to find whether a flow system is in stable condition. Gravity, capillary and inertial forces perpendicular to the flow direction are the major factors for stabilization in the transverse direction.

In a segregated flow of two fluids in an ideal porous medium, transverse mixing occurs when inertial forces due to flow diversion overcome gravity forces or/and capillary. Since relative values indicate which force is dominant, the ratios of transverse water inertial force, capillary force, and gravity force provide criteria for transverse mixing. Therefore, the inertia-capillary ratio is expressed as

$$N_{CV}' = \frac{F_T}{F_c} = \frac{\rho v_T^{\,2} A}{p_c^{\,*} A} = \frac{\rho v_T^{\,2}}{p_c^{\,*}} \quad \text{.....(4.1)}$$

Where, the dispersed water velocity v_T is the interstitial velocity.

Zhou *et al.* (1997) used the empirical expression (Eq. 4.2) to find capillary pressure,

$$p_c^{\,*} = 4\sigma_o \cos\theta \left(\frac{c\phi}{k}\right)^{\frac{1}{2}} \quad \text{.....(4.2)}$$

Where, k is permeability from core's measurements. c is a constant depending on the medium, c = 0.02 for glass bead-packs.

The common method for assessing capillary pressure is to use capillary tube when the radius (r) of average pore throat is known. e.g., for the glass beads or uniform grains

$$p_c^{\,*} = \frac{2\sigma_o}{r} \cos\theta \quad \text{.....(4.3)}$$

In segregated flow, the gravity prohibits fluid upward flow. For instance, from the Hele-Shaw experiments, the collapse of waves in the model indicates that gravity eventually stops the transverse flow process (Duan and Wojtanowicz, 2007). The inertia-gravity ratio may be expressed as

$$N_{GV}' = \frac{F_T}{F_G} = \frac{\rho v_T^{\,2}}{\Delta\rho g d_p^{\,*}} \quad \text{.....(4.4)}$$

The grain diameter in Eq. (4.5) can be evaluated from the Carmen-Kozeny theory (Al-Bazzaz and Al-Mehanna, 2007)

$$d_p^{\,*} = \sqrt{\frac{k*(1-\phi)^2}{3.631*10^9*\phi^3}} \quad \text{.....(4.5)}$$

Where, d_p^* is the diameter of a uniform grain, inch.

When both dimensionless numbers (N_{CV}' and N_{GV}') are larger than 1, crossflow of water into oil phase may occur and lead to transverse mixing. These two numbers also provide that the maximum inertia force that can cause transverse mixing regardless of tortuosity and eddy (Zhou *et al*., 1997). To make these numbers commonly acceptable, in the following criteria, Weber number and Richardson number are introduced to substitute N_{CV}' and N_{GV}', respectively.

Basically, the Richardson number describe the ratio of gravity and inertia forces, while the Weber number measure the ratio of inertia and capillary force (Israselachvili, 1995 and Rowlinson and Widom, 1982).

$$R_i = \frac{gh}{v^2} \quad \text{.....(4.6)}$$

$$W_e = \frac{\rho v^2 h_c}{\sigma} \quad \text{.....(4.7)}$$

Where, h_c represents the hydrostatic height due to capillary force

It should be mentioned that Weber number (Eq. 4.7) is used for evaluation of non-wetting phase transverse mixing, e.g., oil invades water layer in glass bead pack model. In this study Sand and glass bead-packs are both water wet, so Eq. (4.7) will not be used for the following analysis of transverse mixing.

Therefore, the inertial force of water from its body velocity and path change is the major source causing unbalanced force in water transverse mixing in water-wet porous media.

4.1.1 Inertial Force from Flow Path

Noman and Archer (1987) opined that, during flow through a straight pipeline at low rate, i.e., at low Reynolds number, the viscous forces are dominant and so the inertia term is usually ignored in momentum balance equation. For flow through a porous medium, the presence of a solid matrix ensures that fluid streamlines are never straight. The slightest degree of curvature in the path-line introduces acceleration of the fluid particles. Hence, inertia forces can become significant in flow through porous media even at fairly low rates. Experimental measurements have shown that in unconsolidated media the Darcy equation begins to fail at a Reynolds number of about 1.

Dullien (1979) demonstrated their laboratory work and showed that for low flow rate, Darcy's law could predict the pressure drop adequately and the quadratic term could be ignored. For higher rates of flow, the Forchheimer relation represented all their experimental data accurately. It was also found that the inertial term rapidly increased with an increase of ratio of pore diameter (d_{pore}) and throat diameter (d_{throat}). The excess viscous dissipation was, however, found to be related very weakly to the length of pores and throats.

$$\Delta p \sim v^2\left(\left(\frac{d_{pore}}{d_{throat}}\right)^2 - 1\right) \quad \text{.....(4.8)}$$

4.1.2 Criterion Based on Force Balance

Richardson number in Eq. (4.6) is a general expression. In a segregated flow, Kundu (1990) noted that, oil and water have different density – one fluid density is ρ_1, another fluid density is ρ_2. The effective gravity in a two-layer situation is the "buoyancy" force $(\rho_2-\rho_1)g$. In the case, we may define a Richardson number as

$$R_i = \frac{g' d_p^*}{v^2} \quad \text{.....(4.9)}$$

Where, $g'=(\rho_2-\rho_1)g$ called "reduced gravity". $[L]/[T]^2$

d_p^* = diameter of grains, [L]

For a two-phase flow in porous media, a modified Richardson number should be applied with a correlation related to d_{pore}/d_{throat}. Therefore, substitute the correlation (4.8) to (4.9), it gives a modified Richardson number

$$R_i' = \frac{g' d_p^*}{v^2\left(\left(\frac{d_{pore}}{d_{throat}}\right)^2 - 1\right)} \quad \text{.....(4.10)}$$

From K-H instability, R_i should be less than 0.25 to cause unstable interface where a stratified two-phase flow occurs (Kundu, 1990). Hence, a criterion for transverse mixing may be that the modified Richardson number (Eq. 4.10) should be less than 0.25.

4.1.3 Relationship between d_{pore}/d_{throat} and Non-Darcy Flow Coefficient β

At macroscopic scale, a quadratic term with an inertial flow coefficient (β) should be considered at high velocity flow, as a Forchheimer's term shown in Eq. 4.11 (Geertsma, 1974). The equation indicates that the inertial force would significantly increase pressure gradient when velocity and β are large.

$$-\frac{dp}{dr} = \frac{\mu v}{k} + \beta \rho v^2 \quad \text{.....(4.11)}$$

Eq. (4.11) is fit for single-phase flow in unconsolidated and consolidated porous media. There are many factors related to Non-Darcy factor β such as tortuosity (τ), for example. Li and Engler (2001) stated that pressure gradient in the flow parallel to the dominant driving force's direction; the non-Darcy β factor is not related to tortuosity as

$$\beta = \frac{c_1 c_4}{k^{1+c_2} \phi^{c_2-1}} \quad \text{.....(4.12)}$$

For pressure gradient in the flow direction perpendicular to the dominant driving force's direction, the β factor relates to tortuosity as

$$\beta = \frac{c_1 \tau}{k^{c_2} \phi^{c_3}} \quad \text{.....(4.13)}$$

In the above two formulas,

c_1 = constant in β correlation

c_2 = permeability exponent

c_3 = porosity exponent

c_4 = constant in k-τ correlation

The different sizes of pore and throat may significantly increase the tortuosity of flow path (Noman and Archer, 1987). Tortuosity increases with increasing pore-to-throat size ratio, so β value is also increased.

The relationship between F_o vs. Reynolds number in Figure 4.1, published by Ma and Ruth (1997) also demonstrates the effect of pore-to-throat size on β. In the semi-log plot, F_o is the ratio of inertial force and viscous force at different flow velocities, as

$$F_0 = \frac{\beta k \rho v}{\mu} \quad \text{.....(4.14)}$$

The plot shows that for $R_e>1$, $F_0>0$, e.g. the inertial component, $\beta g v^2$, in Forchheimer formula (4.11) becomes increasingly significant.

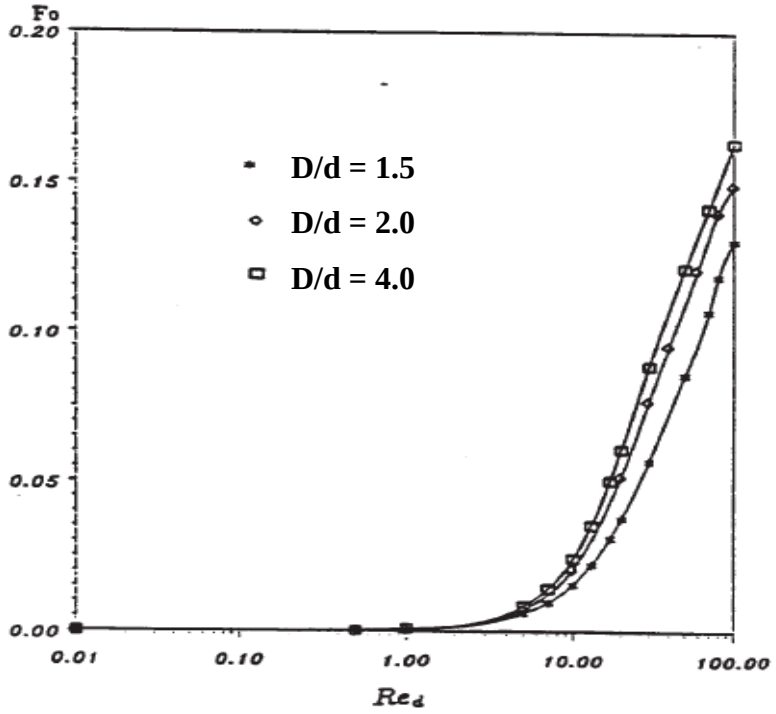

Figure 4.1 Variation of Forchheimer number (F_o^*) with Reynolds number in a VA model (from Ma and Ruth, 1997)

4.2 Mechanistic Analysis of Mixing Mechanism in Pore-Scale

In order to describe the complex fluid/fluid and fluid/rock interactions at high velocity, a simplified porous media model is necessary. Bear (1969) stated that cubic packing with 47% porosity is uncommon in actual porous media. Rhombohedral packing of uniform particles (Figure 4.3-a) is more representative of any actual porous media since the grains tend to be consolidated as in the actual rock. This type of packing has 26% porosity (Figure 4.2-b). A simple network structure composed of the pores and throats is shown as Figure 4.2-c.

For a given porosity and grain packing pattern, the size of pores, throats, and grains can be estimated from published formulas. One of the formulas (Amyx *et al.*, 1960) employs the Poiseuille equation for flow in the throats of porous media, and computes permeability of

bundled tubes with radius r as,

$$k = \frac{\phi r^2}{8\tau} \quad \text{.....(4.15)}$$

Solving (4.15), for r gives

$$r = \sqrt{\frac{8\tau k}{\phi}} \quad \text{.....(4.16)}$$

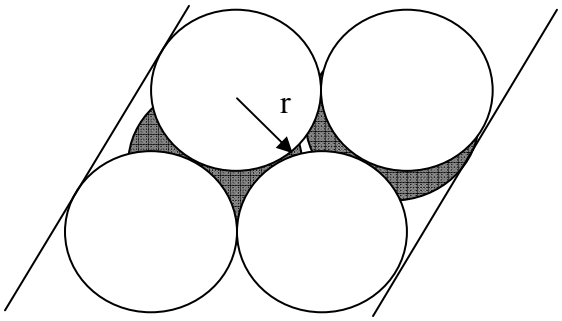

4.2-a Rhombohedral packing

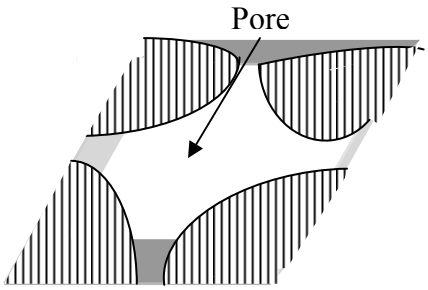

4.2-b Pore and throats in cross-section of a rhombohedral packing

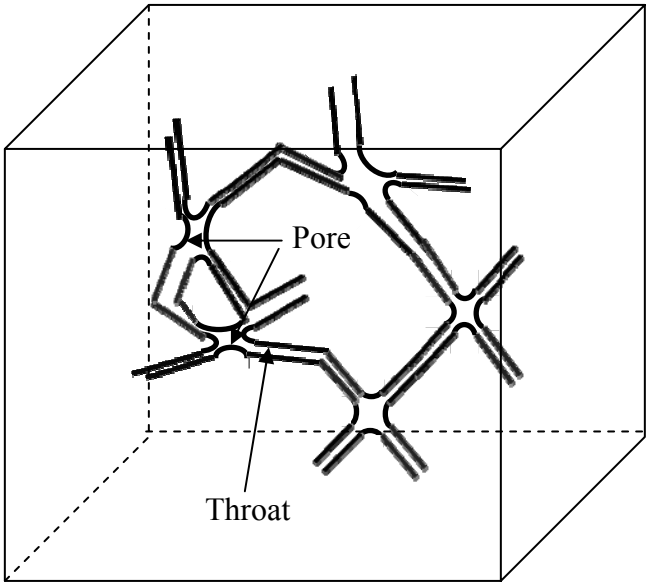

4.2-c Groups of simplified pores and throats

Panda and Lake (1994) derived another model for a single-phase flow using Carman-Kozeny estimate of permeability as

$$k = \frac{d_p^{*2}\phi^3}{72\tau(1-\phi)^2} \quad \text{.....(4.17)}$$

Solving (4.17), for d_p^* gives

$$d_p^* = \sqrt{\frac{72\tau(1-\phi)^2 k}{\phi^3}} \quad \text{.....(4.18)}$$

Substitute Eq. (4.15) to (4.18), the relation between d_p^* and r can be expressed as:

$$d_p* = \frac{3(1-\phi)}{\phi} r \quad \text{.....(4.19)}$$

In the formation rock, the fluid flow path is continually split. If two fluids are flowing, their flow path diversions result from collisions between fluid and rock grains and fluid and fluid, which may cause transverse mixing. When one fluid's momentum is greater than that of the other fluid, the fluid with larger momentum will displace the other in a piston or partial displacement pattern (see Figure 4.3). For piston-like displacement, there will be a single phase flow in the displaced throat. For example in Figure 4.4-a and 4.4-b, two fluids from two different throats converge in a simple throat. In one case (4.4-a) the fluids will continue to flow together, while in another case (4.4-b) fluid with higher momentum will block another fluid with smaller momentum. Figure 4.4-c demonstrates uneven distribution of the two fluids flowing and colliding together at a rock grain. This case is further analyzed mathematically in Appendix C.

For partial displacement, there will be a snap-off displacement in the displaced throat. Since the phase's velocity after collision can be possibly evaluated, a demonstration of saturation distribution during partial displacement is analyzed in Appendix C.

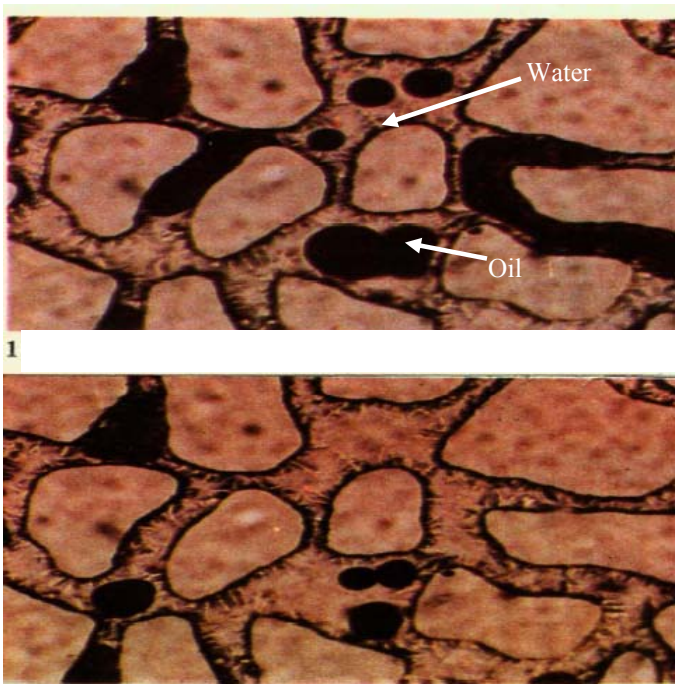

Figure 4.3 Water displacing oil patterns (Guo and Chen, 2007)

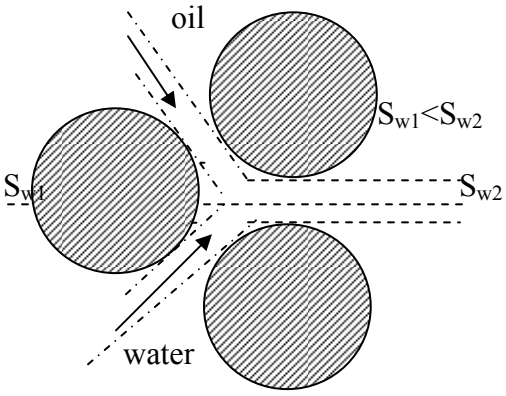

4.4-a Segregated flow collision

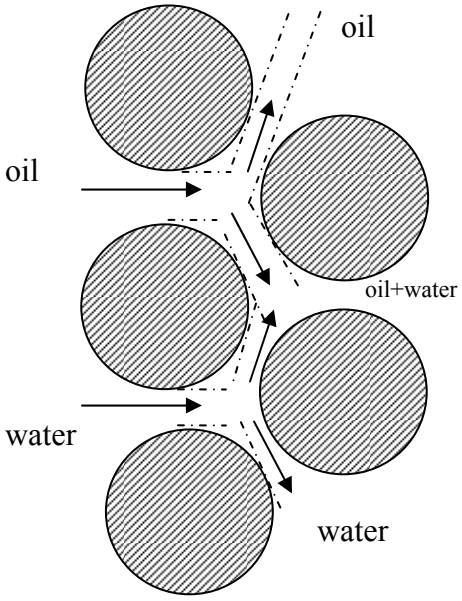

4.4-b Two bifurcated flow convergence and collision

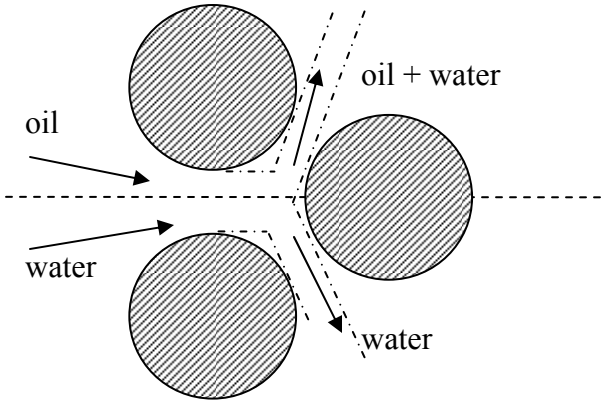

4.4-c Flow diverges unevenly after collision

4.3 Transverse Mixing at Grains due to Collision – Piston-Like Displacement

Laws of momentum and energy are applied in analyzing transverse mixing in pore scale. 4.4-b has been used as a primary model for analyzing saturation change in piston-like displacement in Appendix C. Meanwhile, water and oil flow segregately in separated pore throats before their collisions with grains. The following assumptions are used for establishing a simplified model:

1. Prior to the collision, water and oil flow together in separated throats;
2. All grains have the same size, "d_p";
3. Capillary effect is much smaller compared with inertial force and can be ignored;
4. During collisions between two fluids, momentum is conserved without vortex effect;
5. No grains migration occurs.

Boundary conditions and related flow parameters in Figure C-3 are introduced. In momentum and force change the mechanism of transverse mixing caused by the divergence of flow at grains, depicted in Figure 4.4-b and Figure C-3, has been modeled mechanistically. Mathematical analysis of the process is presented in Appendix C. The summary of the analysis is followed after fluid collision with grains:

1. When the oil stream may have larger momentum than water stream in pore throats, water transverse mixing may be prohibited. Then oil may invade into the water phase after

collision, and the same volume of water could be displaced, the amount of oil mixing with water can be evaluated using Eq. (C.28).

2. When the water's momentum is larger than the oil's momentum, the water enters oil layer, and water transverse mixing occurs. The increased water saturation after the collision in oil layer can be evaluated using Eq. (C.29) in case of piston-like displacement.

3. When the water possibly has the same momentum as the oil, there is no momentum transfer after collision. In other words, the condition is stable that there is no water or oil saturation change after collision.

4.4 Transverse Mixing at Grains due to Collision – Snap-Off Displacement

Another model for snap-off displacement is considered in Appendix C as well. For example, if the shapes of pore throats are not round in Figure C-1, movable water may exist in the space of oil blobs and solid wall. In Appendix C water is assumed to be a wetting phase, and described as a continuous stream making oil stream become individual blobs after collision (Figure C-4). The results of saturation change are shown in C.36.

Based on the theory of energy conservation, Froude number may be applicable for mixing stabilization evaluation from kinetic energy to potential energy. From this view, the transverse mixing fluid may be stabilized at certain higher position as its velocity reduces after collisions. The potential height after collision is shown in Eq. (C.40) in Appendix C.

4.5 Summary

1. Transverse mixing criteria for segregated flow in porous media are developed using a modified dimensionless group (Richardson number). The ratio of diameters of pore and throat are considered for inertial force computation.

2. That R_i is less than 0.25 for Kelvin-Helmholtz instability could be used for evaluation of onset of transverse mixing in porous media. Further evidence is needed to confirm its feasibility.
3. Experimentally and theoretically, larger the ratio of size of pore and throat may result in increase of non-Darcy coefficient β. But on the other hand, there lacks evidence that β has direct relationship with the ratio.
4. An analytical demonstration of pore-scale fluid/grain and fluid/fluid collision is presented in Appendix C to explain the mechanism of water transverse mixing in the oil. The computations show that water saturation distribution after a collision is a function of water saturation prior to the collision.
5. The computations of mixing effect at a single grain merely demonstrate the phenomenon by considering one idealized pore-grain structure and a segregated flow of oil and water pattern. Other pore-grain structures and two-phase flow patterns may strongly affect the change of fluid saturation distribution.

CHAPTER 5

EARLY TRANSVERSE MIXING IN LINEAR GRANULAR FLOW CELL EXPERIMENTS

The objective of this chapter is to verify and analyze transverse mixing in porous media by a series of granular-pack flow experiments. A linear flow cell having 15-inch in length, 6-inch in height, and a 0.25-inch gap was packed with different sizes of glass beads (0.5 mm and 1.0 mm) and sand (average 0.6 mm) and flown through by segregated streams of oil and water at pressure gradients up to 22.4 psi/ft. Only early-time transverse mixing has been observed in the upstream section of the cell as dimensional and end effects distorted the flow in the downstream cell section.

The chapter gives an overview of experimental procedure describing the cell packing protocol, flow test design, measurements and monitoring routines. Each flow test was video-taped and photographed so that fluid saturation could be measured and analyzed with a color-sensing software. Also analyzed are interactions between pressure, velocity, water saturation, and size of transverse mixing zone.

The results show no oil invasion into the water layer – only water invading oil layer with water saturation at the initial W/O interface remaining constant. Transverse mixing increased for higher flow velocity (pressure gradients) and larger grain sizes. However, a high-viscosity oil reduced mixing effect. Also, the results show that the size of mixing zone was proportional to square root of time, thus following the dispersion principle.

5.1 Properties of Fluids and Granular Media

Four different packing materials (two sizes of glass beads and two types of sand) and three different viscous oils were used in the flow experiments.

5.1.1 Porous Media in the Experiments

Two types of sand were selected - Columbia #16 and #2 Q-ROK. The sand size distributions are shown in Tables 5.1 and 5.2. Also, porosity and permeability measurements of the packed sands are listed in Table 5.3. The log-log plot in Figure 5.1 is a linear correlation of measured permeability and average value of the grain diameters.

Table 5.1 Distribution of particles of #2 Q-ROK sand (the diameter's mean=0.6 mm)

Mesh	Diameter (mm)	Distribution (Fraction)	Cum. Distribution (Fraction)
16 M	1.18	0	0
18 M	1	0.03	0.03
20 M	0.85	0.03	0.06
25 M	0.71	0.36	0.42
30 M	0.6	0.26	0.68
35 M	0.5	0.15	0.83
40 M	0.425	0.09	0.92
50 M	0.3	0.07	0.99

Table 5.2 Distribution of particles of Columbia #16 sand ($\overline{d_p}$=1.3 mm)

Mesh	Diameter (mm)	Percentage
12 M	1.68	0.237
16 M	1.19	0.756

Table 5.3 Properties of porous media

Particle Name	Permeability (Darcy)	Porosity (fraction)
Columbia #16 sand	900	0.39
1.0 mm glass beads	414	0.43
0.5 mm glass beads	333	0.43
#2 Q-ROK sand	294	0.39

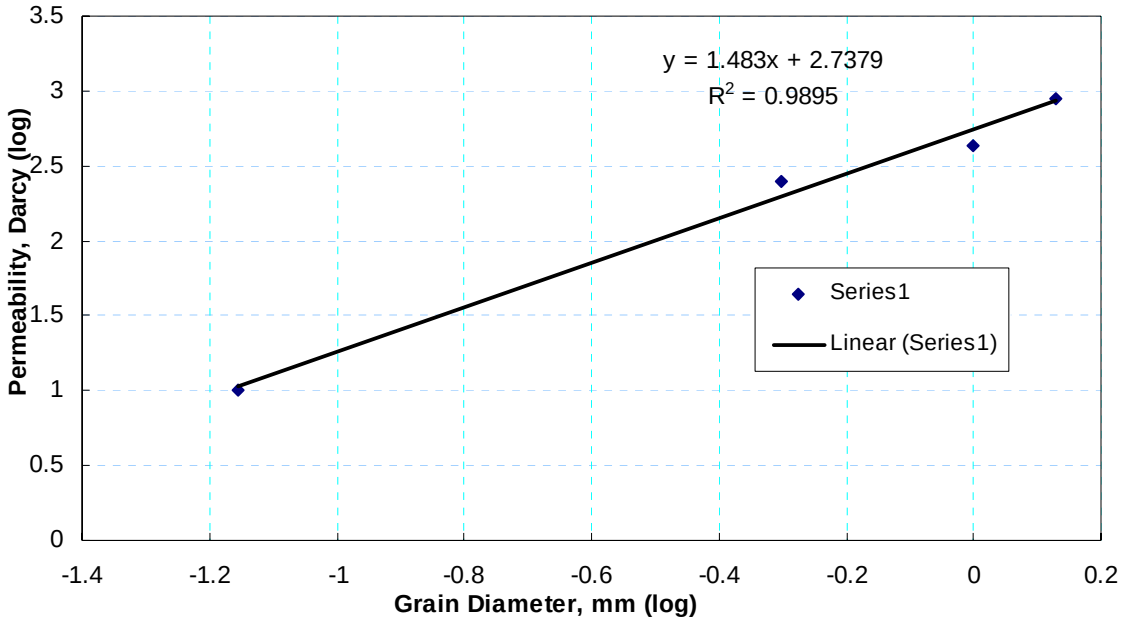

Figure 5.1 Linear log-log correlation of permeability vs. grain size

Two permeability meters (Figures 5.2 and 5.3) were employed for measuring the packed porous media permeability. In the permeameters, two pressure gauges are mounted at the ends of a steel pipe. A filter is placed at the exit end to prevent particles from flowing out. A water hose is connected to the entry end to supply fluid. Hydraulic pressure provides packing mechanism. The packing was conducted in step-wise fashion until the pipe was completely filled out with sand.

Figure 5.2 Permeability meter (1)

Figure 5.3 Permeability meter (2)

5.1.2 Fluid's Viscosity

Fluid viscosity was measured by a Cannon-Fenske meter. To obtain different viscosities, shown in Table 5.4, different mixtures of Soltrol and mineral oil were made. Viscosity was measured in triplicates, and the average value recorded.

Table 5.4 Viscosity of the test fluids

	Viscosity meter factor (cst/s)	Density (g/cc)	Measured flow time (seconds)	Calculated viscosity (cp)
Dyed water	0.03558	1	31	1.1
Soltrol	0.09266	0.762	35	2.5
Heavy Mineral Oil / Soltrol (1:1.5)	0.50155	0.708	19	6.7
Heavy Mineral Oil / Soltrol (1:1)	0.1073	0.72	160	12.5

5.2 Design of Flow System

The flow system is shown in Figure 5.4. The system consists of two major parts, the fluid's recycling system and the flow cell.

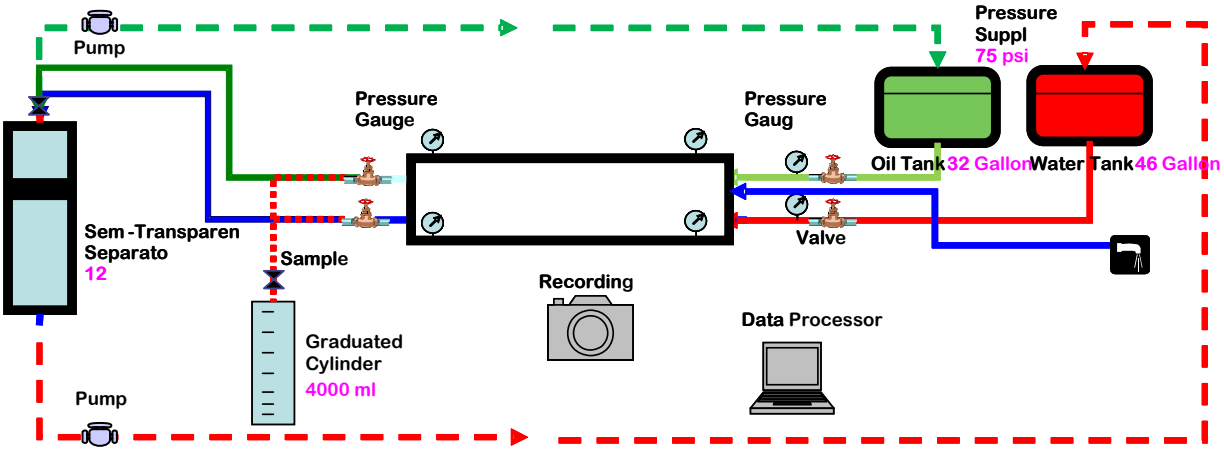

Figure 5.4 Schematics of flow system

5.2.1 Fluid-Recycling System

The system includes installations for oil and water storage, pumping, collection, separation and measurement. It consists of two liquid tanks, two utility pumps and one gas compressor. The maximum supply pressure by the compressor is of 75 psi. The pressurized liquid in each tank is released to flow through the pipelines to the flow cell's inlets. Inlet pressure gauges are used to monitor the instantaneous inlet pressure, and keep the inlet pressure values of oil and water equal. At the outlet, a big container receives the water-oil mixtures. Total flow rate is measured using graduated cylinders and single phase rate computed from fluid separation in the cylinders. The whole mixture is gravity-separated. A complete separation of water and oil takes approximately 10 minutes. After separation, the fluids are pumped back to the storage tanks using two 1/8 HP utility pumps.

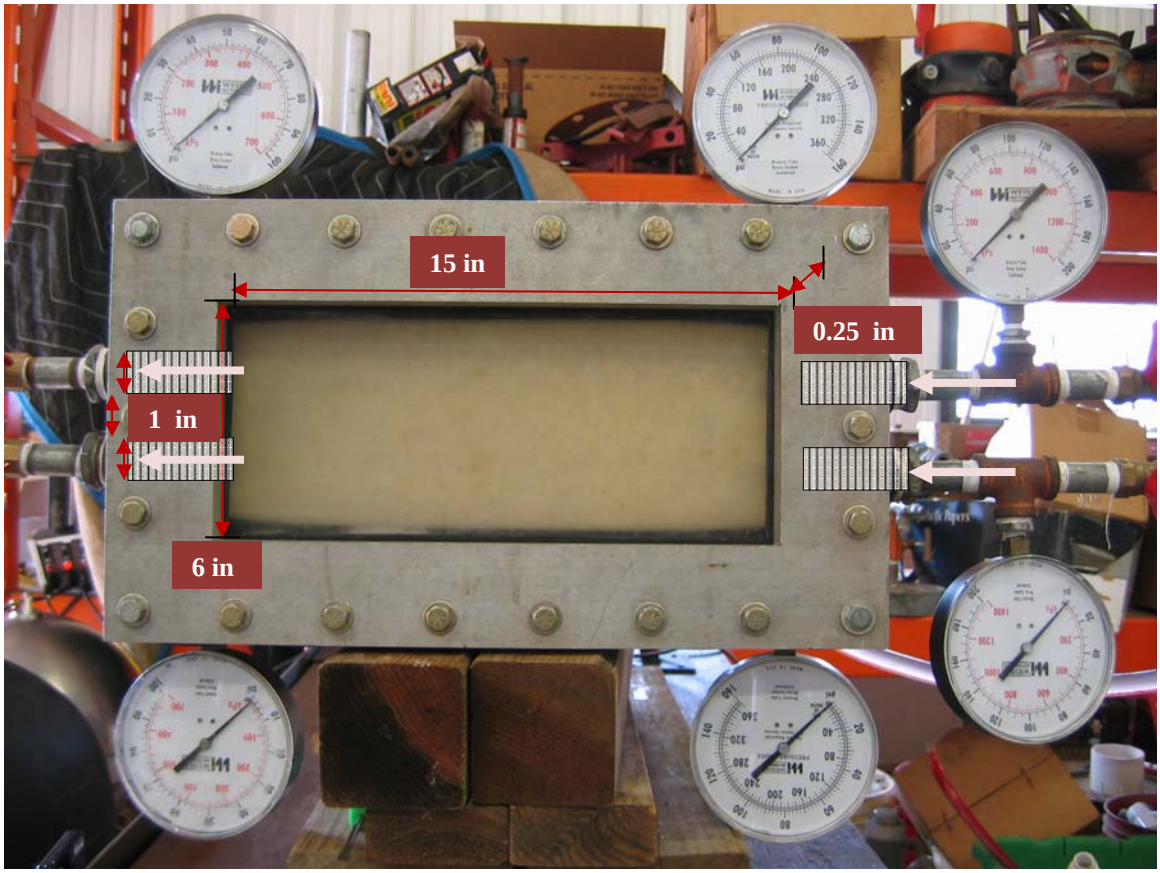

Figure 5.5 The dimension of the actual model

5.2.2 Flow Cell

Shown in Figure 5.5 are the dimensions of the flow cell comprising two parallel clear one-inch plexiglass plates with a gap. Diameters of the two inlets and the two outlets are as much as 1 inch to minimize local pressure losses at the entry and exit from the cell and maximize pressure drop across the granular pack. The flow direction is from right to left.

The cell and granular packs have been designed to obtain relatively high interstitial velocities at the maximum pressure for the cell. However, the flow tests have shown that dimensional effects constrain the dispersed flow. As shown in Figure 5.6, initially the mixing zone raises above the initial W/O interface. As the fluid approaches the outlets, the flow streams converge towards the two outlets. The mixing zone shrinks to the interface of the outlets because of the end points. The maximum height at the mixing zone may be affected by vertical size and end effect of the flow cell. Hence, these effects should be considered when studying transverse

mixing. Because of these limitations, the only mid-distance was selected to evaluate the mixing zone.

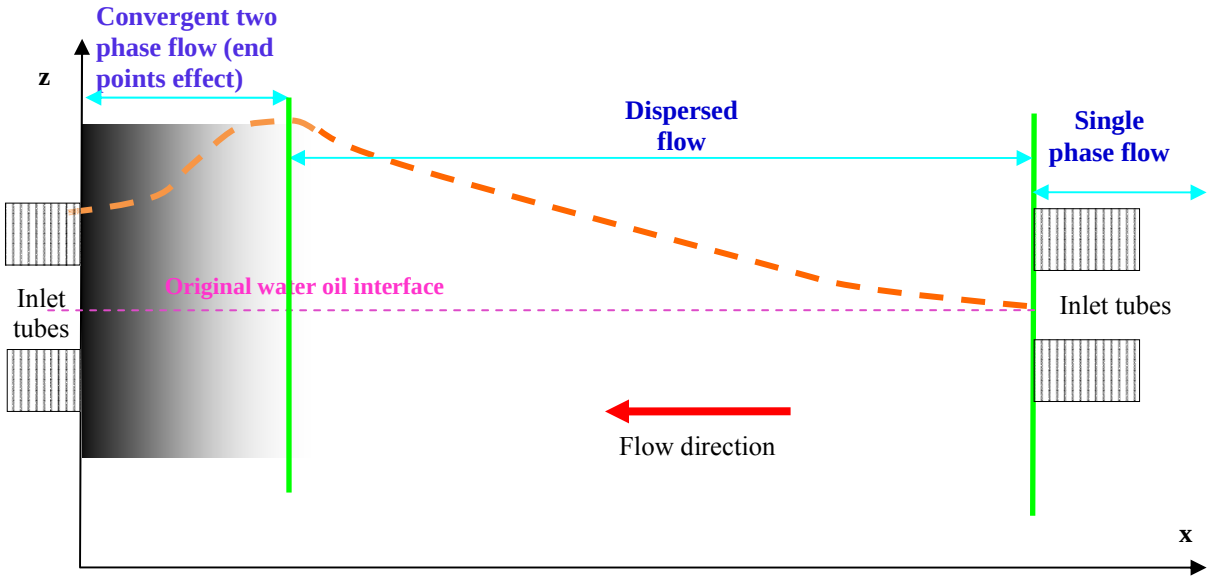

Figure 5.6 Dimensional effects in transverse mixing

5.2.3 Flow Cell Scaling Verification

Duration of flow time in the cell should be verified in order to verify if the cell dimensions are suitable for observing transverse mixing.

A scaling analysis was used by Cinar et al. (2006), Zhou et al. (1997) and Lake and Hirasaki's (1981) to identify a transverse flow in the segregated flow. In this study, their method has been used to analyze whether the flow cell could capture the transverse mixing phenomena using the transverse mixing number (N_{TM}) was a ratio of the times needed to cross the porous medium longitudinally and transversely. It has been set as 5.0 to indicate the effect of the denominator is larger than numerator (Zhou et al, 1997). In other words, if the minimum visible size of transverse mixing requires five-fold smaller time to be noticed than the flowing time through the model, transverse mixing could be observed in our cell. According to the color-sensing method, the minimum visible height (h_{mv}) for the cell is 0.2 inch. Assuming transverse flow value of 0.4 inch/second (v_w) estimated from our experiments, the transverse velocity of

water is approximately 0.2 inch/second (v_{wt}). The cell length is 15 inches. The computed time ratio is much larger than 5 (Eq. 5.1).

$$N_{VH} = \frac{Lv_{wt}}{h_{mv}v_w} > 5 \quad \text{.....(5.1)}$$

Where, v_{wt} is the transverse velocity of water, h_{mv} is the minimum visible height.

Therefore, the dimension of the cell is suitable for capturing transverse mixing.

5.2.4 Flow Test Procedure

1. Only one kind of granular media is used for hydraulic packing the cell. Initially, the cell is filled up with water and tested for a leakage. Then, it is packed by flowing through and adding granular material until no more packing is needed.
2. The tightly packed cell is connected to the flow system, comprising air compressor, fluid accumulators, and recycling tanks.
3. The cell is filled up with oil-tops down. Then red dyed water is slowly injected into the cell- bottom up.
4. A flat and stable W/O interface should be observed for every run before starting flow.
5. Applying uniform (oil and water) pressure drop across the cell generates segregated flow that would quickly stabilize. Then, the outlets pressure, the inlet pressures, and the W/O interface distortion are measured, and photographs are taken.
6. Pressure drop across the cell re-adjusted after the measurements.
7. At least three pressure drop adjustments are used for each run.
8. After removing oil and dyed water, the cell is completely flushed with tap water before the next run.

5.2.5 Mapping Water Saturation

A CMYK (Cyan, Magenta, Yellow and Key/Black) module of the Photoshop™, a color-sensing software, was used to measure X-Z distribution of water saturation. As the water was colored

red, only the M element of the module was used (Figure 5.7). To calibrate the module, several known red water concentrations of the oil/water mixture were correlated with the module reading scale from 38% (oil only) to 100% (water only). The calibration produced a linear relationship between the percentages and water saturations. The resulting straight line calibration formula was used to analyze color photographs of stabilized flow of oil and water in the cell. In order to plot iso-saturation lines, linear interpolation was used to find point (X, Z) having the same water saturation.

Figure 5.7 Color code options in CMYK module of Photoshop™

5.2.6 Error Analysis of Iso-Saturation Lines

(1) There is about $\pm 5\%$ error in sensing magenta intensity by the CMYK module of Photoshop™. For example, in the pure oil zone, the reading of magenta may be from 33% or 43% (38% average). In all, the water saturation error by color sensing precision is about $\pm 8\%$ (Eq. 5.2).

$$\text{error} = \frac{100}{100-38} \times (\pm 5) \quad \text{.....(5.2)}$$

(2) Also, the size of grids used for color sensing may introduce error to the position of the iso-color line. Each reading of color represented a 1.67 in×0.21 in (length×height) grid. Therefore, error in vertical direction is $\Delta z = \pm 0.017 \text{in}$ and the longitudinal error is $\Delta x = \pm 0.13 \text{in}$.

The type of granular media also affects accuracy of color intensity sensing. Particles used in the experiments were glass beads, and sand. As glass beads are transparent, color-sensing was more precise than that with the sand pack.

5.3 Experimental Results and Analysis

For the same granular pack, at least three test runs were conducted using different viscosity combinations. The runs are summarized in Table 5.5. Each test run was video-taped and photographed with still frame photos. The photos were, then, analyzed using the procedure, described above. To determine water distribution in the transition zones, iso-lines of water saturation, 20%, 50%, and 80% were plotted and used in the further analysis. Selected photographs with iso-saturation plots are shown in Appendix A.

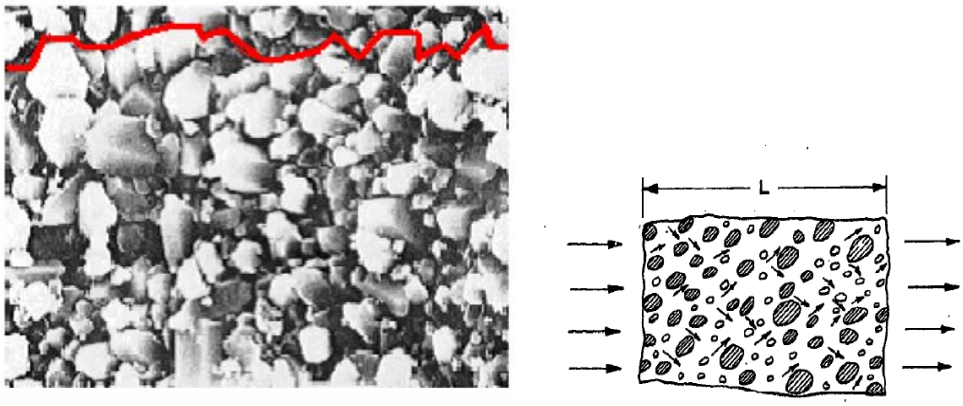

Figure 5.8 Continuous changes in flow direction (45^{o})
(Haro, 2007 and Perkins and Johnston, 1963)

A qualitative initial analysis of the results showed that a smooth, flat, water oil interface was obtained at low flow rates. By increasing pump pressure drop across the cell, the interface became unstable and a transition zone developed. In contrast to the Hele-Shaw experiments, where the fluid interface fluctuated in waves; the flow interface in porous media (Figure 5.8) steadily moves upwards. It means that the porous structure eliminates waving. But the tortuous path of the water and oil streams induces transverse mixing by mechanism other than shear effect.

Table 5.5 Summary of Experimental Results

Grain Type	Oil Viscosity	Run #	Pressure Difference (psi)	Water Velocity (ft/s)	Oil Velocity (ft/s)	Average Velocity at Interface (ft/s)	Reynolds Number (Water)	Richardson Number (Water)
0.5 mm glass beads	2.5 cp oil	sg-1-1	15	0.43	0.17	0.30	66.0	0.25
		sg-1-2	20	0.58	0.23	0.41	89.0	0.13
		sg-1-3	28	0.82	0.33	0.57	125.8	0.07
	6.7 cp oil	sg-2-1	16	0.46	0.07	0.26	70.7	0.21
		sg-2-2	21	0.60	0.09	0.35	92.8	0.12
		sg-2-3	24	0.69	0.10	0.40	106.1	0.09
	12.5 cp oil	sg-3-1	7	0.20	0.02	0.11	30.9	1.12
		sg-3-2	11	0.32	0.03	0.17	48.6	0.45
		sg-3-3	28	0.81	0.06	0.44	123.7	0.07
#2 Q ROK sand	2.5 cp oil	s-1-1	1.5	0.08	0.03	0.06	12.2	0.71
		s-1-2	3	0.13	0.05	0.09	20.4	0.26
		s-1-3	4	0.21	0.08	0.15	32.6	0.10
	6.7 cp oil	s-2-1	2	0.11	0.02	0.06	16.3	0.40
		s-2-2	3	0.16	0.02	0.09	24.4	0.18
		s-2-3	4	0.21	0.03	0.12	32.6	0.10
	12.5 cp oil	s-3-1	2	0.11	0.01	0.06	16.3	0.40
		s-3-2	4	0.21	0.02	0.11	32.6	0.10
		s-3-3	5	0.24	0.02	0.13	36.6	0.08
		s-3-4	5	0.27	0.02	0.14	40.7	0.06
1.0 mm glass beads	2.5 cp oil	lg-1-1	3	0.2	0.08	0.14	30.7	2.64
		lg-1-2	4	0.27	0.11	0.19	41.4	1.45
		lg-1-3	7	0.47	0.19	0.33	72.1	0.48
		lg-1-4	11	0.73	0.29	0.51	112.0	0.20
		lg-1-5	15	0.93	0.37	0.65	142.7	0.12
	6.7 cp oil	lg-2-1	1	0.07	0.01	0.04	10.2	23.72
		lg-2-2	4	0.27	0.04	0.15	40.9	1.48
		lg-2-3	7	0.47	0.07	0.27	71.6	0.48
	12.5 cp oil	lg-3-1	2.5	0.17	0.01	0.09	25.6	3.79
		lg-3-2	5	0.33	0.03	0.18	51.2	0.95
		lg-3-3	7	0.47	0.04	0.25	71.6	0.48

Note: sg- small glass beads, s- sand, lg- large glass beads

The results were also analyzed quantitatively for their conformance with the dispersion principles. The linear relationship between transverse distance of water saturation and square

root of horizontal flowing distance shown in Figures 5.9 and 5.10, indicates that a dispersion-like principle may be obeyed by the transverse mixing process.

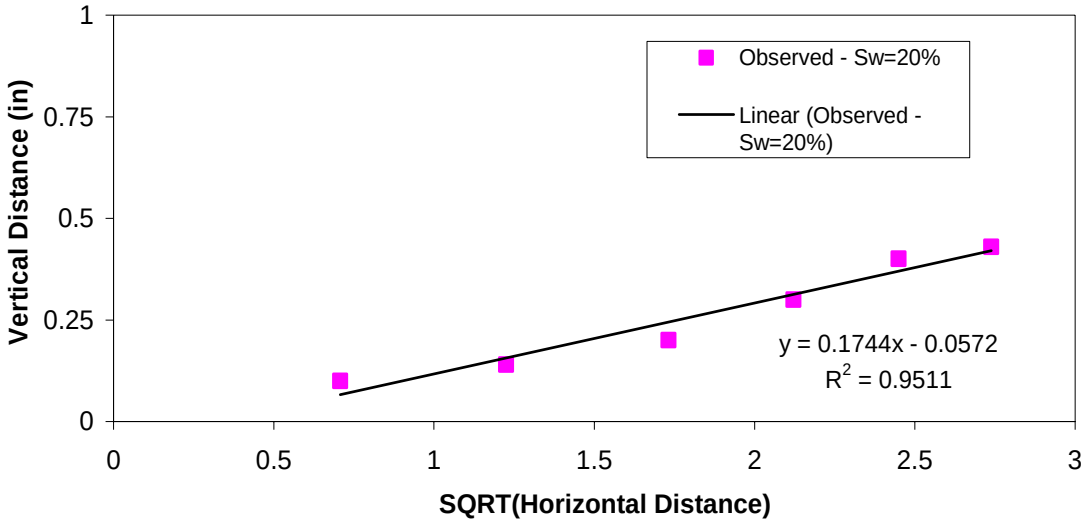

Figure 5.9 Dispersion fit for 0.5 mm glass beads at S_w=20% (Run #sg-1-1)

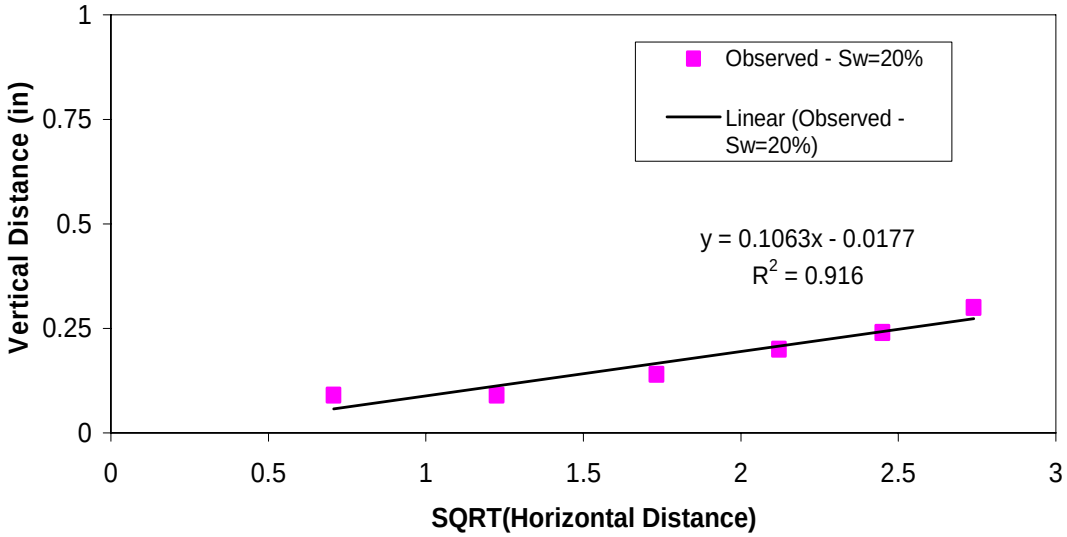

Figure 5.10 Dispersion fit for 0.5 mm glass beads at S_w=50% (Run #sg-1-1)

Shown in Figure 5.11 are plots of vertical water saturations profiles from the experiments. The plots look similar to a typical water saturation distribution in a capillary

pressure transition zone (Figure 5.12). It means that the transverse mixing may be considered an extension of the capillary transition zone.

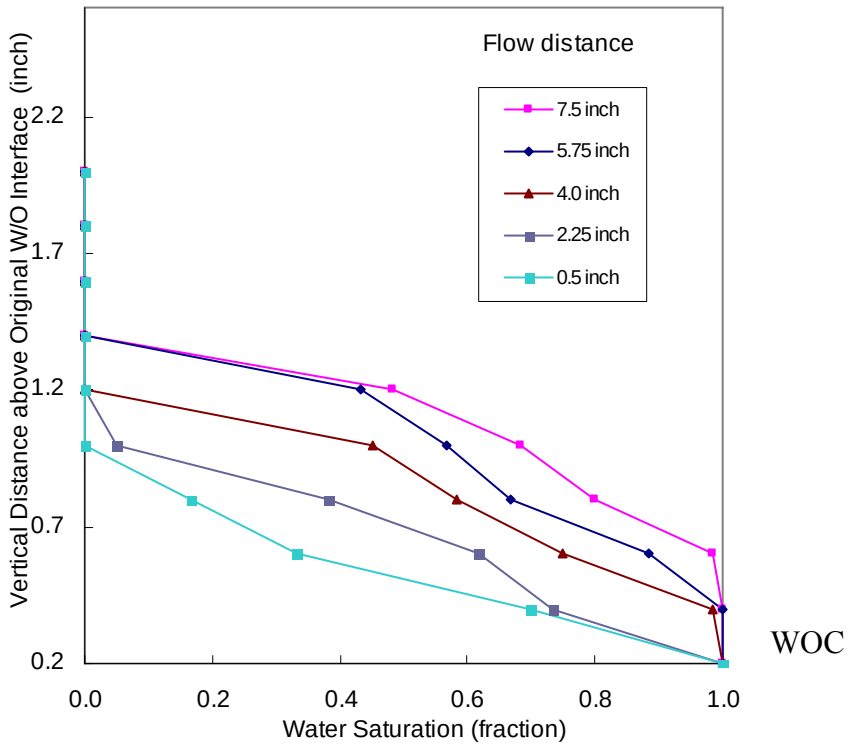

Figure 5.11 Capillary pressure transition zone from simulator (CMG IMEX)

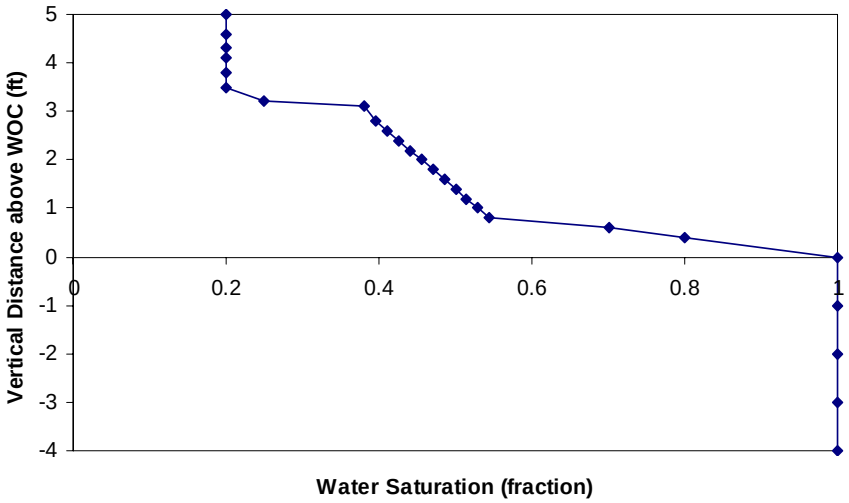

Figure 5.12 Stable water saturation profiles above WOC at different flow distance (Run #lg-1-1 for 1mm glass beads)

5.3.1 Flow Velocity Effect

The interstitial velocities are computed from the measured water and oil flow rates, measured porosity, and flow area in the cell. Within a range of water velocity from 0.08 ft/s to approximately 1.0 ft/s (maximum), transverse mixing begins at the flow distance – 0.5 to 7.5 inch away from the inlets.

To analyze the effect of velocity on intensity of transverse mixing, a slope of transverse mixing is defined as and averaged slope of the iso-saturation plots vs. flow distance. Figures 6.13 to 6.15 show the effect of flow velocity on the transverse dispersion slopes for oil viscosity 2.5 cp. For instance, corresponding to S_w=20%, the slopes reduce from 0.27 to 0.15, to 0.03 for 0.6 mm sa, and 1.0 mm and 0.5 mm glass beads, respectively in Figure 5.13. The slopes for the other two values of water saturation are the largest for the sharp-edged sand, smaller for round glass beads and almost no slope for the smallest glass beads.

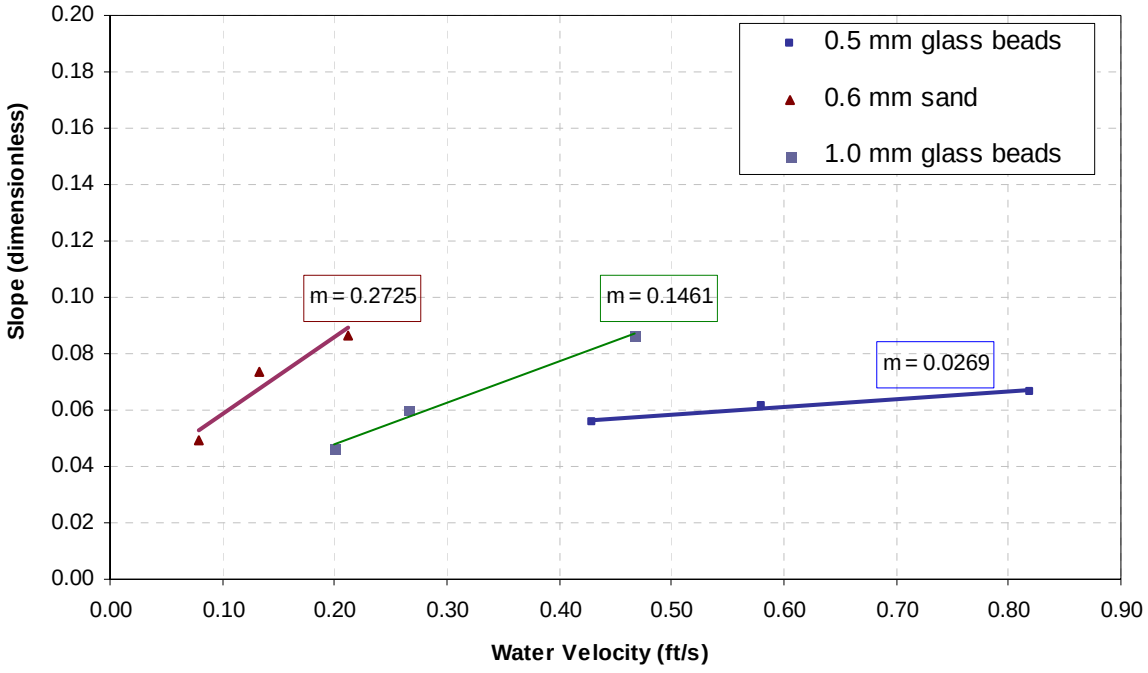

Figure 5.13 Slopes of mixing zone growth vs. water velocity at S_w=20%

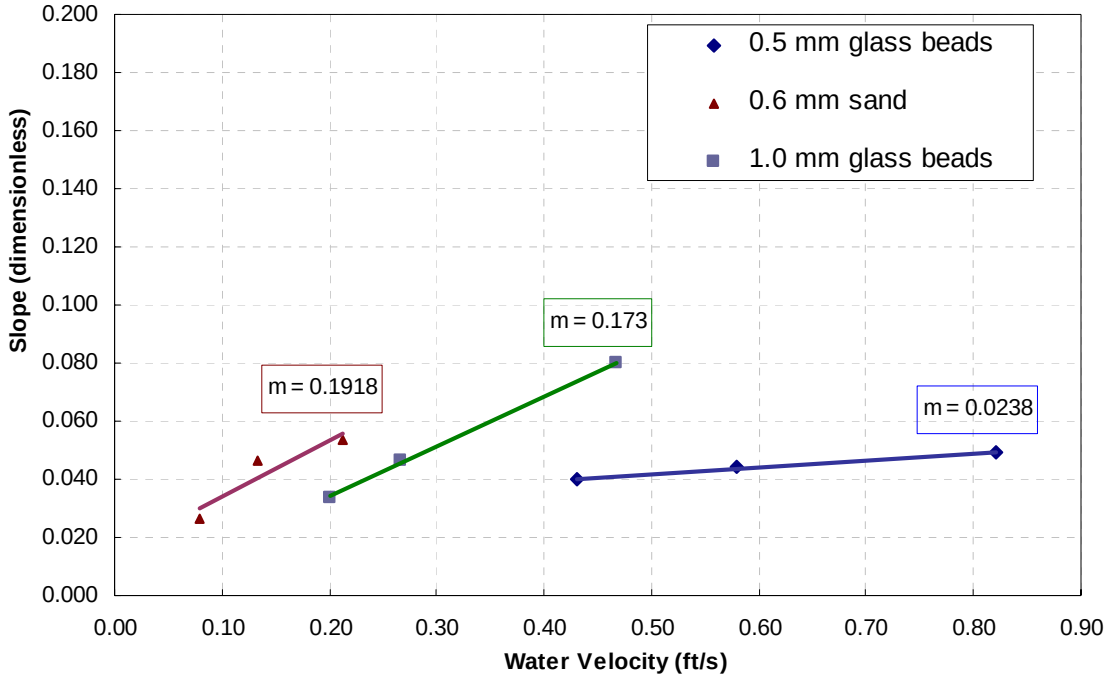

Figure 5.14 Slopes of mixing zone growth vs. water velocity at S_w=50%

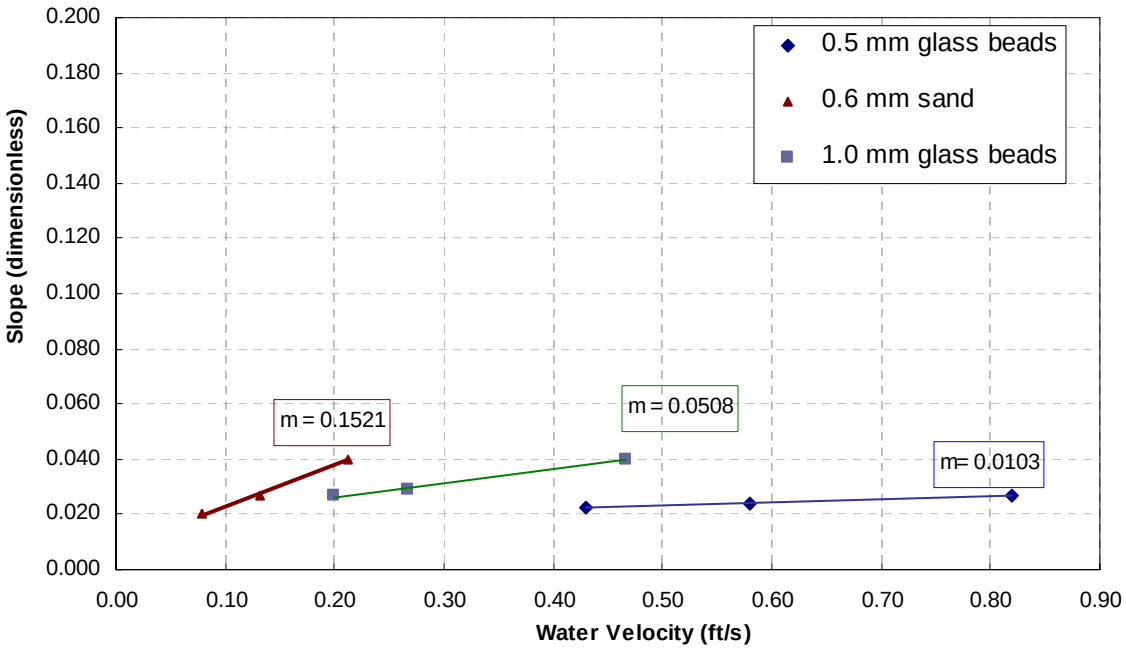

Figure 5.15 Slopes of mixing zone growth vs. water velocity at S_w=80%

Interestingly, as shown in Figure 5.16, the slope of transverse mixing for 1.0 mm glass beads is the maximum at the water velocity of 0.6 ft/s (Run # lg-1-1 to lg-1-5). Data for other water saturation iso-lines consistently indicate the maximum value of the slope within the 0.2

and 1.0 ft/s velocity range. The phenomenon is not observed for the other two granular packs with twice smaller grains. Apparently, the velocities for the two smaller grains are not large enough to capture the entire slope trend.

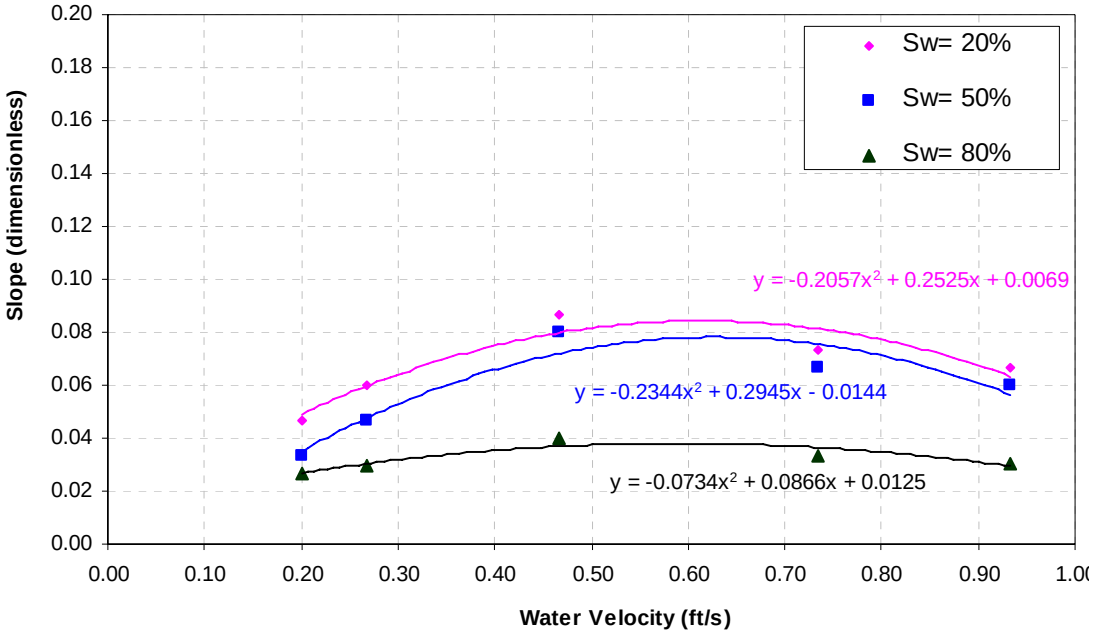

Figure 5.16 Slope of mixing zone growth vs. water velocity at different S_w (1.0 mm)

The change of width of mixing zone with velocity may be explained by displacing patterns in pore scale. For two-phase flow in water-wet rock, Honarpour et al. (1986) described in Figure 5.17, water resides on the grain surface, and flow may remain continuous from throats to throats after collision. Oil, however, may flow in various patterns.

At low velocity, Raimondi and Torcaso (1964) reported that oil might be displaced in a piston-like pattern because oil could continuously flow through pore throats. Therefore, in our experiments at low velocity range, the larger water velocity, the farther oil is displaced, in turn, the larger the transition zone is. However, when the displacing velocity is relatively high, water with higher momentum may break oil streams (Figure C-4, Appendix C), then the discontinuous oil blob may be trapped in throats, and slow down in smaller pores since water may pass through in the larger pore throats. Hence, these trapped and/or slow moving oil blobs (snap-off) may

reduce the water saturation during mixing process. The snap-off condition is discussed as follows.

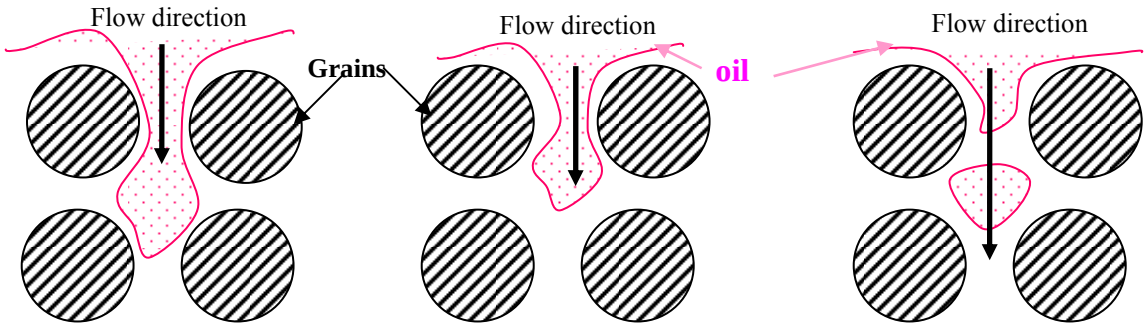

Figure 5.17 Water displacing oil in patterns of continuous oil flow and break-off oil blobs (from left to right) in water-wet rock (After Honarpour et al., 1986)

As fluid flow at relatively high velocity, the eluted part starts to take place. The flow of eluted part is restricted with certain conditions. The eluted part may also be regarded as snap-off. There is a critical capillary pressure (p_c') for snap-off defined by Falls et al. (1988).

$$p_c' - p_c = \frac{a_{so}}{t_{so}} \quad \text{.....(5.3)}$$

Where, a is constant of proportionality, cp

t_{so} is snap-off time, seconds

p_c is capillary pressure, referred to Eq. (3.4)

p_c' should be larger than p_c to form snap-off. The snap-off time (t_{so}) would be longer than the regular flow time. If oil could flow across the structure element, the pressure drop should be equal or bigger than p_c'. The pressure drop may be evaluated using Eq. (2.9). Since the lag time due to snap-off may reduce both water and oil flow, transverse mixing may have slow down at high velocity shown in Figure 5.16.

5.3.2 Grain Size, Shape and Uniformity Effect

Transverse mixing positively correlates with the grain size. Coats and Smith (1964) and Perkins and Johnston (1969) noted that the size of grain may increase the tortuous flow distance and, in

turn, make the mixing zone larger. Fore example, Figure 5.13 shows that for the same velocity of 0.45 ft/s, the 0.5 mm and 1.0 mm bead packs gives of 0.06 and 0.08, slopes of transverse mixing respectively. Being a measure of initial transverse mixing, the slope increases as the mean size of grain increases.

Grain shapes (and uniformity) may further intensify transverse mixing. When the flow in sand is compared with glass beads, a larger mixing may occur, due to variety of sand sizes (Haro, 2007). For the porous media having poorly-sorted grains, e. g., in #2 Q ROK sand (mean size =0.6 mm), the throats are not as uniform as those in glass beads. At the pore scale, there is more variation of direction interstitial velocity and value (due to changing flow area) which further contributes to the mixing. Hence, the transverse mixing slope in the sand should be larger than that for similar size glass beads, when the average flow velocity is the same. In fact, for velocity 0.20 ft/s, the slope for sand is 0.087 vs. 0.05 for glass beads in Figure 5.13, while in Figure 5.14 the same comparison is 0.055 for sand vs. 0.035 for glass beads.

Moreover, the photographs show that iso-saturation lines in the sand pack are not as smooth as the ones in glass beads packs; chaotic shapes of these lines have been observed in the experiments. Obviously, transverse mixing in poorly sorted porous media is complex.

5.3.3 Fluid Viscosity Effect

For equal viscosities of oil and water, a symmetrical growth of water (upwards) and oil (downwards) transition zones was observed by Perkins and Johnston (1969). In their experiments, large total mixing zones were reported for the low viscosity oil, as each fluid invaded the other fluids.

In our experiments, oil viscosity was from 2 to 3-fold larger than water viscosity and only water-in-oil mixing was observed. The viscosity difference controlled velocity difference, which is reportedly a key factor in convective dispersion (Blackwell, 1962). Convective dispersion is a

type of mass transformation inside fluid at high velocity in macroscopic scale. High-viscosity oil always tends to have a low flow rate, in turn, have smaller transverse mixing.

In our experiments, transverse mixing slightly reduces with increasing oil viscosity as shown in Figure 5.18. According to Darcy's Law, the greater the viscosity, the more slowly oil flows. Apparently, transverse velocity in Eq. (5.1) reduces as the dispersed water has to take longer time to flow through the pore throats which are previously occupied by viscous oil. (Viscous oil has larger interfacial tension with water and solid grains.) Moreover, water invasion takes more energy and time to "drag" the discontinued oil blobs through pores and throats. It was observed by Wang *et al*. (2006) that both water and oil relative permeability would decrease when oil viscosity increased. Hence, comparing with less viscous oil, a smaller growth of transverse mixing zone is observed for the same water flowing (residence) time.

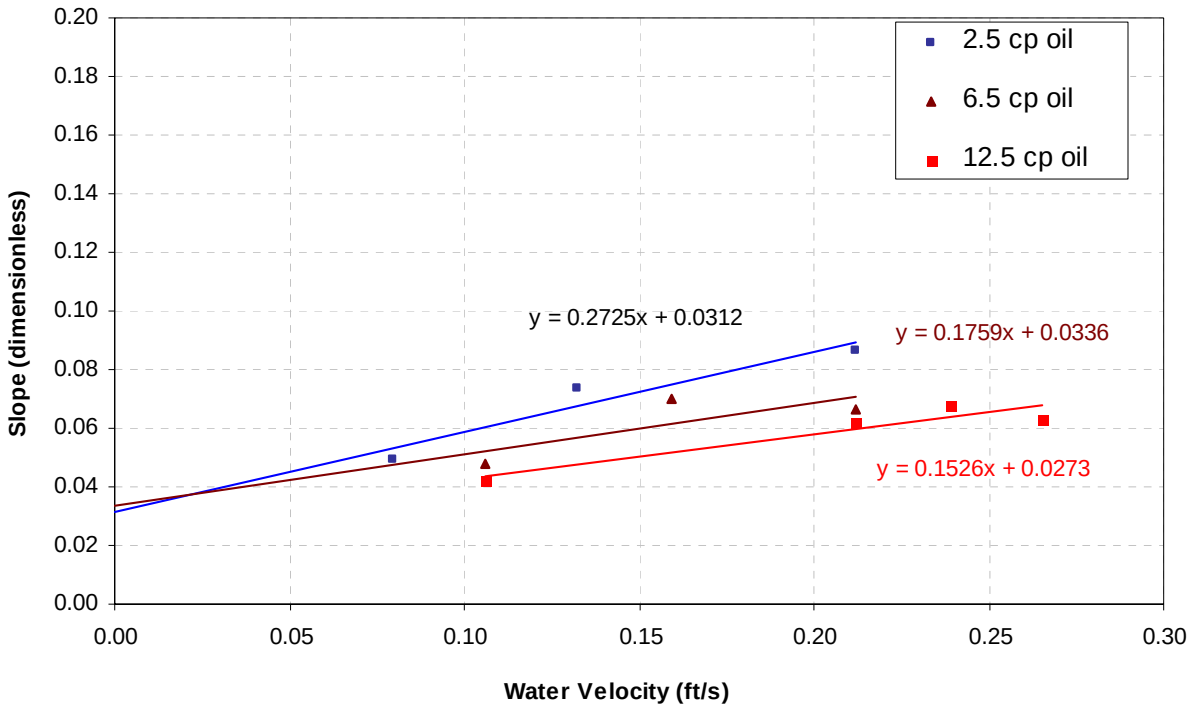

Figure 5.18 Slope of mixing zone growth vs. water velocity at different oil viscosity (include all the cases (Table 5.5) in #2 Q ROK sand experiments)

5.4 Summary

In this study, transverse mixing in porous media was investigated experimentally using granular packs and two immiscible fluids. Experiments of mixing in linear stratified flow with oil and water were analyzed. The following conclusions are drawn:

1. A granular-pack flow cell was built to observe mixing. In all flow experiments, the transverse mixing phenomenon was observed. Its degree, however, was different for oil viscosity, grain size, type and shape, and pressure drop across the cell.
2. In view of the scaling analysis theory, dimensions of the flow cell were sufficient for capturing the onset of transverse mixing. However, only early time transverse mixing is observed because of dimensional effect. The water saturation isolines were impacted by the constricted upper the no-flow boundary and converged at the two outlets. Only first half of the flow cell was considered representative analysis.
3. For all values of different pressure drop across the flow cell and different granular packs, vertical size of mixing transition zone above the initial W/O interface appeared to be proportional to the square root of the flowing distance, i.e. time.
4. Transverse mixing increased with higher flow velocity (pressure gradient) and larger grain sizes. However, higher-viscosity oil reduced mixing effect.

CHAPTER 6

MATHEMATICAL MODEL OF DISPERSED FLOW

This chapter presents a mathematical model to compute water saturation profile developed due to transverse mixing above the oil/water interface. “Mixing” is broadly interpreted here to address the entire range of stirring, splitting, dispersion and diffusion processes between two fluids.

At macroscopic scale, a saturation profile can be modeled by the unsteady diffusion equation. Analogous to a concentration or energy diffusion process, the macroscopic mixing at the interface is determined by the balance between mechanical forces in the transverse direction. The transverse dispersion coefficient (D_T) can be determined using the model for a constant flow velocity and constant water saturation (S_{wooi}) at the initial W/O interface. The analytical solution is also used to predict saturation profiles for various cases using the computed D_T.

6.1 Limitations and General Assumptions

Several limitations and general assumptions for the transverse mixing experiments can be summarized as follows:

The first assumption is that the mechanical dispersion (not molecular diffusion) is similar in the miscible and immiscible fluids (Bird *et al*, 2001). In fluid dynamics, the dispersion phenomenon is characterized by the continuous or cascade splitting of the streamtubes. A general equation of continuity for a multi-component mixture based on control volume is

$$\frac{\partial \rho_\alpha}{\partial t} = -\left(\frac{\partial n_{\alpha x}}{\partial x} + \frac{\partial n_{\alpha y}}{\partial y} + \frac{\partial n_{\alpha z}}{\partial z}\right) + r_\alpha \qquad \alpha = 1,2,3,...,k \quad \text{.....(6.1)}$$

Where,

ρ_α = density of each species

n_α = components of mass flux

r_α = volumetric source/sink terms

It is well-known that the material balance equations for two miscible fluids in x-z plane (see Figure 6.1), in which phase *i* is an injection phase, may be expressed as

$$\phi\frac{\partial C_i}{\partial t}+\frac{\partial}{\partial x}(u_x C_i-\phi K_L\frac{\partial C_i}{\partial x})+\frac{\partial}{\partial z}(u_z C_i-\phi K_T\frac{\partial C_i}{\partial z})=0 \quad \text{.....(6.2)}$$

Where,

u_x, u_z = phase i flowing velocity in x and z directions respectively, [L]/[T]

C_i = phase i's concentration, fraction

K_L, K_T= longitudinal and transverse dispersion respectively, $[L]^2/[T]$

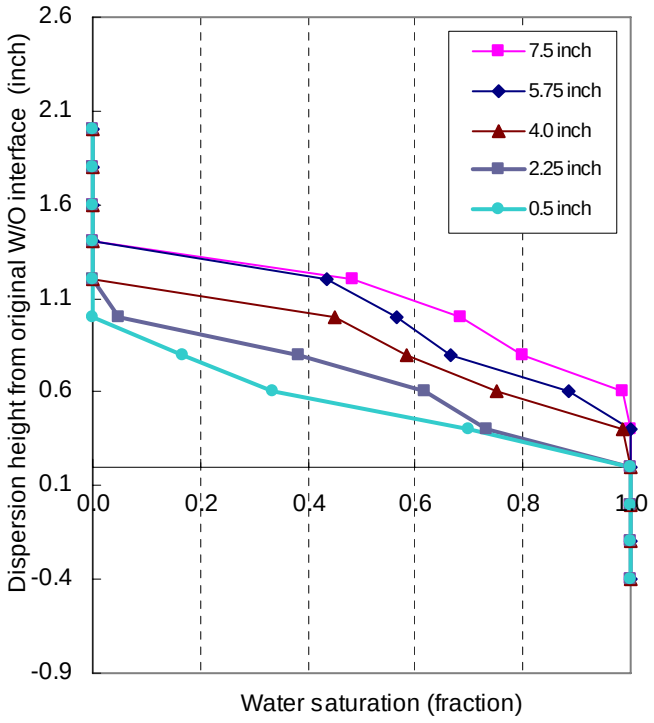

Figure 6.1 Dispersed water saturation profile (Run # sg-1-2 –picture #322)

Following Ewing (2000) and Perkins and Johnston's (1969), concentration changes are similar to saturation changes amongst immiscible fluids. In the same physical domain, when the injected phase *i* is immiscible with the displaced phase, the mass conservation equation can be expressed as

$$\phi \frac{\partial S_i}{\partial t} + \frac{\partial}{\partial x}(u_x S_i - \phi D_L \frac{\partial S_i}{\partial x}) + \frac{\partial}{\partial z}(u_z S_i - \phi D_T \frac{\partial S_i}{\partial z}) = 0 \quad \text{.....(6.3)}$$

Where,

S_i = phase *i*'s saturation, fraction

D_L = immiscible longitudinal dispersion, $[L]^2/[T]$

D_T = immiscible transverse dispersion, $[L]^2/[T]$

Another typical assumption is maintaining saturation at the original interface constant. It has been proposed that the invasion between phases depends on the momentum variance between fluid-fluid impingement and fluid-rock impingement. Transverse mixing starts from this interface. In the experiments, water is less viscous and has higher momentum than oil. The water saturation at original W/O interface is always equal to (1- S_{or} - S_{wi}) at both low and high flow rates (Figures 6.2 and 6.3). In Figure 6.2, the water velocity v_w is 8.2 cm/s, and oil velocity v_o is 3.3 cm/s. In Figure 6.3, v_w is 15.2 cm/s, and oil velocity v_o is 6.1 cm/s.

Therefore, water saturation at the original interface, S_{wooi}, is assumed to be a constant and relatively a higher value. Similarly, if the oil viscosity were to be the same as the water viscosity, oil droplets/globules may disperse into the water streams as well (Perkins and Johnston, 1969). In the latter case, one would observe a rather symmetric transverse dispersion pattern.

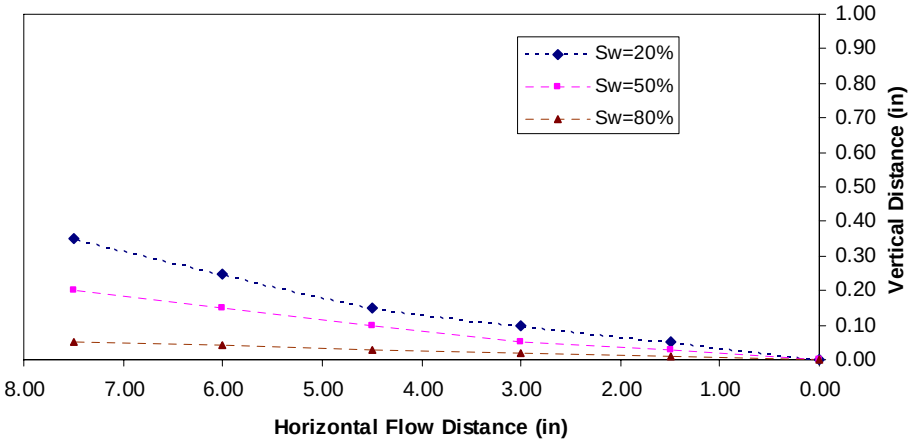

Figure 6.2 Iso-saturation lines at low flow rate Run # lg-1-1 (picture#388)

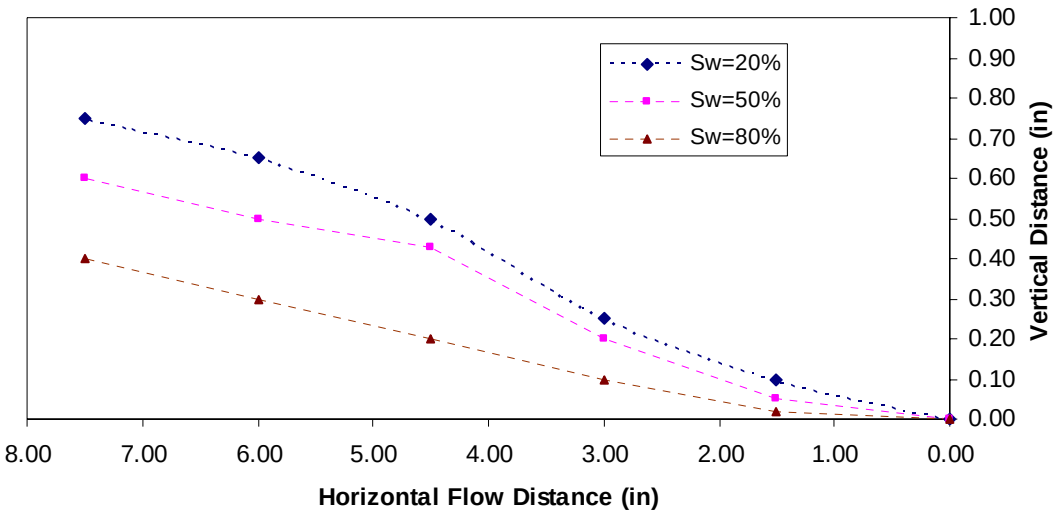

Figure 6.3 Iso-saturation lines at high flow rate Run #lg-1-3 (picture #322)

The third assumption is that the average flow velocity at W/O interface, v, is constant and equal to the arithmetic average of water and oil velocity. For instance, in Figure 6.4, the water and oil velocity are 0.036 and 0.001 cm/s, respectively, and therefore, the W/O interface velocity should be set as 0.0185 cm/s. This average interfacial velocity is consistent with the material balance.

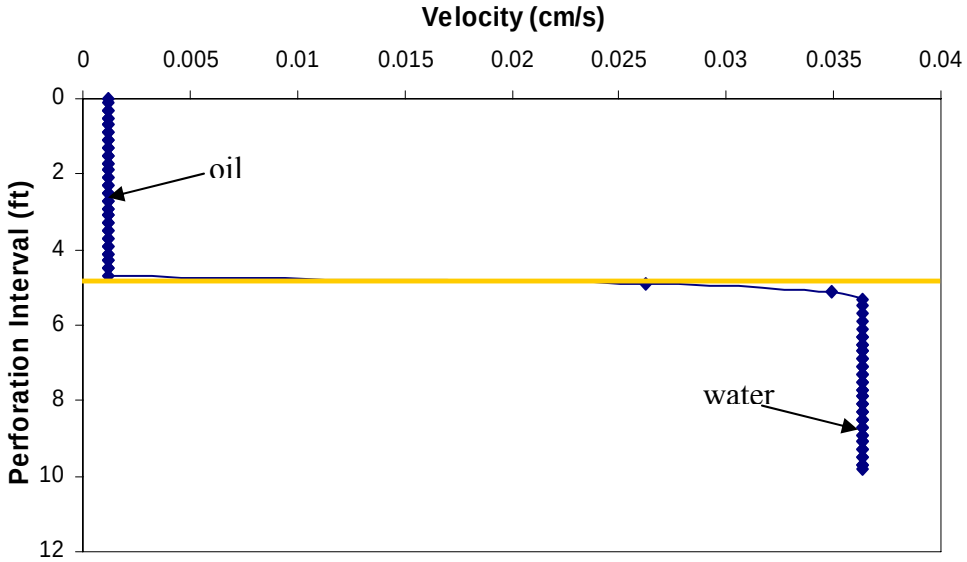

Figure 6.4 Distribution of velocities across O/W interface from numerical simulator

6.2 Mathematical Model of Dispersed Flow

A linear mathematical model is developed here to estimate water saturation distribution and the size of transverse mixing zone.

The model is derived from the assumptions discussed above. Also, it is assumed that available cross-section to each bulk flow path is not affected by the transverse mixing and neither does the bulk flow velocity.

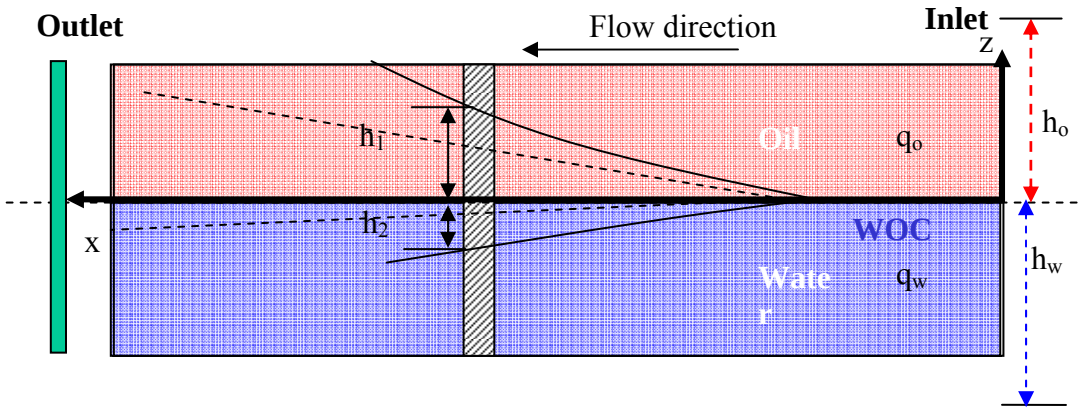

Figure 6.5 Schematic of transverse mixing in a linear model

Given a stratified model of two immiscible fluids, the velocity is constant in the bulk of each phase and no longitudinal dispersion occurs. The vertical velocity is zero, since the vertical pressure equilibrium is maintained. Thus, one obtains the following convection-diffusion type governing equation for the saturation profile.

$$\phi \frac{\partial S_i}{\partial t} + \frac{\partial}{\partial x}(u_x S_i) + \frac{\partial}{\partial z}(-\phi D_T \frac{\partial S_i}{\partial z}) = 0 \quad \text{.....(6.4)}$$

For fully developed flow regime (away from the inflow or outflow boundary effects), we may assume that the change of saturation in longitudinal direction is negligible and hence leads to the following simplified governing equation.

$$D_T \frac{\partial^2 S_w}{\partial z^2} = \frac{\partial S_w}{\partial t} \quad \text{.....(6.5)}$$

Boundary condition (1): $S_w(0,t) = S_{wooi}$ …….(6.6)

Boundary condition (2): $S_w(\infty,t) = S_{wc}$ ……..(6.7)

Initial condition: $S_w(z,0) = S_{wc}$ ……...(6.8)

S_{wooi} in the computations is approximately a constant value (= 0.9), which is the observed water saturation at and below static OWC in the flow cell, so that

$S_{wooi} = 1 - S_{or}$

Let's also define mobile water saturation in oil zone, S_{wm}, Where,

$S_{wm} = S_w - S_{wc}$ ……...(6.9)

Eq. (6.5) becomes $D_T \frac{\partial^2 S_{wm}}{\partial z^2} = \frac{\partial S_{wm}}{\partial t}$ ……...(6.10)

Eq. (6.6) becomes $S_{wm}(0,t) = S_{wooi} - S_{wc}$ ……..(6.11)

Eq. (6.7) becomes $S_{wm}(\infty,t) = S_{wc} - S_{wc} = 0$ …….(6.12)

Eq. (6.8) becomes $S_{wm}(z,0) = S_{wc} - S_{wc} = 0$ …….(6.13)

In order to solve this second-order partial differential equation, the Laplace transform of function S_w in Eq. (6.5), is defined for all real numbers $t \geq 0$, is the function U(z), defined by,

$U(z) = \int_0^\infty e^{-st} S_w dt$ …….....(6.14)

Where, s = Laplace / (complex) frequency variable, second^{-1}.

t = flow time, second. $t = \frac{|x_0 - x|}{v}$

x_0=coordinate of transverse mixing onset

v=constant velocity at OWC

After Laplace transfer, Eq. (6.5) becomes

$sU(z) - S_{wm}(0) = D_T \frac{d^2 U(z)}{dz^2}$ …….(6.15)

Eq. (6.11) becomes

$$U(0,t) = \frac{S_{wooi} - S_{wc}}{s} \quad \text{……..(6.16)}$$

Eq. (6.12) becomes

$$U(\infty,t) = 0 \quad \text{…….(6.17)}$$

Eq. (6.13) becomes

$$U(z,0) = 0 \quad \text{…….(6.18)}$$

Where, $S_{wm}(0)$ is the initial value.

$$sU(z) = D_T \frac{d^2U(z)}{dz^2} \quad \text{…….(6.19)}$$

Let, $\frac{dU}{dz} = Y$ and apply the chain rule to the right-hand side of Eq. (6.19)

$$D_T \frac{d^2U(z)}{dz^2} = D_T \frac{dY}{dz} = D_T \frac{dY}{dU}\frac{dU}{dz} = D_T Y \frac{dY}{dU} \quad \text{……(6.20)}$$

Substitute Eq. (6.20) into Eq. (6.19),

$$sU(z) = D_T Y \frac{dY}{dU}$$

$$\frac{1}{2}sU^2 = \frac{1}{2}D_T Y^2 - C_1$$

$$Y = \sqrt{\frac{sU^2 + 2C_1}{D_T}} \quad \text{…….(6.21)}$$

Substitute the assumption to (6.21),

$$\frac{dU}{dz} = \sqrt{\frac{sU^2 + 2C_1}{D_T}} \quad \text{…….....(6.22)}$$

Integrate Eq. (6.22), $\int \frac{dU}{\sqrt{\frac{sU^2 + 2C_1}{D_T}}} = \int dz$ …….....(6.23)

$$\int \frac{dU}{\sqrt{(\sqrt{\frac{s}{D_T}}U)^2 + \frac{2C_1}{D_T}}} = \int dz \quad \text{.....(6.24)}$$

C_1 is always a positive number. In case that $2C_1/D_T$ is a negative value, the solution will become trivial when infinite z boundary condition is applied; the procedure is not included here.

So, set C_1^{*2} equal to $2C_1/D_T$ and insert $\sqrt{\frac{s}{D_T}}$ on both sides of Eq. (6.24),

$$\int \frac{d(\sqrt{\frac{s}{D_T}}U)}{\sqrt{(\sqrt{\frac{s}{D_T}}U)^2 + C_1^{*2}}} = \sqrt{\frac{s}{D_T}} \int dz \quad \text{.....(6.25)}$$

Integrate right side of Eq. (6.25),

$$\int \frac{d(\sqrt{\frac{s}{D_T}}U)}{\sqrt{(\sqrt{\frac{s}{D_T}}U)^2 + C_1^{*2}}} = \sqrt{\frac{s}{D_T}}z + C_2 \quad \text{.....(6.26)}$$

Integrate left side of Eq. (6.26), we get

$$\text{Sinh}^{-1}\left(\frac{\sqrt{\frac{s}{D_T}}U}{C_1^*}\right) = \sqrt{\frac{s}{D_T}}z + C_2 \quad \text{.....(6.27)}$$

Then switch the $\sinh^{-1}$ to right side of Eq. (6.27)

$$\left(\frac{\sqrt{\frac{s}{D_T}}U}{C_1^*}\right) = \text{Sinh}\left(\sqrt{\frac{s}{D_T}}z + C_2\right) \quad \text{.....(6.28)}$$

Change the form of sinh to exponential expression

$$\left(\frac{\sqrt{\frac{s}{D_T}}U}{C_1^*}\right) = \frac{e^{\left(\sqrt{\frac{s}{D_T}}z + C_2\right)} - e^{-\left(\sqrt{\frac{s}{D_T}}z + C_2\right)}}{2} \quad \text{.....(6.29)}$$

Then, we get the solution of U,

$$U = \frac{\overline{C}_1 e^{(\sqrt{\frac{s}{D_T}}z)} - \overline{C}_2 e^{-(\sqrt{\frac{s}{D_T}}z)}}{2\sqrt{\frac{s}{D_T}}} \quad \text{.....(6.30)}$$

As z approaches infinity, e^z goes to infinity. Therefore, $\overline{C}_1$ term would be equal to 0 for U to be finite.

Substitute boundary condition Eq. (6.16) to Eq. (6.30)

$$\frac{S_{wooi} - S_{wc}}{s} = \frac{\overline{C}_2}{2\sqrt{\frac{s}{D_T}}} \quad \text{.....(6.31)}$$

We obtain

$$\overline{C}_2 = \frac{2(S_{wooi} - S_{wc})}{s}\sqrt{\frac{s}{D_T}} \quad \text{.....(6.32)}$$

Substitute Eq. (6.32) to (6.30)

$$U = \frac{(S_{wooi} - S_{wc})e^{-(\sqrt{\frac{s}{D_T}}z)}}{s} \quad \text{.....(6.33)}$$

Use the inverse Laplace transform and solve the equation,

$$S_{wm} = (S_{wooi} - S_{wc})\text{erfc}(\frac{z}{2\sqrt{D_T t}}) \quad \text{.....(6.34)}$$

Considering Eq. (6.9) gives water saturation

$$S_w = S_{wc} + (S_{wooi} - S_{wc})\text{erfc}(\frac{z}{2\sqrt{D_T t}}) \quad \text{.....(6.35)}$$

Eq. (6.35) can also be written as

$$S_w = S_{wooi} - (S_{wooi} - S_{wc})\text{erf}(\frac{z}{2\sqrt{D_T t}}) \quad \text{.....(6.36)}$$

Also, considering distance in x-coordinate the equation Eq. (6.36) becomes (6.37)

$$S_w = S_{wc} + (S_{wooi} - S_{wc})\,\mathrm{erfc}\left(\frac{z}{2\sqrt{D_T \frac{(x_0 - x)}{v}}}\right) \quad \ldots\ldots(6.37)$$

According to Eq. (6.35) or (6.36), S_w will gradually increase with flowing time. From the property of error function, S_w will decrease rapidly with increasing z.

6.3 Comparison with the Experimental Results

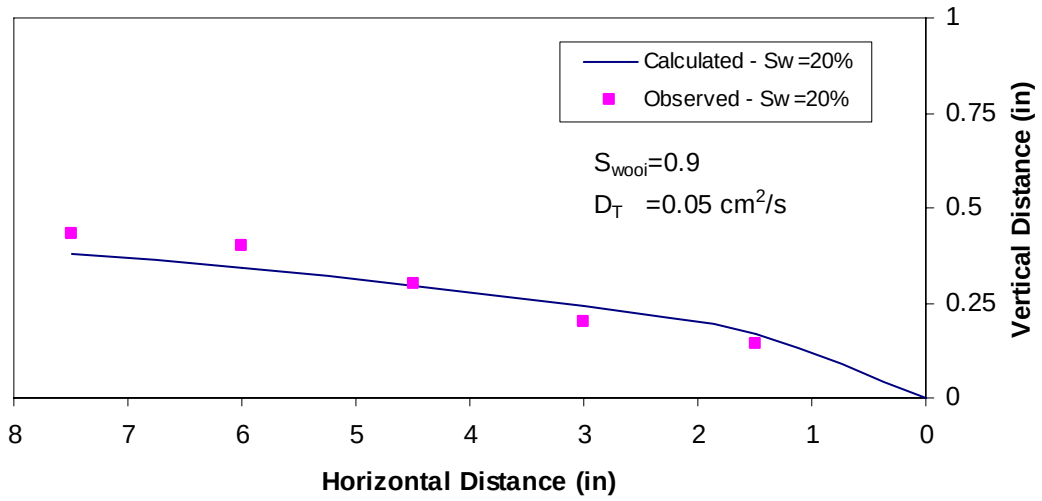

Figure 6.6 Matching experimental data of S_w=20% (Run # sg-1-1)

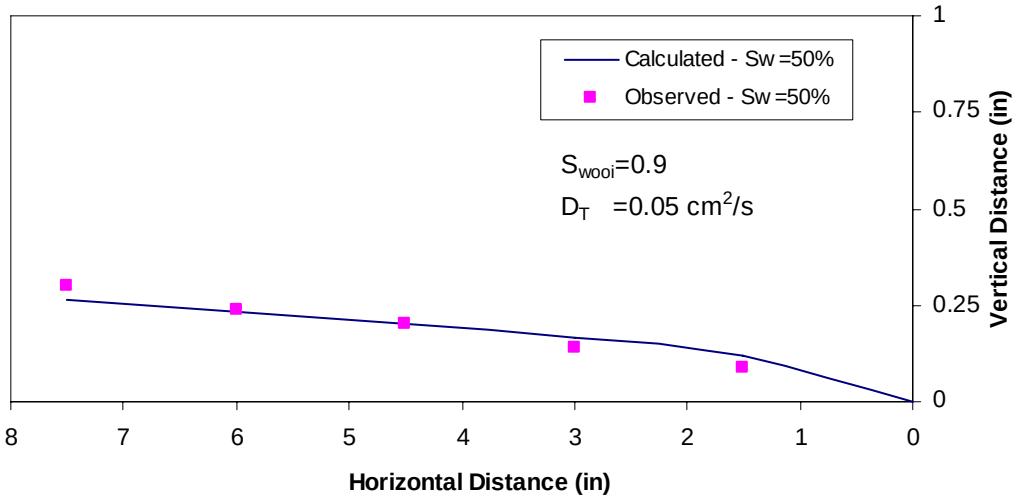

Figure 6.7 Matching experimental data of S_w=50% (Run # sg-1-1)

Formula (6.35) has been matched with against the water saturation data from the experiments. An example is shown in Figure 6.6 and 7.7. Figure 6.6 matches satisfactorily with

the observed mixing profile for the water saturation of 20%. Figure 6.7 shows another comparison when water saturation is 50%. The relative error is approximately 10% in these reported results. The average error of profile matching for glass beads experiments is less than 10%. The maximum error of matching profile is in sand, which is about ±15%.

6.4 Dependence of Mixing Zone on Péclet Number

Bijeljic and Blunt (2006) reported that miscible dispersion in porous media needs sufficient time or distance to obtain observable spreading in the longitudinal and transverse directions. As discussed earlier, dispersion process in miscible and immiscible fluids have similar patterns. To evaluate the transverse dispersion for immiscible fluids, a modified Péclet number, is defined as the ratio of the advection to dispersion rate,

$$N_{Pe}' = \frac{vL}{D_T} \quad \text{.....(6.38)}$$

Where, D_T = transverse dispersion, cm^2/s

In Equation 6.38, the ratio of flow velocity in the mixing zone to the transverse dispersion coefficient is relatively constant. Therefore, the Péclet number increases with the flow distance L and a developed mixing zone may be observed at the macroscopic scale (Bijeljic and Blunt, 2006).

6.5 Solution Discussion

Parametric study of the solution (Eq. 6.35) of dispersion coefficient is discussed. Effects of flow distance, initial water saturation, and interaction of both parameters are investigated. All the data are cited from Perkins and Johnston (1969) since there is no mismatch in their experimental results. The original values of experimental results are listed in Table 6.1. Then, values of flow parameters for various runs are shown as well. Based on the solution of Eq. (6.35), it is observed that the transition zone size increases with an increasing flow distance (L) (Fig. 6.8). Further, S_w depends on the saturation (S_{wooi}) at WOC if the flow distance is the same, but the vertical size of

transition zone does not change (Fig. 6.9). The dispersed water droplets migrate farther in the vertical direction increasing the mixing zone size while both parameters (flow distance and water saturation) are increased (Fig. 6.10).

Table 6.1 Sensitivity Testing Matrix

Parameter	Test						
	1	2	3	4	5	6	7
Flow length, cm	10	50	100	200	200	100	200
Water saturation at original W/O interface (S_{wooi}), fraction	0.5	0.5	0.5	0.5	0.6	0.6	0.7
Flow velocity (v), cm/s	0.014						
Transverse dispersion coefficient (D_T), cm^2/s	0.0014						
Connate water saturation (S_{wc}), fraction	0.2						

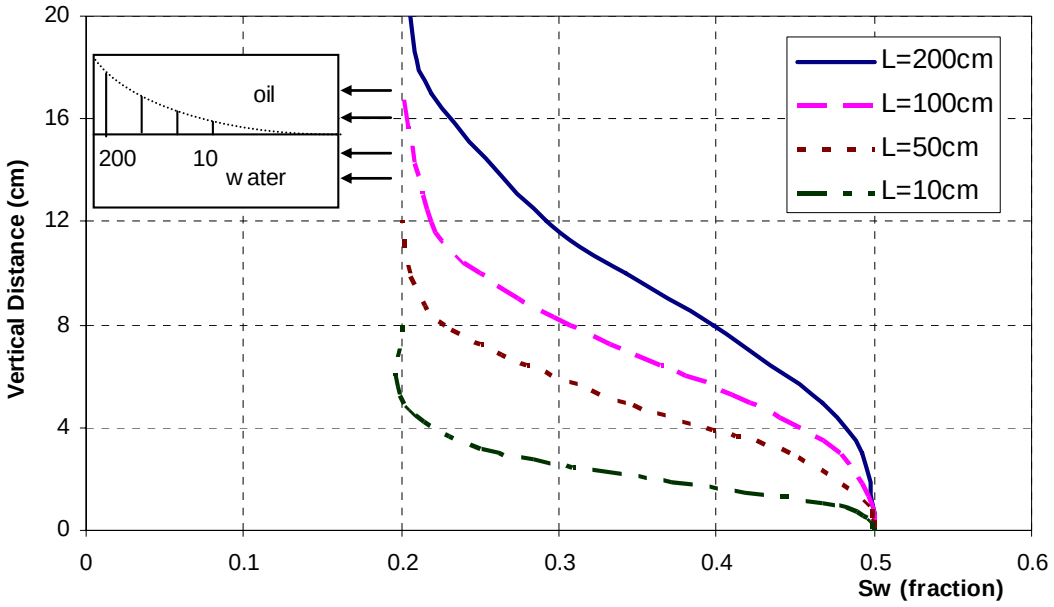

Figure 6.8 Vertical distribution of water saturation at different longitudinal positions while varying flow length

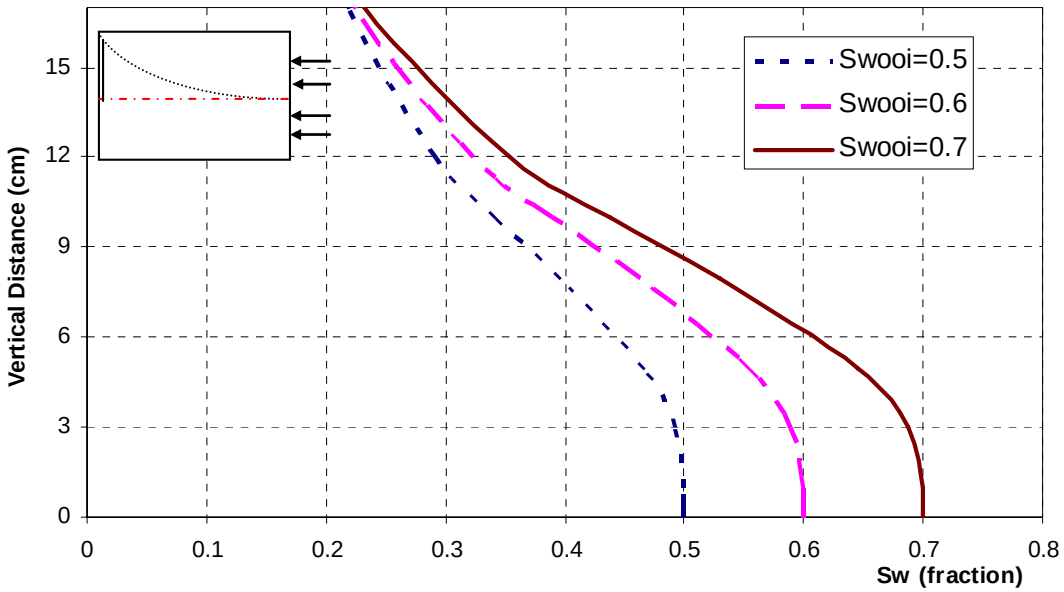

Figure 6.9 Vertical distribution of water saturation at observation station (L= 200 cm from inlet) while varying boundary water saturation

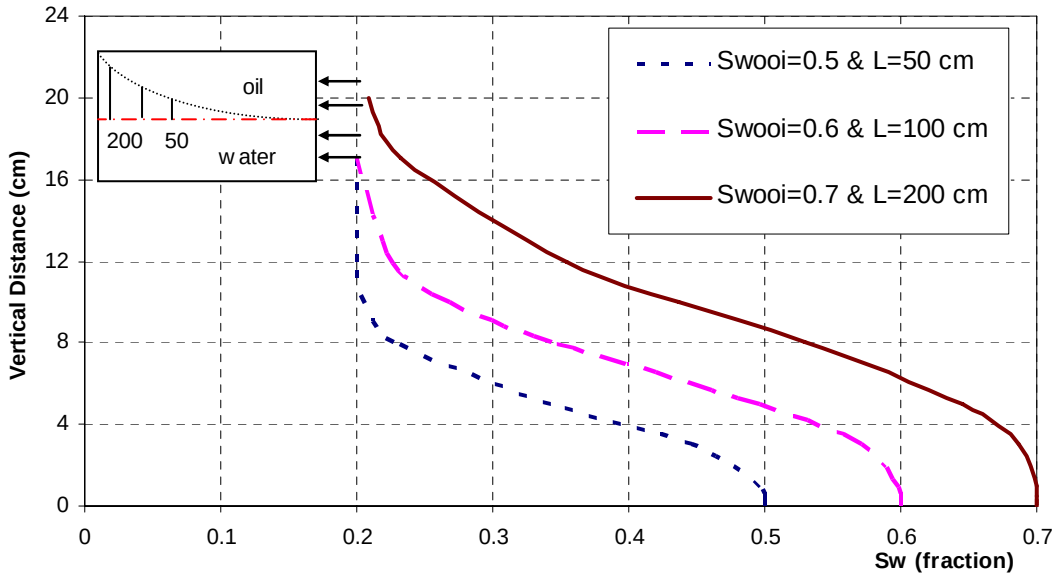

Figure 6.10 Variation of water saturation with vertical distance at different lateral distances for different boundary water saturations

6.6 Alternative Dispersion Model of Transverse Mixing in Linear Flow

An alternative linear-flow model is developed using separation of variables method. The approach appeared to be simpler mathematically and provided an interesting new alternative to computations based on the model derived in **6.2**. An analytical solution is obtained for a 1-D

dispersion model (Figure 6.5). Based on the discussions, the governing equation is the same as Eq. (6.10) with the definition of mobile water saturation, $S_{wm.}$

Boundary conditions are the same as the linear model for the mobile water saturation. They are

$$S_{wm}(0,t) = S_{wooi} - S_{wc} \quad \text{.....(6.39)}$$

$$S_{wm}(\infty,t) = S_{wc} - S_{wc} = 0 \quad \text{.....(6.40)}$$

$$S_{wm}(z,0) = S_{wc} - S_{wc} = 0 \quad \text{.....(6.41)}$$

In the experiments with high viscosity oil, only water invades into oil layer. The observation reflected by the second assumption in 6.1.

Let's assume function S_{wm} to be a product of two single-variable functions, Z and T as

$$S_{wm} = Z(z)T(t) \quad \text{.....(6.42)}$$

$$ZT' - D_T Z'' T = 0 \quad \text{.....(6.43)}$$

$$ZT' = D_T Z'' T \quad \text{.....(6.44)}$$

$$\frac{T'}{D_T T} = \frac{Z''}{Z} = \lambda \quad \text{.....(6.45)}$$

Two partial differential equations

$$\begin{cases} \dfrac{d^2 Z}{dz^2} = \lambda Z \\ \dfrac{dT}{T} = \lambda D_T dt \end{cases} \quad \text{.....(6.46)}$$

Solve two ordinary differential equations in Eq. (6.46) separately (Paul Dawkins, 2001), and substitute the results to Eq. (6.42), the solution for the governing equation (6.10) is

$$S_{wm} = (C_1 e^{\sqrt{\lambda} z} + C_2 e^{-\sqrt{\lambda} z})(e^{\lambda D_T t} + C_3) \quad \text{.....(6.47)}$$

Then, considering $S_w = S_{wm} + S_{wc}$

$$S_w = S_{wc} + (C_1 e^{\sqrt{\lambda} z} + C_2 e^{-\sqrt{\lambda} z})(e^{\lambda D_T t} + C_3) \quad \text{.....(6.48)}$$

Where, $t = \frac{x}{v}$

In this condition, λ is a separation constant. C_3 is -1 from initial condition. Using boundary condition, C_1 is zero; C_2 is $S_{wooi} - S_{wc}$; But λ can not be solved because no effective boundary condition can constrain it to a unique solution. So, to find the other constant coefficients, the observed data points in experiments (Run # sg-1-1) are used to compute the constant coefficients λ and D_T. For this particular run, we have $\lambda = 420$, and $D_T = 0.05$ cm^2/sec. So, approximate solution for this water saturation distribution at Run #sg-1-1 is

$$S_w = (0.9e^{-20.5z})(e^{3.3t} - 1) \quad \text{.....(6.49)}$$

Figure 6.11, comparison of the theoretical water saturations, from the alternative model with the error function model, Eq. (6.35) for Run # sg-1-1 at S_w=20% shows reasonably similar results in the early-time mixing.

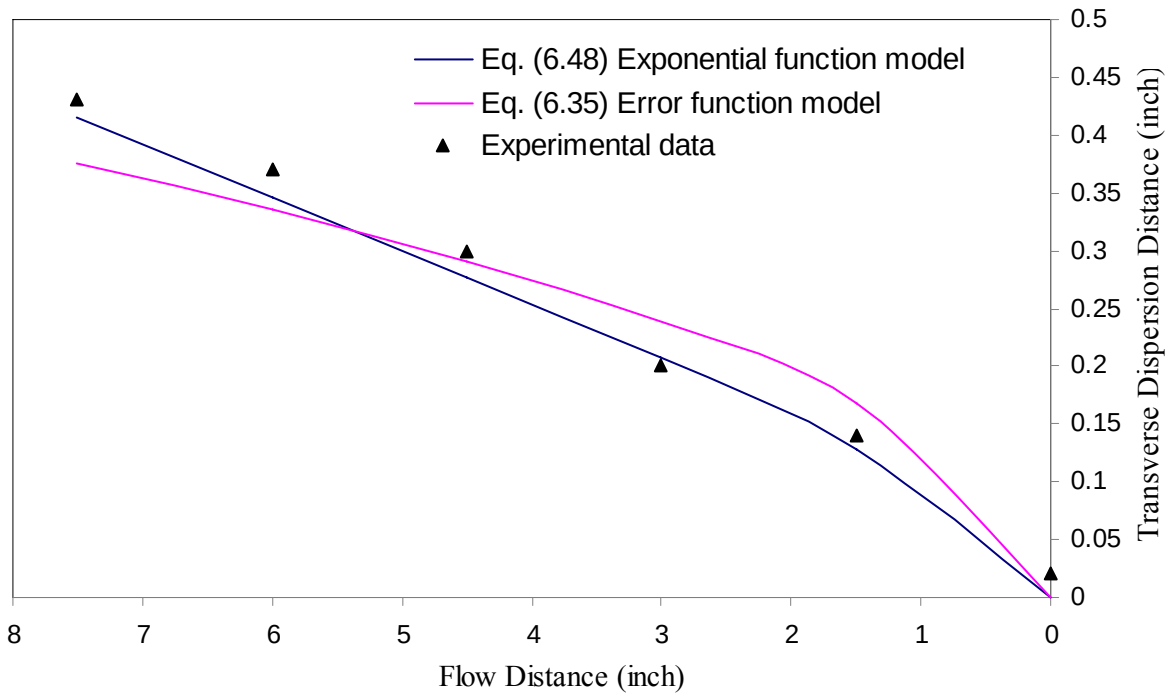

Figure 6.11 Comparison of two linear transverse models for data from Run # sg-1-1

6.7 Summary

1. Several underlying assumptions and typical boundary conditions for the mixing experiments are discussed and critically evaluated.
2. A simplified macroscopic model for transverse mixing has been analytically derived. The model defines a transverse dispersion coefficient.
3. The mathematical model matches reasonably well the experimental results of early transverse mixing. Also the model provides a simple method to determine transverse dispersion coefficient (D_T) from these experiments.
4. An alternative linear-flow model is developed using separation of variables method. The completely different solution shows a similar match to the early time experimental results as the error function solution.

CHAPTER 7

EXPERIMENTAL DATA ANALYSIS

This chapter presents computations of the immiscible transverse dispersion coefficient (D_T) and discussion of the implications and validity. From the linear relationship of D_T and velocity, transverse dispersion is scaled and pseudo-dispersivity is defined. Moreover, error analysis of D_T computation shows that the error of D_T increases for the experimental runs with higher fluid velocity. The computed error allows estimation of the most likely range of dispersivity.

7.1 Computation of D_T

The coefficient of D_T has been determined applying the results from several experimental runs by fitting the analytical model of Eq. (6.35) using an iterative procedure as follows:

1. Draw/select S_w isoline in a photograph;
2. Determine value of S_{wooi} from photographs, it is approximately 0.9 in most of our experiments since small amount of oil may trapped in mixing process;
3. Select at least 5 points on the isoline, and get each point's coordinate - (x, z) in the range of flow distance 7.5 inch from inlets;
4. Compute average velocity of water and oil;
5. Compute flowing time, t, for each point (z, t);
6. Find the best fit of S_w values computed for measured values using Eq. (6.35), output the value of D_T.

In the above procedure, the average velocity was computed using bulk velocity values from Table 6.5. A relatively good match has been observed for most runs as discussed (see Figure 6.6 and 6.7) in Chapter 6. The input data and resulting values of D_T are shown in Table

7.1. Note that S_{wooi} in the computations is approximately a constant value – 0.9, which is observed from the experimental results.

Table 7.1 Dispersion parameters' evaluation in grain pack experiments (S_w=20%)

Grain Type	Oil Viscosity	Run #	Average Velocity at Interface (cm/s)	Transverse Dispersion D_T (cm^2/s)
0.5 mm glass beads	2.5 cp oil	sg-1-1	9.17	0.06
		sg-1-2	12.37	0.10
		sg-1-3	17.50	0.17
	6.7 cp oil	sg-2-1	8.07	0.03
		sg-2-2	10.59	0.08
		sg-2-3	12.11	0.11
	12.5 cp oil	sg-3-1	3.32	0.00
		sg-3-2	5.21	0.01
		sg-3-3	13.27	0.02
#2 Q ROK sand	2.5 cp oil	s-1-1	1.70	0.01
		s-1-2	2.83	0.02
		s-1-3	4.53	0.06
	6.7 cp oil	s-2-1	1.86	0.01
		s-2-2	2.79	0.01
		s-2-3	3.72	0.01
	12.5 cp oil	s-3-1	1.75	0.00
		s-3-2	3.49	0.01
		s-3-3	3.93	0.01
		s-3-4	4.37	0.01
1.0 mm glass beads	2.5 cp oil	lg-1-1	4.27	0.02
		lg-1-2	5.76	0.04
		lg-1-3	10.03	0.11
		lg-1-4	15.58	0.16
		lg-1-5	19.84	0.18

7.2 Scaling of Transverse Dispersion Coefficient (D_T)

Computed values of D_T have been correlated with average velocities values. Example correlation plots are shown in Figures 7.1, 7.2, and 7.3. Linear relationship is quite evident and has been observed in most experiments.

From the linear relationship of flow velocity and dispersion coefficients, a pseudo-dispersivity can be defined as,

$$D_T = \alpha' v \quad \text{.....(7.1)}$$

Moreover, the plot in Figure 7.4 shows that pseudo-dispersivity increases with increasing size of the particles. Its values for particle size 0.5, 0.6 and 1.0 are 0.0126, 0.0139, and 0.0186 cm, respectively.

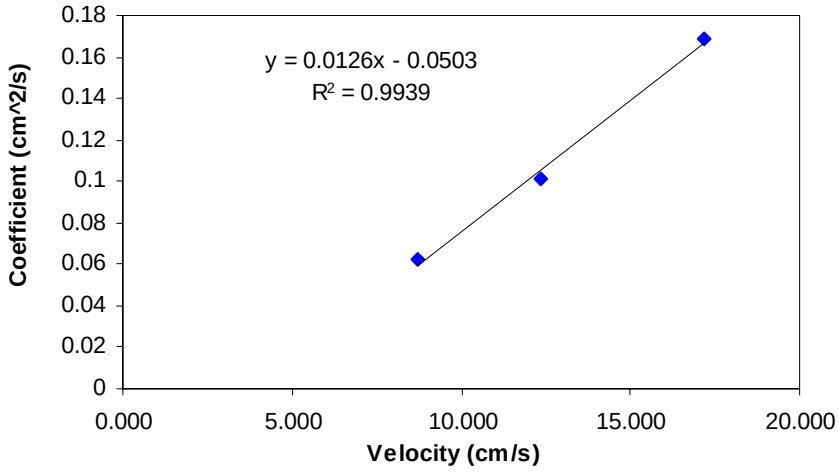

Figure 7.1 Coefficient D_T vs. average velocity for 0.5 mm glass beads at 20% water saturation

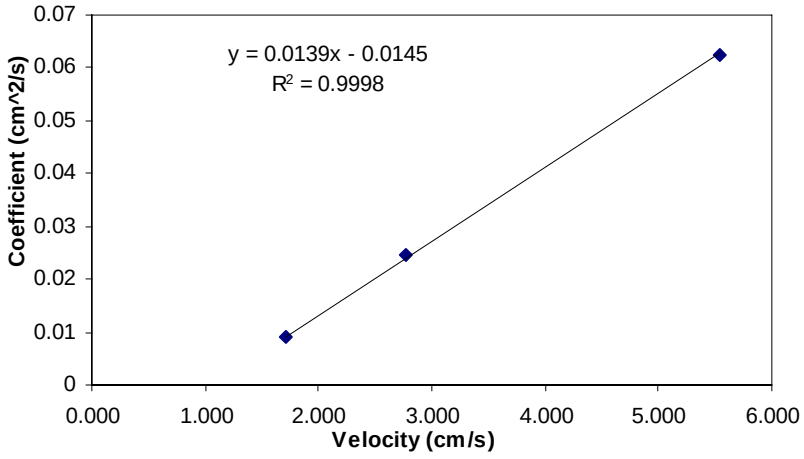

Figure 7.2 Coefficient D_T vs. average velocity for #2 Q Sand at 20% water saturation

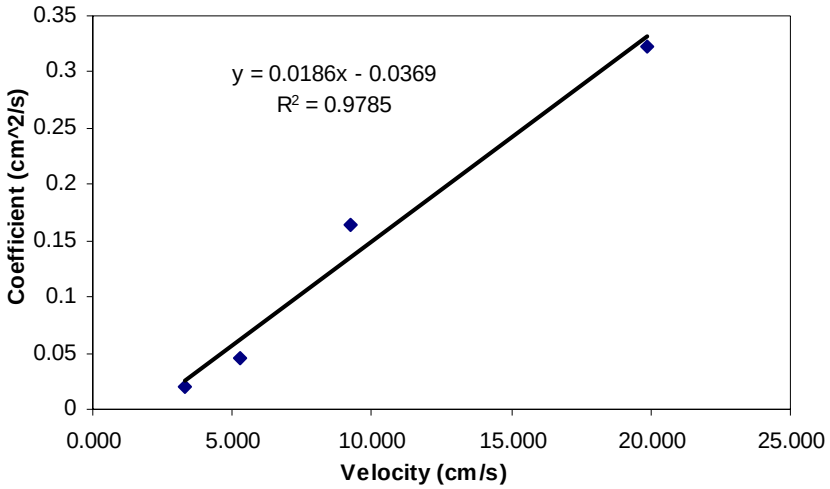

Figure 7.3 Coefficient D_T vs. average velocity for 1.0 mm glass beads at 20% water saturation

Because the size of grains has linear relationship with α', immiscible dispersion becomes somewhat analogous to miscible dispersion (Coats and Smith, 1964). If the grains of a porous medium are homogeneous, the dispersion coefficient can be predicted using the following linear regression equation.

$$D_T = C_D D_P v = 0.119 D_P v \quad \text{.....(7.2)}$$

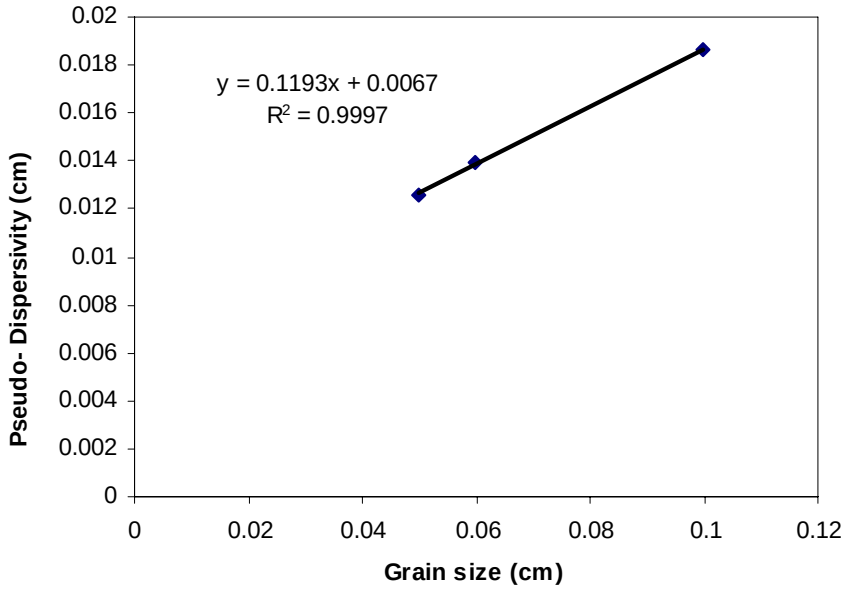

Figure 7.4 Pseudo-dispersivity vs. grain size (related to Figures 7.1 – 7.3)

7.3 Error Analysis

To analyze the error of computed D_T, the following steps:

1. Select S_w isolines from flow experiments with the same granular media, pressure drop across the cell and oil velocity;
2. Determine values of D_T for each S_w isoline;
3. Consider the minimum, maximum, and mean values of D_T;
4. Repeat steps 1 through 3 for all granular media, pressure drops, and oil viscosities.
5. Determine maximum error of dispersivity (α') using maximum and minimum values of D_T and velocity and relationship to D_T (e.g. Eq. 7.1).

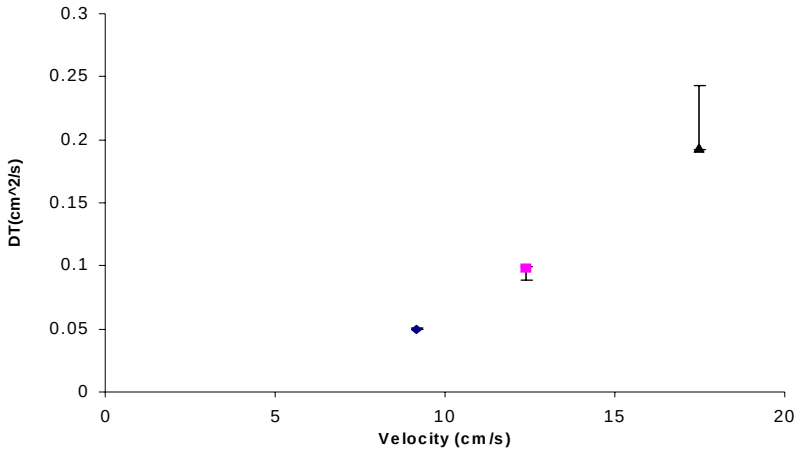

Figure 7.5 Error analysis of D_T in 0.5 mm glass beads (2.5 cp oil)

The plot of D_T error in Figure 7.5 indicates a linearity of D_T values (minimum and maximum) with velocity and loss of precision for higher velocities in Figure 7.5. Standard deviation values are 0.002 and 0.06 cm^2/s for small (9.2 cm/s) and large (17.5 cm/s) water velocities. The increase of error with velocity may result from flow change and high Reynolds number in water flow. Reynolds number is much larger than 100 when water flows at 25 cm/s in 0.5 mm glass beads. However, the water flow Reynolds numbers are smaller than 100 in other two tests shown in Table 7.2. Note that the additional pressure drawdown in longitudinal

direction due to turbulence may reduce the vertical pressure difference, in turn, reduce the magnitude of transverse mixing (refer to Figure 2.3).

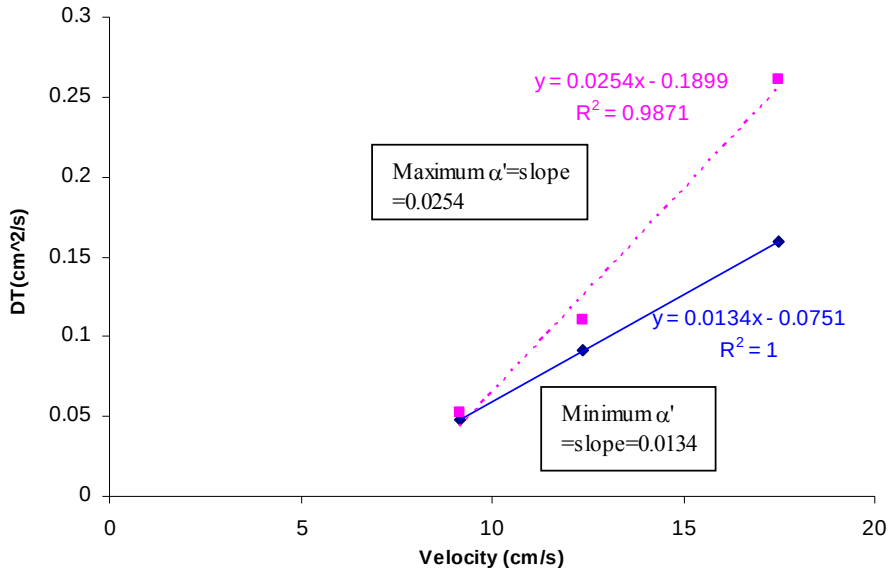

Figure 7.6 Error analysis of DT and α' for 0.5 mm glass beads (2.5 cp oil)

Table 7.2 D_T values for different velocities in 0.5 mm glass beads experiment with 2.5 cp oil

	Water Velocity	Oil Velocity	20%	50%	80%	Relative error
	(cm/s)		D_T (cm^2/s)	D_T (cm^2/s)	D_T (cm^2/s)	($\Delta D_T/D_T$ mean)
	13.11	5.24	0.0329	0.0302	0.0307	
	13.11	5.24	0.0336	0.0366	0.0393	
	13.11	5.24	0.0504	0.0497	0.0409	
	13.11	5.24	0.0672	0.0537	0.0786	
	13.11	5.24	0.0681	0.0672	0.0710	
Average	9.17		0.0505	0.0475	0.0521	9.19%
	17.68	7.07	0.0954	0.1096	0.1060	
	17.68	7.07	0.0746	0.1288	0.1399	
	17.68	7.07	0.0974	0.0644	0.1082	
	17.68	7.07	0.0954	0.0671	0.0931	
	17.68	7.07	0.1010	0.0851	0.1073	
Average	12.37		0.0928	0.0910	0.1109	20.3%
	24.99	10.00	0.2983	0.1573	0.2300	
	24.99	10.00	0.2652	0.1398	0.1150	
	24.99	10.00	0.2762	0.1457	0.1296	
	24.99	10.00	0.2241	0.1573	0.1472	
	24.99	10.00	0.2387	0.1948	0.1873	
Average	17.50		0.2605	0.1590	0.1618	52.4%

Shown in Table 7.2 are D_T error values for 0.5 mm glass beads with 2.5 cp oil.

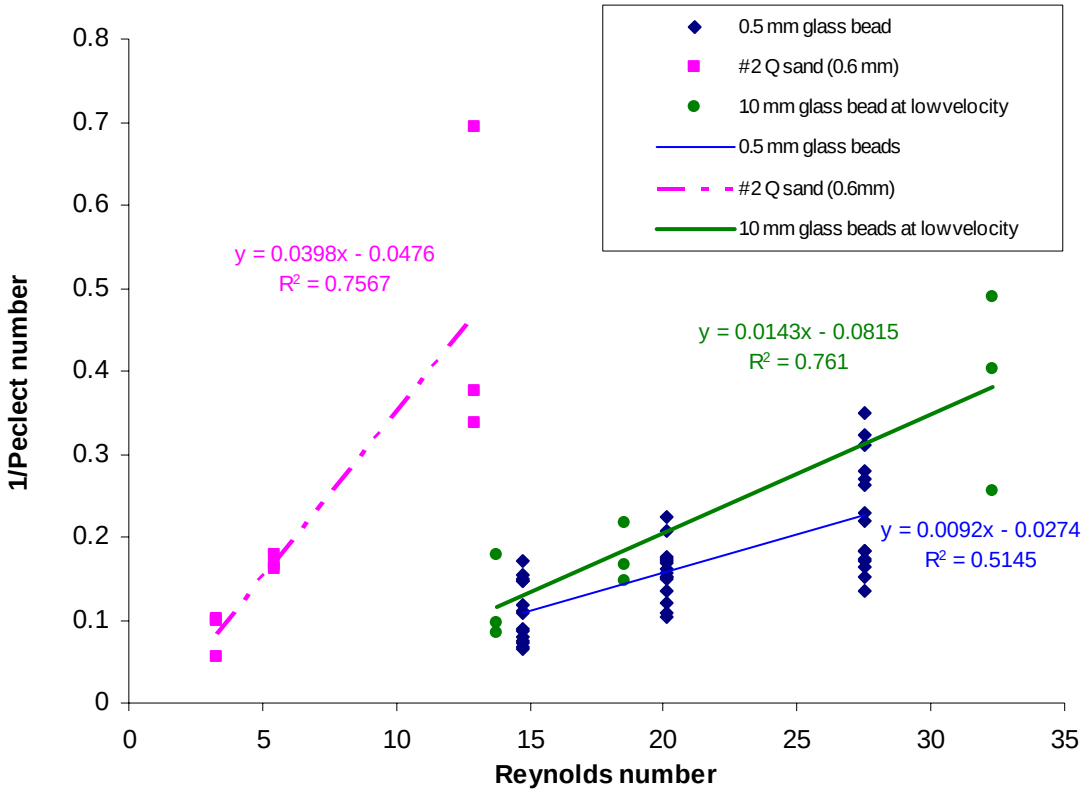

Figure 7.7 Dimensionless analysis of D_T vs. velocity

To obtain the relationship for any scale, dimensionless groups of Peclet and Reynolds numbers are used. The characteristic length is the diameter of grain. Their plots in Figure 7.7 show that sand has larger D_T than glass beads. The observation is consistent with the plots of transverse dispersion in Figure 5.13 through 5.15. Because sand is a natural material, there is greater variability in its grain size and shape. This may result in more tortuous flow at the pore scale, or variability in Darcy velocity due to larger-scale heterogeneity. Either of these phenomena would tend to increase mixing and thus D_T.

7.4 Summary

1. A series of linear-flow experiments in granular pack cell show that transverse dispersion coefficient may be a linear function of velocity.

2. Transverse mixing of water and oil at OWC appears somewhat similar to miscible dispersion in terms of linear relationship between grain size and pseudo-dispersivity in Figure 7.4. The flow experiments enable computation of transverse dispersion coefficient and the pseudo-dispersivity results.
3. Based on a group of experimental data, relative error of D_T ranges from 0.002 to 0.06 cm^2/s for water velocities from 9.2 to 17.5 cm/s, respectively.

CHAPTER 8

EFFECT OF TRANSVERSE MIXING ON OIL WELL PERFORMANCE

This chapter presents an estimation of oil well productivity reduction caused by the transverse mixing effect. Distribution of water saturation due to transverse mixing around a production well has been described by converting the linear transverse mixing model to cylindrical coordinates and integrating within radial distance. The resulting water distribution was input to a numerical simulator to compute reduction of oil rate and increase water rate and water cut. The results show that transverse mixing could increase water invasion, block the oil inflow and reduce well productivity. However, value of transverse dispersion coefficients used in the calculations come from the flow experiments (described earlier) with granular media having extremely high permeability. In actual wells permeability around actual wells is much smaller, so the transfer mixing effect may be smaller than the estimation.

8.1 Procedure of Evaluating Transverse Mixing at Wells

For a given well production rate and the experimental value of the transverse dispersion coefficients, the following procedure has been proposed to calculate an additional transverse dispersion zone assuming that the reservoir formation has similar properties as the experimental media.

1. Use commercial simulator to model a single well fully penetrating the oil and water layers.
2. Input the basic data into the simulator: well data, reservoir, and fluid properties, oil and water layer thickness, rate of production, and calculate oil and water rate and water cut.

3. Calculate radial distribution of velocity at OWC using Carman-Kozeny approach described in Chapter 4 based on (Al-Bazzaz et al, 2007).
4. Calculate distribution of the modified Richardson number to determine radial size of the transverse dispersion zone.
5. Derive a analytical model of transverse mixing in radial flow to compute water saturation distributions around the well.
6. Use water saturation distribution to determine distribution of relative permeability around the well using Corey correlations.
7. Modify near-well relative permeability in the oil well simulator's input and compute the resulting reduction oil rate and increased water rate separately for oil layer and water layer. The treatment assumes sole assessment of transverse mixing effect with no influence of crossflow.
8. Compare the oil well productivity with and without the effect of transverse mixing.

8.2 Development of Transverse Mixing Model in Radial Flow

To simulate the early transverse mixing in radial system, a radial-flow model has been developed. As discussed in Chapter 7, following Ewing (2000) and Perkins and Johnston's (1969), concentration changes are similar to saturation changes amongst immiscible fluids. In the same physical domain, when the injected phase water is immiscible with the displaced phase, the mass conservation equation can be expressed as

$$\phi \frac{\partial S_i}{\partial t} + \frac{\partial}{\partial x}(u_x S_i - \phi D_L \frac{\partial S_i}{\partial x}) + \frac{\partial}{\partial z}(u_z S_i - \phi D_T \frac{\partial S_i}{\partial z}) = 0 \text{ .....(6.3)}$$

We consider this equation for transverse dispersion.

$$\frac{\partial}{\partial z}(\phi D_T \frac{\partial S_w}{\partial z}) - \frac{\partial}{\partial x}(v S_w) = \phi \frac{\partial S_w}{\partial t} \text{ .....(6.4)}$$

Then, since v and S_w are constant values, $\frac{\partial}{\partial x}(vS_w)$ can be eliminated in Cartesian coordinates. We get Eq. (6.5).

$$\frac{\partial}{\partial z}(\phi D_T \frac{\partial S_w}{\partial z}) = \phi \frac{\partial S_w}{\partial t} \quad \text{.....(6.5)}$$

However, in radial flow velocity changes with distance, Eq. (7.4) needs to be changed to radial coordinates.

Note that the left-hand side Eq. (6.4),

Let $u_z = \phi D_T \frac{\partial S_w}{\partial z}$, $\frac{\partial}{\partial z}(\phi D_T \frac{\partial S_w}{\partial z})$ becomes $\frac{\partial}{\partial z}(u_z)$.

And let $u_x = vS_w$, $\frac{\partial}{\partial x}(vS_w)$ becomes $\frac{\partial}{\partial x}(u_x)$. Both u_x and u_z have velocity unit.

Eq. (6.4) can be written in

$$\nabla u = \frac{\partial u_z}{\partial z} - \frac{\partial u_x}{\partial x} \quad \text{.....(8.1)}$$

McQuarrie (2003) shows the transformation rule from Cartesian to cylindrical coordinates,

$$\nabla u = \frac{\partial u_x}{\partial x} + \frac{\partial u_y}{\partial y} + \frac{\partial u_z}{\partial z} \quad \text{.....(8.2)}$$

$$\nabla u = \frac{1}{r}\frac{\partial}{\partial r}(ru_r) + \frac{1}{r}\frac{\partial u_\theta}{\partial \theta} + \frac{\partial u_z}{\partial z} \quad \text{.....(8.3)}$$

When u is not dependent on θ, the $\partial u_\theta / \partial \theta$ term can be eliminated.

$$\nabla u = \frac{1}{r}\frac{\partial}{\partial r}(ru_r) + \frac{\partial u_z}{\partial z} \quad \text{.....(8.4)}$$

And the derivative to z does not change from Cartesian to cylindrical coordinates, so, $\frac{\partial}{\partial z}(\phi D_T \frac{\partial S_w}{\partial z})$ will be carried on into cylindrical coordinates without change. Therefore, Eq. (8.1) in cylindrical coordinates becomes

$$\frac{\partial}{\partial z}(u_z) - \frac{1}{r}\frac{\partial}{\partial r}(ru_r) = \phi\frac{\partial S_w}{\partial t} \quad \text{.....(8.5)}$$

Where, $u_r = vS_w$

Substitute the expressions for u_r and u_z defined here, Eq. (8.5) becomes

$$\frac{\partial}{\partial z}(\phi D_T \frac{\partial S_w}{\partial z}) - \frac{1}{r}\frac{\partial}{\partial r}(rvS_w) = \phi\frac{\partial S_w}{\partial t} \quad \text{.....(8.6)}$$

As we know, the flow rate is constant. Hence,

$$v_{r_0} * 2\pi r_0 * h = v * 2\pi r * h \quad \text{.....(8.7)}$$

So, $v = \frac{v_{r_0} r_0}{r}$ .....(8.8)

Where, r_0 = radial size of transverse mixing around well

v_{ro} = flow velocity at r_o

Considering Eq. (8.8), the term $\frac{1}{r}\frac{\partial}{\partial r}(vrS_w)$ becomes $\frac{v_{r_0} r_0}{r}\frac{\partial}{\partial r}(S_w)$.

Similar to the reasoning used in deriving Eq. (6.5), saturation change longitudinal (radial) direction is negligible, so the term $\frac{\partial}{\partial r}(S_w) = 0$. Hence, Eq.(8.6) becomes

$$D_T \frac{\partial^2 S_w}{\partial z^2} = \frac{\partial S_w}{\partial t} \quad \text{.....(8.9)}$$

Interestingly, transverse mixing in radial flow (Eq. (8.9)) is discussed by the same equation as that for linear flow, Eq. (6.5). However, in the radial model the flowing (residence) time is defined as

$$t = \frac{\pi(r_0^{\,2} - r^2)h}{Q} \quad \text{.....(8.10)}$$

Also, considering the experimental results on pseudo-dispersivity, we have

$$D_T = v\alpha' \quad \text{.....(7.1)}$$

Thus, the radial flow model for transverse mixing is

$$S_w = S_{wc} + (S_{wooi} - S_{wc})\,\mathrm{erfc}\left(\frac{z}{2\sqrt{\alpha'\frac{(r_0^{\,2} - r^2)}{2r}}}\right) \quad \text{.....(8.11)}$$

Note that, the solution in Eq. (8.11) is also the same as the linear-flow model solution – Eq. (6.35).

$$S_w = S_{wc} + (S_{wooi} - S_{wc})\,\mathrm{erfc}\left(\frac{z}{2\sqrt{D_T t}}\right) \quad \text{.....(6.35)}$$

Moreover, Considering $t = \frac{x_0 - x}{v}$ and $D_T = v\alpha'$, Eq. (6.37) and pseudo-dispersivity in Eq. (7.1) the linear flow model becomes very similar to the radial flow model in Eq. (8.11) as

$$S_w = S_{wc} + (S_{wooi} - S_{wc})\,\mathrm{erfc}\left(\frac{z}{2\sqrt{\alpha'(x_0 - x)}}\right) \quad \text{.....(6.37-1)}$$

8.3 Well Productivity Evaluation

A numerical model for single well is established in a radial system. The well fully penetrates both water and oil layer. The related properties are listed in Table 8.1. Run this model in a given pressure drawdown, oil productivity and water cut are computed. A spreadsheet model is also set up for computation of interstitial velocities at various distances away from the well. The increased pressure gradient difference as fluid approaches wellbore accelerates the flow velocity, and may cause larger transverse mixing. The interstitial velocity of onset transverse mixing (the intercepts on x axis in Figure 7.1 to 7.3) is used to determine the radial size. Oil productivity and water cut are computed, results are shown in Table 8.3.

Table 8.1 The basic input data

	Name of parameters	Glass Beads	Sand
k_{ro}	Oil Relative Permeability End Point	1	1
k_{rw}	Water Relative Permeability End Point	1	1
μ_o	Oil Viscosity (cp)	2.5	2.5
μ_w	Water Viscosity (cp)	0.6	0.6
S_{or}	Residual Oil Saturation (Fraction)	0.1	0.1
S_{wc}	Irreducible Water Saturation (Fraction)	0.1	0.1
n_o	Corey Exponent for Oil	2	2
n_w	Corey Exponent for Water	2	2
Q_o	Flow Rate (B/D)	4600	4600
Q_w	Flow Rate (B/D)	20000	20000
Δp	Total Pressure Drawdown (psi)	10	2000
k	Average Permeability (Darcy)	330	1
ϕ	Porosity (Fraction)	0.4	0.25
α'	Pseudo-Dispersivity (in)	0.005	0.001
h_o/h_w	Oil/Water Thickness (ft)	7	7

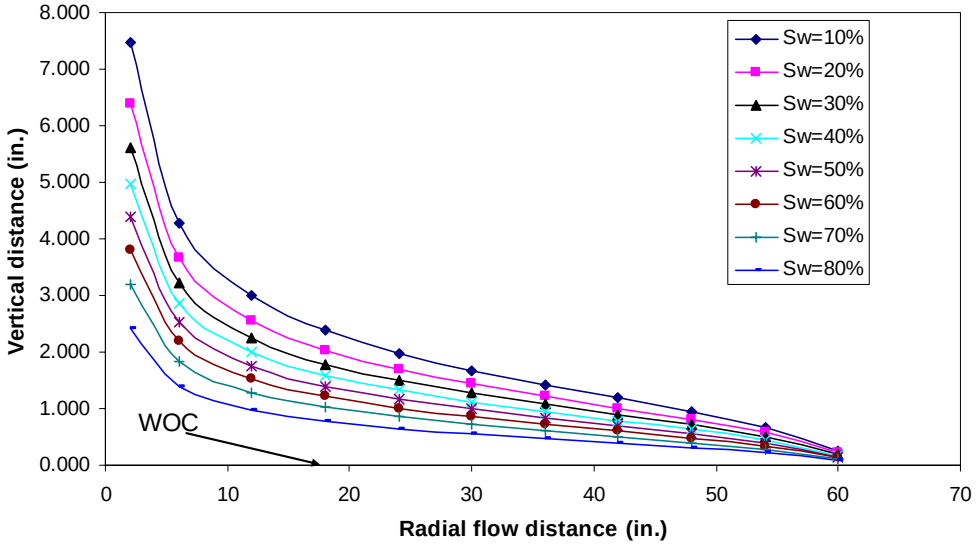

Figure 8.2 Water saturation profile in a cylindrical coordinates for data from Run # sg-1-1

In step 5 in 8.1, distribution of water saturation around the well was computed with Eq. 8.11. A cluster of water saturation isolines is shown in Figure 8.2. In step 6, relative permeability curves were generated using Corey equations with both exponents equal 2.0). And the relative permeability end points equal 1.0 as shown in Table 8.2. Then saturation distribution values (Figure 8.2) were input into the radial grid cells within the zone of transverse mixing.

Table 8.2 Relative permeability in simulations

S_w	k_{rw}	k_{ro}
0.10	1	0
0.20	0.76	0.02
0.30	0.56	0.06
0.40	0.39	0.14
0.50	0.25	0.25
0.60	0.14	0.39
0.70	0.06	0.56
0.80	0.02	0.77
0.9	0	1

Following step 7, the simulations were run separately for the oil and water layers. Two cases have been run for evaluation the effect of mixing on oil production for the condition: Δp=formation pressure – bottom hole flowing pressure=constant. The numerical codes are attached in Appendix D.

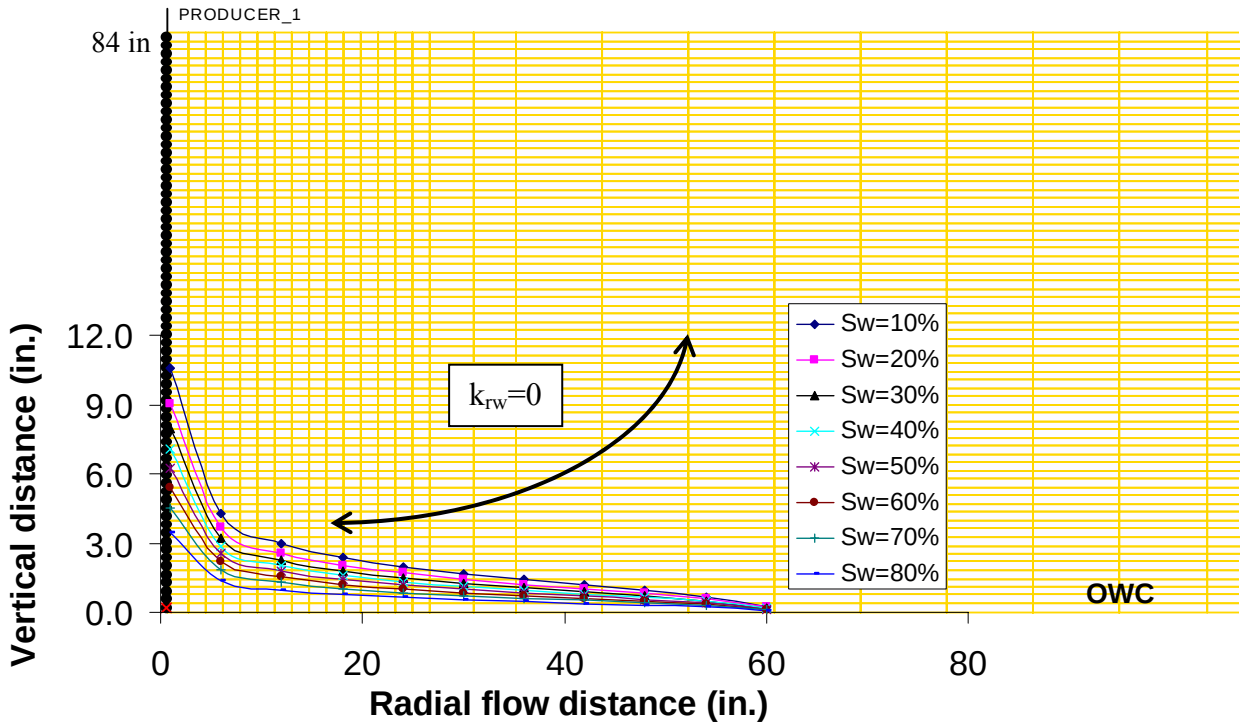

Figure 8.3 Modified water saturation in oil layer due to transverse mixing-oil layer simulation run

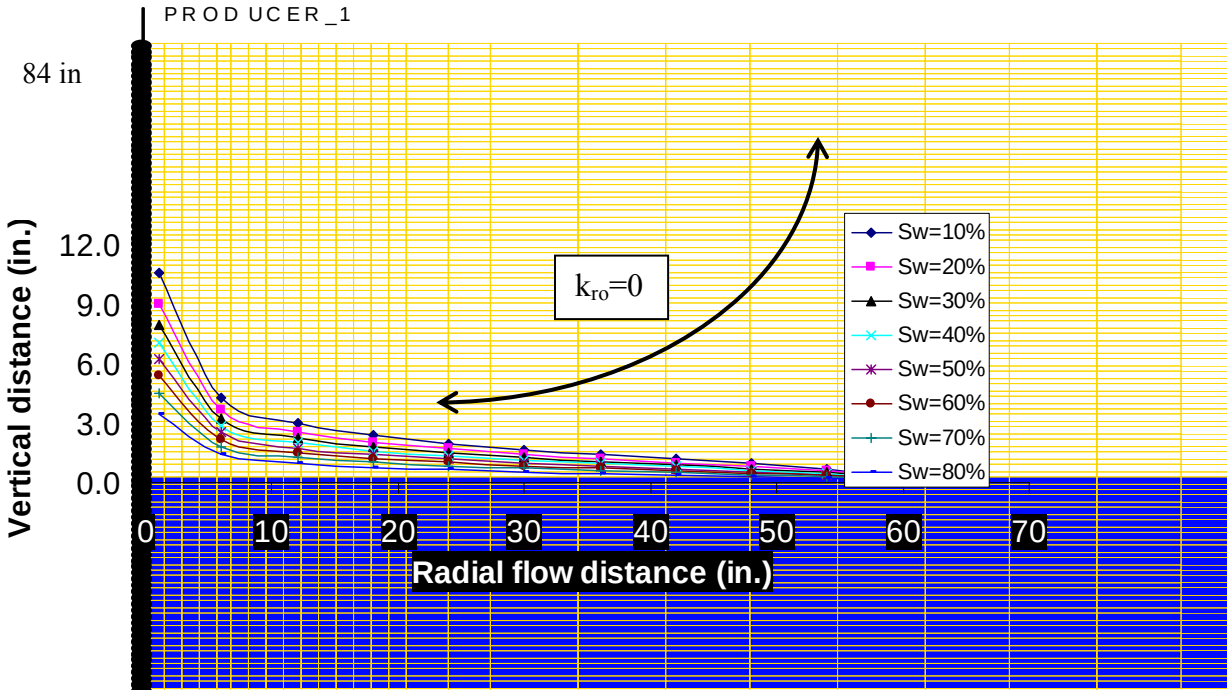

Figure 8.4 Modified water saturation above OWC in water simulation run

Without transverse mixing (step 2 in 8.1), the well's oil and water production rates were 4600 and 23000 Bbl/day, respectively with 10 psi pressure drawdown. The calculated oil productivity index was 460 Bbl/D/psi. Then, in the oil layer run (step 7), Figure 8.3 shows water saturation distribution from Figure 8.2 input into the simulation within the modified S_w distribution. Then the calculated zone relative permeabilities were changed, accordingly.

For the water layer run the modified S_w distribution zone was added above the OWC as shown in Figure 8.4, and only relative permeability of water was used in the computations. Oil relative-permeability is derived. The simulations show that transverse mixing alone reduced the oil production rate from 4600 B/D/psi to 4400 B/D/psi. Also, the well productivity index reduced from 460 to 440 B/D/psi.

In the simulation runs, a finer-grid model was used with the number of grids in the vertical direction is increased to 70. The vertical size of the grids was reduced from 5 ft to 0.1 feet. All other properties of the reservoir model are kept the same. "Convergence by Newton's

Method" is applied in the simulation. The keyword in the simulator specifies the convergence criteria for Newton's Method when the strongly non-linear conservation equations are solved. Since the saturations do not change in the single phase flow model, the saturation convergence tolerance was relaxed from 0.000001 to 0.001 to help the solution to converge.

As shown in Table 8.3, transverse mixing reduced productivity index, and increased water cut by 8.3% and 2.5%, respectively.

Table 8.3 Comparison of results

	No Transverse Mixing	Transverse Mixing	Change (%)
Oil Rate (BOD)	4600	4400	-4.35
Water Rate (BOD)	23000	23200	0.87
Productivity Index (BOD/psi)	460	440	-4.35
Water Cut (%)	83.33	84.06	0.87

Transverse mixing is also evaluated for an actual reservoir. The input parameters are the same as the Table 8.1, except permeability reduces to 1 Darcy, porosity is 25%, and pressure drawdown increases to merely 2000 psi. Referring the mixing velocity is the 0.6 mm sand, the onset mixing velocity is 1 cm/s (Figure 7.2), which is smaller than onset mixing velocity in glass beads (Figure 7.1). A newly extrapolated dispersivity of this sand is 0.001 inch using Eq. (7.2). The computed mixing size around wells is about 30 ft. Following the same procedures in 9.1, two simulation results are compared in Table 8.4.

Table 8.4 Comparison of results

	No Transverse Mixing	Transverse Mixing	Change (%)
Oil Rate (BOD)	4800	4400	-8.33
Water Rate (BOD)	20000	20500	2.50
Productivity Index (BOD/psi)	2.4	2.2	-8.33
Water Cut (%)	80.65	82.33	2.09

8.4 Discussion of Simulation Results

The following conclusions are drawn:

1. The effect of transverse mixing on oil productivity is not significant because the applied value of transverse dispersion coefficient is small because no tortuosity (heterogeneity) is considered, and early-time dispersion is used in the coefficient computation.
2. In actual rocks near wells, capillary effect may be dominated; the effect of transverse dispersion may be masked by the transition zone induced by capillary pressure.
3. Because only early-time dispersion has been observed, the results of pseudo-dispersivity affects the actual value of D_T; if the size of flow cell is bigger enough, and less/no boundary effect affect the size of mixing zone, the mixing zone could expand as it may occur in actual rocks, larger D_T may be obtained.
4. The extrapolation of α' was 0.003 inch from early-time dispersion experiments (s-1-1) in a short flowing distance (7.5 inch). To predict transverse dispersion for a much larger distance, e.g. 30 ft, the extrapolated dispersivity may not be accurate due to no experimental verifications.

CHAPTER 9

CONCLUSIONS, CRITICISMS AND RECOMMENDATIONS

9.1 Conclusions

The dissertation presents a study of transverse mixing in segregated flow of immiscible viscous fluids in porous media. The main findings of the study are summarized below.

1. Based on literature studies, major factors affecting transverse mixing may be shear mixing and momentum transfer (collision) effects. The effects have been studied experimentally with Hele-Shaw interface instability and gravel pack physical models. Transverse mixing across the interface between two fluids may occur in a concurrent segregated flow.
2. Reservoir simulation was applied to study transition zone at water-oil contact as both fluids flow at the same/different velocities in similar flow conditions. No transition zone developed in linear segregated flow of oil and water at high pressure drop in the model. The result indicated that W/O mixing phenomenon can not be modeled in simulator.
3. Transverse mixing of oil and water comprising waves and scattered globules above unstable interface has been observed in Hele-Shaw experiments. Flow velocity and two-phase velocity contrast may increase wave length. However, in view of Meignin et al's experimental results, smaller gap size reduces wave length. The equivalent permeability of Hele-Shaw (gap=0.28mm) is 6500 Darcy. Hence, for a gap size of the order of throat sizes in porous media, the shear effect would be negligible.
4. In porous medium, collision effect resulting from tortuosity is the main factor causing transverse mixing. The effects involve impingements between fluid/fluid and

fluid/rock. With collisions, fluids may transfer across their interface, and transition zone forms.

5. The ratio of size of pore and throat in porous media is critical for transverse mixing. Because the ratio contributes to tortuosity directly leading to transverse flow, and flow path change may generate inertial force inducing transverse mixing.
6. Transverse mixing must occur when inertial forces exceed the sum of capillary and gravity forces. Mixing criteria for segregated flow in porous media have been developed using modified dimensionless group of Richardson number.
7. Onset of transverse mixing in pores/throats occurs without turbulence, regarding that Reynolds number criterion for turbulence flow in porous media is 300. In a series of computations with typical formation parameters, transverse mixing condition is always met when Reynolds number is between 1 and 100.
8. Transverse mixing has been confirmed with granular-pack flow cell experiments. However, only early time mixing has been observed because of dimensional effects. The results showed no oil invading water, and only water invading oil layer with water saturation at initial W/O interface remaining constant. Higher pressure gradients and larger grain sizes increased transverse mixing. Increased oil viscosity reduced mixing. Also, results showed that the size of mixing zone was proportional to square root of time, thus following the dispersion principle. Hence, transverse mixing should be mathematically described with a dispersion model.
9. A model of early transverse mixing has been derived by solving the linear flow equation of incompressible fluids with first order transverse dispersion term, for constant flow velocity and constant water saturation at initial W/O interface (S_{wooi}).

The model matched experimental results. Also, it has been used to determine transverse dispersion coefficient (D_T).

10. Experiments have shown that transverse dispersion coefficient was proportional to average flow velocity. A formula of pseudo-dispersivity has been proposed. The scaling of pseudo-dispersivity indicates an analogy of transverse mixing with miscible dispersion in terms of linear relationship between grain size and pseudo-dispersivity.
11. Water saturation due to transverse mixing around a producing well has been described by transferring transverse mixing model to cylindrical coordinates and integrating within radial distance. Then, the water saturation was input to a reservoir simulator by modifying relevant simulation grids. In the case study, aimed at assessing transverse mixing effect for a known value of D_T, water production increased by 2.5%; oil decreases by 8.3%; and there was an overall 2.1% of water cut increase from 80.6% to 82.3%. Hence, transverse mixing may significantly increase water production, and therefore, reduce a well's oil productivity.

9.2 Critical Comments

This study is merely the first attempt to understand the phenomenon that has not been well studied. Therefore, limitations and shortcomings of this research should be pointed out as follows.

1. Size of the gap between two plates in Hele-Shaw model controls the capillary effect on interface stability. The current gap is 0.28 mm, which gives low capillary pressure and extremely high permeability (about 6000 Darcy). However, actual formation rock permeability ranges require much smaller gap size and vertical space. A correlation

of gap size with wavelength and amplitude could be quite insightful for excluding the shear mixing effect entirely.

2. Simplifications and assumptions in the mathematical model of transverse mixing weaken applications of the model. In describing dispersion process, longitudinal dispersion has not been included, which may oversimplify the mechanisms of long-time mixing. Also, for this model, constant velocity at original interface has been assumed. However, if light oil invades into water flow, velocity at the original interface may be a function of water saturation. Thus, velocity may change with the flow distance.
3. The pore-scale analytical demonstration can illustrate bifurcated two-phase flow in different types of displacement, such as piston-like and snap-off. It ignores effect of capillary and gravity. So, the derivations cannot be used for network models without improvement.
4. The dimensions of the current model limit the observation of stabilization of the transition zone. Since the outlets of the model is only 15 inches from the inlets, transverse mixing does not have enough time to reach equilibrium condition before the end effects begin. So, the captured saturation profile represents only developing early time mixing. The restricted outflow that generates flow convergence, which reverses water saturation profile because there are only two outlets that concentrate flow streams at the center of model's end.
5. Fluids selection may affect the conclusions. In the experiments, oil viscosity was always higher than water viscosity. This fact combined with the small size of the flow cell might have resulted in constant value of water saturation at original W/O interface (S_{wooi}).

6. There is a need for more experimental support of the thesis that transverse mixing is indeed a dispersion process. At this point, there is only an observation of a good mathematical correlation of $S_w(z)$ distribution with time over a very short flow distance.
7. Integration of the transverse mixing model with well inflow simulator has been made for the purpose of having some estimation of the effect. Firstly, a constant level of OWC was set over much longer distance than that in the experiments. Secondly, the transition zone from the radial transverse mixing model was input into the simulation grids separately for water and oil well.

9.3 Recommended Future Work

Future works is needed to better describe the process of transverse mixing. Particularly, emphasis should be given to:

1. Make the gap between two plates of the Hele-Shaw adjustable. The size could be reduced to about 10 microns. For different sizes of the gap, the wavelength should be measured at the same pressure gradient. Extrapolating the relationship between gap and wavelength should provide better estimate of shear effect in actual fractured porous media.
2. Design a larger size granular-pack model is critical. The current no-flow interval between two outlets should be very small or eliminated. So, ideally, the outlets should be fully evenly distributed at the model's end. This would allow fluids to keep their flow path, thus eliminate the convergence effect. Also, constant pressure at the top and bottom side of the cell could better simulate actual flow in the formation.

3. Use different less viscous fluids. So, the case of light oil having less viscosity than water could be considered. To see a complete spectrum of transverse mixing, very light oil invasion to water should be investigated.
4. A 2-D dispersion model might be needed to describe late-time mixing equilibrium. The numerical methods like Matlab may be a powerful tool to find solutions. Also, continuous mixing (grain-by-grain) in a network model should be used to reach better understanding of mixing mechanisms.
5. Due to lack of field data, the productivity index was only tested with experimentally measured dispersion coefficients. Actual field production data are expected to apply to the model using the designed procedure, and verify the accuracy of the effect of transverse dispersion on well productivity.
6. Transverse mixing could be added to reservoir simulators used for modeling wells inflow.

REFERENCES

Al-Bazzaz, W. H. and Al-Mehanna, Y. W.: Porosity, Permeability and MHR Calculations Using SEM and Thin-section Imagines for Characterizing Complex Mauddud-Burgan Carbonate Reservoir. Paper SPE 110730 presented at SPE Asia Pacific Oil & Gas Conference and Exhibition, Jakarta, Indonesia, 30 October. 2007

Al-Rumhy, M. H. and Kalam, M. Z.: Relationship of Core-Scale Heterogeneity with Non-Darcy Flow Coefficients, SPE 25649, Published in SPE Formation Evaluation, June 1996

Amyx, J. W., Bass, D. M. and Whiting, R. L.: Petroleum Reservoir Engineering. New York, McGraw-Hill, p.607, 1960

Arriola, A, Willhite, G. P. and Green, D. W.: Mobilization of an Oil Drop Trapped in a Noncircular Pore Throat Upon Contact with Surfactants. SPE 9405, prepared for 55th SPE Annual Technical Conference and Exhibition, Dallas, Texas, 21-24 September, 1980

Arya, Atul, Hewett, Tom A., Larson, R. G. and Lake, L.: Dispersion and Reservoir Heterogeneity. SPE 14364, SPE Reservoir Engineering, Feb 1988

Baldock, G. R. and Bridgeman, T.: The Mathematical Theory of Wave Motion, published by John Wiley & Sons, 1981

Batchelor, G.K.: An Introduction to Fluid Dynamics. Cambridge University Press, 1967

Bau, Haim H.: Kelvin-Helmholtz instability for parallel flow in porous media: A linear theory, Published by American Institute of Physics in Physics of Fluids, 25 (10) October 1982

Bear, Jacob: Dynamics of Fluids in Porous Media, published by Dover Publications, Inc. 1972

Belhaj, H. A., Agha, K. R., Nouri, A. M., Vaziri, H. H. and Islam, M. R.: Numerical Modeling of Forchheimer's Equation to Describe Darcy and Non-Darcy Flow in Porous Media. Paper SPE 80440 presented at SPE Asia Pacific Oil and Gas Conference and Exhibition, Jakarta, Indonesia, April 15-17. 2003

Bentsen, R. G.: A New Approach to Instability Theory in Porous Media, SPE 12725, Published in SPE Journal, October 1985

Bijeljic, B. and Blunt, M. J.: A Physically Based Description of Dispersion in Porous Media. SPE 102869, SPE Annual Technical Conference and Exhibition, San Antonio, Texas, 24-27 September 2006

Bird, R. B., Stewart, W. E. and Lightfoot, E. N.: Transport Phenomena, Published by Wiley, 2001

Blackwell, R. J.: Laboratory Studies of Microscopic Dispersion Phenomena, SPE 1483, Published by SPE Journal, March 1962

Bowlin, K.R., Wheeler, S. S. and Waldo, L. A.: Field Application of In-Situ Gravity Segregation to Remediate Prior Water Coning. SPE 38296, SPE Western Regional Meeting, Long Beach, California, June 25-27, 1997

Bush, W. M.: Surface Tension Module, Teaching material for the Department of Fluids Dynamics in MIT

Carman, P. C.: Fluid Flow through a Granular Bed. Trans. Inst. Chem. Eng. London 15, 150-156, 1937

Choudhury, S. Roy and Brown, Kevin G.: Novel dynamics in the nonlinear evolution of the Kelvin-Helmholtz instability of supersonic anisotropic tangential velocity discontinuous, Elsevier, Mathematics and Computers in Simulation 55 (2001) 377-391

Cinar, Y., Jessen, K., Berenblyum, R., Juanes, R. and Orr Jr., F. M.: An Experimental and Numerical Investigation of Crossflow Effects in Two-Phase Displacements, SPE Journal, June 2006

CMG GEM Manual, 2006

Coats, K. H. and Smith, B. D.: Dead-End Pore Volume and Dispersion in Porous Media, SPE 00647, published by SPE Journal, March 1964

Cooke, C. E., Jr. 1973: Conductivity of Fracture Proppants in Multiple Layers. JPT, 1101-1107, SPE-4117-PA

Dake, L. P.: Fundamentals of Reservoir Engineering, published by ELSEVIER Science B. V. 2002

Dixit, A. B., McDougall and Sorbie, K. S.: A Pore-Level Investigation of Relative Permeability Hysteresis in Water-Wet Systems. SPE 37233, SPE Journal, June, 1998

Duan, S. and Wojtanowicz, A. K.: Theoretical and Experimental Investigation of Water in Oil Transverse Dispersion in Porous Media. SPE 115518, SPE Annual Technical Conference and Exhibition, Denver, Colorado, September 20–24, 2008

Duan, S. and Wojtanowicz, A. K.: Bottom Water Invasion at Oil Wells due to Transverse Dispersion: Theoretical Modeling and Experimental Results. SPE 102323, SPE Annual Technical Conference and Exhibition, San Antonio, Texas, September 24–27, 2006

Duan, S. and Wojtanowicz, A. K.: Laboratory Investigation of Immiscible Transverse Dispersion Using Hele-Shaw Experiment. CIPC 2007-187, 58th Annual Technical Meeting, Calgary, Alberta, Canada, June 12 – 14, 2007

Duan, S. and Wojtanowicz, A.: Dynamic Growth of Water Saturation around Oil Wells by Water Coning and Transverse Dispersion, CIPC 2006-192, 57th Annual Technical Meeting, Calgary, Alberta, Canada, June 13 – 15, 2006

Dullien, F.A. L.: Porous Media – Fluid Transport and Pore Structure, Academic Press, New York, 1979

Evans, R. D., Hudson, C. S., and Greenlee, J. E. 1987: The Effect of an Immobile Liquid Saturation on the Non-Darcy Flow Coefficient in Porous Media. SPE Production Engineering, SPE-14206-PA

Ewing, Richard E.: Recent Development in Reservoir Simulation, 2000

Falls, A. H., Hirasaki, G. J., Patzek, T. W., Gauglize, D.A., Miller, D. D. and Ratulowski: Development of a Mechanistic Foam Simulator: The Population Balance and Generation by Snap-Off. Published in SPE Reservoir Engineering, August 1988

Ferrer, F. , Vielma, M. and Lezama, A.: Permeability Model Calibration and Pore Throat Radius Determination Using Core Analysis and Nuclear Magnetic Resonance Data in Mixed-Lithology Reservoirs, Southwestern Venezuela, SPE 108078, prepared for SPE Latin American and Caribbean Petroleum Engineering Conference, Buenos Aires, Argentina, 15-18 April 2007

Forchheimer, P.: Wasserbewewegung durch Boden. ZVDI (1901) 45, 1781

Garmeh, G., Johns, R. T. and Lake, L.W.: Pore-Scale Simulation of Dispersion in Porous Media. SPE 110228, SPE Annual Technical Conference and Exhibition, California, November 11-14, 2007

Geertsma, J.: Estimating the Coefficient of Inertial Resistance in Fluid Flow through Porous Media. SPE Journal, SPE -4706- PA. 1974

Gomez, Gilberto C. and Ostriker, Eve C.: The Effect of the Coriolis Force on Kelvin-Helmhotlz-Driven Mixing in Protoplanetary Disks, Published in The Astrophysical Journal, 630:1096.1106, September 10, 2005

Gondret, P., Rakotomalala, N., Rabaud, M., Salin, D. and Watzky, P.: Viscous Parallel Flows in Finite Aspect Ratio Hele-Shaw Cell: Analytical and Numerical Results, Published in Phys. Fluids 9(6), June (1997)

Gondret, P. and Rabaud, M. : Shear instability of two-fluid parallel flow in Hele-Shaw cell, Published in Physics of Fluids 9 (11), November 1997, by American Institute of Physics

Graham, James R.: Course's Notes: Linear Theory of Wave and Instability, UC Berkeley

Greenkorn, R. A, Haring, R. E., Jahns, Hans O. and Shallenberger, L. K.: Flow in Heterogeneous Hele-Shaw Models. SPE 999, SPE Journal December 1964

Guo, S. and Chen, Y.: Overview of Flow in Porous Media at Microscopic Scale, Xi'An, China, 2007

Haro, Carlos F.: Permeability Modeling in Porous Media: Setting Archie and Carman-Kozeny Right", SPE 100201, prepared for presentation of 2007 International Oil Conference and Exhibition held in Veracruz, Mexico, 27-30 June 2007

Hassinger, Robert C. and Rosenberg, Dale U.: A Mathematical and Experimental Examination of Transverse Dispersion Coefficients, SPE 1846, published by SPE Journal June, 1968

Hele-Shaw, H. S. : Investigation of the Nature of Surface Resistance of Water and of Streamline Motion Under Certain Experimental Conditions, Trans. Inst. Nav. Arch. (1898) Vol. XI, 25

Hernandez, Juan Carlos: Oil Bypassing by Water Invasion to Wells: Mechanisms and Remediation, Dissertation of Louisiana State University, 2007

Hertz, C. H. and Hermanrud, B.: A liquid compound jet, Journal of Fluid Mechanics Digital Archive (1983)

Hinch, E. J. and Plouraboue, F.: Kelvin-Helmholtz instability in a Hele-Shaw cell: Large effect from the small region near the meniscus, Physics of Fluids 17, 052107 (2005)

Honarpour, M., Koederitz, L. and Harvey, A. H.: Relative Permeability of Petroleum Reservoirs, CRC Press, Inc., 1986

Idelechik, E.: Handbook of Hydraulic Resistance, Second edition, published by Hemisphere. Page 333, Chapter 7, "Merging of Flow Streams and Division into Flow Streams" Publishing Corporation in 1994

Israelachvili, J.: Intermolecular and Surface Forces, 2nd Edition. Academic Press. 1995

Jaimala and Agrawal, S. C.: Shear Flow Instability in a Porous Medium. Published in Indian J. pure appl. Math., 22(7): 661-625, July 1991

Janssen, P. H., van den Broek, W.M.G.T. and Harris, C. K.: Laboratory Study Investigating Emulsion Formation in the Near-Wellbore Region of a High Water-Cut Oil Well. SPE 69740, SPE Journal, March 2001

Jaszczur, M., Szmyd, J. and Petermann, M.: An Analysis of Mixing Progress in a Static Mixer. Proceedings of the 21st International Congress of Theoretical and Applied Mechanics, Springer Verlag 2005

Jha, R. K., Bryant, S. L., Lake, L. W. and John, A.: Investigation of Pore-Scale (Local) Mixing. SPE 99782, SPE/DOE Symposium on Improved Oil Recovery, Tulsa, Oklahoma, April 22-26, 2006

Ju, B., Dai, S., Fan T., Wang, X. and Wu, H.: An Effective Method to Improve Recovery of Heavy Oil Reservoir with Bottom Water Drive. SPE 10521, International Petroleum Technology Conference, Doha, Qatar, November 21-23, 2005

Kamaya, Hideyuki: Accretion Disk Blobs, The Astrophysical Journal, 510:862-866, January 10, 1999

Kakar, Abdul Malik, Zheng, Shiyi and Stewart, George, "Well Test Analysis of Hydralically Fractured Gas Wells for Non-Darcy Flow Effects", Annual Technical Conference, Oct. 8-9, 2004

Katz, M.L. and Tek, M. R.: A Theoretical Study of Pressure Distribution and Fluid Flux in Bounded Stratified Porous Systems with Crossflow, SPEJ 146, 1961

Kumar, V. and Lake, L. W.: Scaling with Transverse Dispersion to Reduce Simulation Time. SPE 27052, the III Latin American/Caribbean Petroleum Engineering Conference, Buenos Aires, Argentina, Apr. 27-29, 1994

Kuo, M.C.T. and DesBrisay, C. L.: A Simplified Method for Water Coning Predictions. SPE 12067, SPE Annual Fall Technical Conference and Exhibition, San Francisco, California, October 5-8, 1983

Kundu, Pijush K.: Fluid Mechanics, Published by Academic Press, 1990

Lake, L. W.: Enhanced Oil Recovery, Prentice Hall. 1996

Lake, L. W. and Hirasaki, G. J.: Taylor's Dispersion in Stratified Porous Media. SPE 8436, SPE Journal, August, 1981

Li, D. and Engler, T. W.: Literature Review on Corrections of the Non-Darcy Coefficient, SPE 70015, SPE Permian Basin Oil and Gas Recovery Conference, Midland, Texas, May 15-16, 2001

Li, D. and Lake, L.: Scaling Fluid Flow through Heterogeneous Permeable Media, SPE 26648, SPE Advanced Technology Series, Vol. 3, No.1, 1995

Loginov, Arthur and Shaw, Christopher: Completion Design for Downhole Water and Oil Separation and Invert Coning. SPE 38829, SPE Annual Technical Conference and Exhibition, San Antonio, Texas, October 5-8, 1997

Ma, Huiping and Ruth, Douglas: Physical Explanations of Non-Darcy Effects for Fluid Flow in Porous Media", SPE 26150, Published in SPE Formation Evaluation, March 1997

Masalmeh, Shehadeh K.: High Oil Recoveries from Transition Zones. SPE 87291, SPE Abu Dhabi International Petroleum Exhibition and Conference, Abu Dhabi, United Arab Emirates, October 13-15, 2000

McQuarrie, Donald A.: Mathematical Methods for Scientists and Engineers. Published by University Science Books, 2003

Meignin, L., Ern, P., Gondret, P. and Rabaud, M.: “Gap Size Effects for the Kelvin-Helmholtz Instability in a Hele-Shaw Cell”, Phys. Review E, Volume 64, 026308 (2000)

Moatimid, Galal M. and El-Dib, Yusry O.: Nonlinear Kelvin-Helmholtz instability of Oldroydian viscoelastic fluid in porous media, Published by Elsevier, Physics A 333 (2004) 41-64

Mogensen, K. and Stenby, E.: A Dynamic Pore-Scale Model of Imbibition, prepared for SPE/DOE Improved Oil Recovery Symposium, Tulsa, Oklahoma, 19-22, April, 1998

Niemann, E. H., Greenkorn, R. A., and Eckert, R. E.: Dispersion during Flow in Non-uniform, Heterogeneous Porous Media, SPE 3365, 1986

Noman, R. and Archer, J.S.: The Effect of Pore Structure on Non-Darcy Gas Flow in Some Low-Permeability Reservoir Rocks, prepared for SPE/DOE Low Permeability Reservoirs Symposium, Denver, Colorado, May 18-19, 1987

O., Byre and M., Sawley: Parallel Computation and Analysis of the Flow in Static Mixer, Chem. Eng. J., 70, 93-104, 1998

Panda, M. N. and Lake, L. W.: Estimation of Single-Phase Permeability from the parameters of a Particle-size Distribution, AAPG Bulletin, V. 78, No. 7, P. 1028 -1039. 1994.

Patzek, T. W.: Verification of a Complete Pore Network Simulator of Drainage and Imbibition, SPE 71310, SPE JPT, 2001

Perkins, T. K. and Johnston, O. C.: A Review of Diffusion and Dispersion in Porous Media. SPE 00480, SPE Journal, March 1963

Perkins, T. K. and Johnston, O. C.: A Study of Immiscible Fingering in Linear Models. SPE 02230, SPE Journal, March 1969

Raghavan, R. and Marsden, S.S.: Theoretical Aspects of Emulsification in Porous Media. SPE 03089, SPE Journal, June 1971

Raimondi, P. and Torcaso, M. A.: Distribution of the Oil Phase Obtained Upon Imbibition of Water, Published in SPE JPT. March 1964

Ramshaw, John D.: Simple model for mixing at accelerated fluid interfaces with shear and compression, Published in Physical Review E, Volume 61, Number 5. May 2000

Reed, R. N. and Wheatley, M. J.: Oil and Water Production in a Reservoir with Significant Capillary Transition Zone, Published in JPT SPE September, 1984

Roof, J. G.: Snap-Off of Oil Droplets in Water-Wet Pores, SPE 2504-PA, published in SPEJ, March 1970

Rowlinson, J. S. and Widom, B.: Molecular Theory of Capillary. Dover. 1982

Russell, T. F.: Dispersion Concepts in Two-Phase Flow, Notes for University of Colorado at Denver, 1997

Samara, Hilmi: Evaluation of the Slope of Oil/Water Interface and Its Change with Time, SPE 86, January, 1961

Seright, R. S., Lane, R. H. and Sydansk, R. D.: A Strategy for Attacking Excess Water Production. SPE 84966, Journal SPE Production & Facilities, Volume 18, Number 3, August 2003

Smirnov, N. N., Nikitin, V. F., Maximenko, A., Thiercelin, M. and Legros, J. C.: Instability and Mixing Flux in Frontal Displacement of Viscous Fluids from Porous Media. Physics of Fluids 17, 084102, 2005

Smith, Charles R. and Pirson, Sylvain J.: Water Coning Control in Oil Wells By Fluid Injection, SPE 613, Published in SPE Journal, Dec. 1963

Smith, R. C. and Greenkorn, R. A.: An Investigation of the Flow Regime for Hele-Shaw Flow. SPE 2140, SPE Journal June 1969

Taylor, G.: Dispersion of Soluble Matter in Solvent Flowing Slowly Through a Tube. Proc., Roy, Soc. London, 219, 186-203, 1953

Tiffin, D. L., Stein, M. H., and Wang, X.: Drawdown Guidelines for Sand Control Completions. SPE 84495, SPE Annual Technical Conference and Exhibition, Denver, Colorado, 5-8 October 2003

Wang, J., Dong, M. and Asghari: Effect of Oil Viscosity on Heavy-Oil /Water Relative Permeability Curves. SPE 99763, Prepared for presentation at SPE/DOE Symposium on Improved Oil Recovery, Tulsa, Oklahoma, 22-26, April 2006

Willhite, G. P.: Waterflooding, Society of Petroleum Engineers, Richardson, TX, 1986

Yildiz, Turhan: Assessment of Total Skin Factor in Perforated Well. SPE 82249, the SPE European Formation Damage Conference held in The Hague, The Netherlands, May 13-14, 2003

Zapata, Vito J. and Lake, Larry W.:A Theoretical Analysis of Viscous Crossflow", SPE 10111, prepared for the 56th Annual Fall Technical Conference and Exhibition of the Society of Petroleum Engineers of AIME, held in San Antonio, Texas, October, 6.7, 1981

Zeybek, M. and Yortsos, Y. C.: "Long Waves in Parallel Flow in Hele-Shaw Cells", Phys. Review Letters, Volume 67, Number 11 (1991)

Zhou, D., Fayers, F. J. and Orr Jr, F. M.: Scaling of Multiphase Flow in Simple Heterogeneous Porous Media. SPE 27833, ASME Winter Meeting, New Orleans, November 28-30, 1997

Websites:
http://fluid.stanford.edu/~fringer/movies/shear_convect/kh.gif

http://www.eesiflo.com/static-mixer-motionless.html

APPENDIX A

PHOTOGRAPHS OF FLOW EXPERIMENTS

The following color photographs document stabilized flow conditions in the granular-pack flow cell described in Chapter 6.

● 20% ● 50% ● 80% water saturation

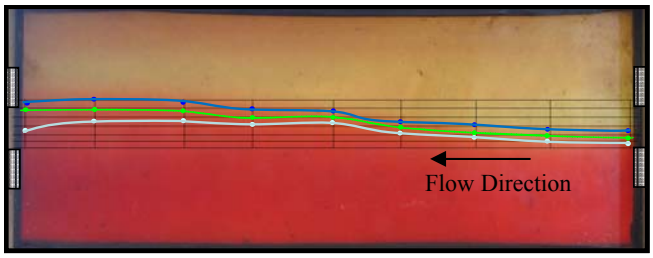

Figure A-1 Experiment in 0.5 mm glass beads -1 (Run # sg-1-1, Picture #133)

Table A-1 S_w isoline location – Run # sg-1-1

Flow distance, inch	7.5	7.5	7.5	7.5
S_w, %	20	50	80	100
Height above OWC, inch	0.42	0.3	0.17	0

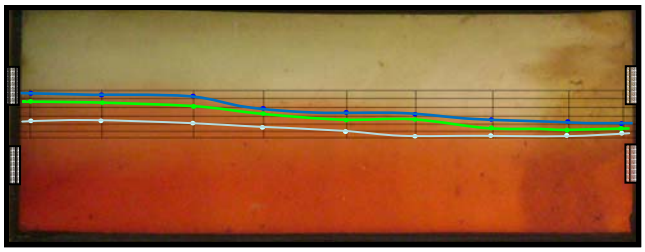

Figure A-2 Experiment in 0.5 mm glass beads -2 (Run # sg-1-2, Picture #D005)

Table A-2 S_w isoline location – Run # sg-1-2

Flow distance, inch	7.5	7.5	7.5	7.5
S_w, %	20	50	80	100
Height above OWC, inch	0.46	0.33	0.18	0

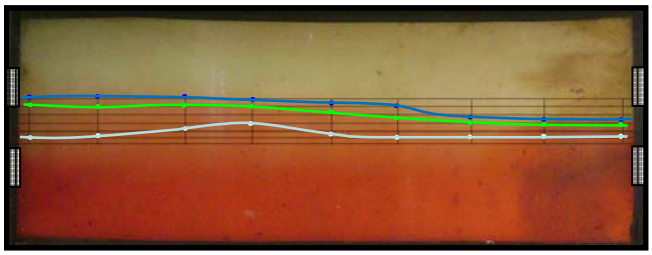

Figure A-3 Experiment in 0.5 mm glass beads -3 (Run # sg-1-3, Picture #D011)

Table A-3 S_w isoline location – Run # sg-1-3

Flow distance, inch	7.5	7.5	7.5	7.5
S_w, %	20	50	80	100
Height above OWC, inch	0.5	0.37	0.2	0

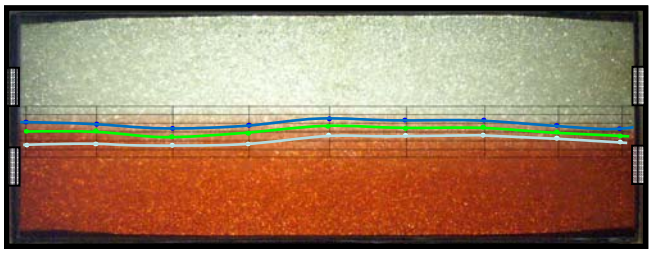

Figure A-4 Experiment in 1.0 mm glass beads -1 (Run # lg-1-1, Picture #388)

Table A-4 S_w isoline location – Run # lg-1-1

Flow distance, inch	7.5	7.5	7.5	7.5
S_w, %	20	50	80	100
Height above OWC, inch	0.4	0.25	0.2	0

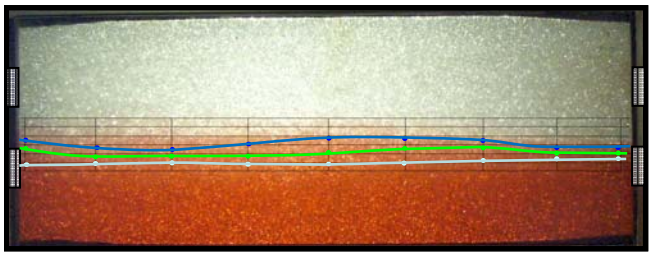

Figure A-5 Experiment in 1.0 mm glass beads -2 (Run # lg-1-2, Picture #392)

Table A-5 S_w isoline location – Run # lg-1-2

Flow distance, inch	7.5	7.5	7.5	7.5
S_w, %	20	50	80	100
Height above OWC, inch	0.45	0.35	0.2	0

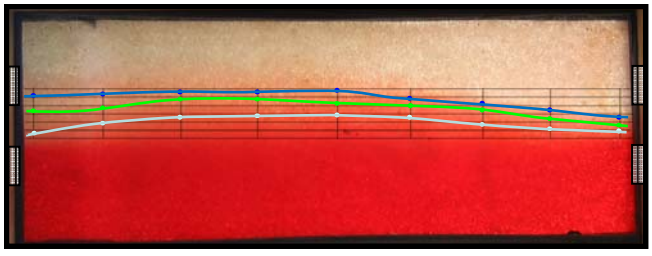

Figure A-6 Experiment in 1.0 mm glass beads -3 (Run # lg-1-3, Picture #322)

Table A-6 S_w isoline location – Run # lg-1-3

Flow distance, inch	7.5	7.5	7.5	7.5
S_w, %	20	50	80	100
Height above OWC, inch	0.7	0.6	0.3	0

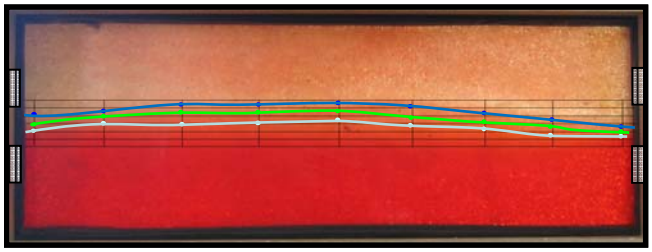

Figure A-7 Experiment in 1.0 mm glass beads -4 (Run # lg-1-4, Picture #346)

Table A-7 S_w isoline location – Run # lg-1-4

Flow distance, inch	7.5	7.5	7.5	7.5
S_w, %	20	50	80	100
Height above OWC, inch	0.6	0.5	0.25	0

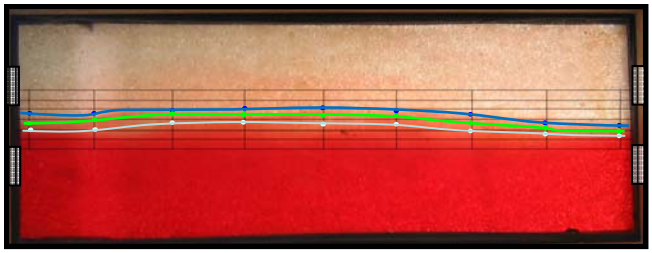

Figure A-8 Experiment in 1.0 mm glass beads -5 (Run # lg-1-5, Picture #327)

Table A-8 S_w isoline location – Run # lg-1-5

Flow distance, inch	7.5	7.5	7.5	7.5
S_w, %	20	50	80	100
Height above OWC, inch	0.4	0.3	0.2	0

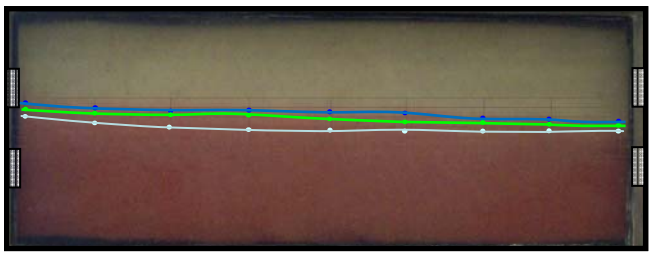

Figure A-9 Experiment in #2 Q-ROK sand -1 (Run # s-1-1, Picture #427)

Table A-9 S_w isoline location – Run # s-1-1

Flow distance, inch	7.5	7.5	7.5	7.5
S_w, %	20	50	80	100
Height above OWC, inch	0.37	0.2	0.15	0

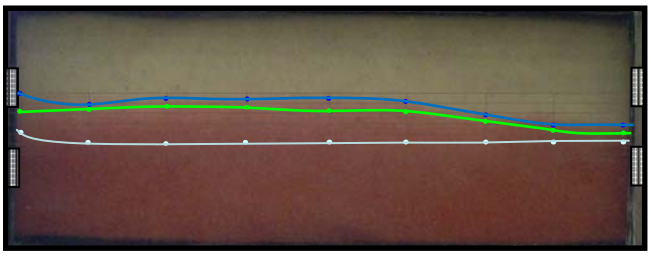

Figure A-10 Experiment in #2 Q-ROK sand -2 (Run # s-1-2, Picture #434)

Table A-10 S_w isoline location – Run # s-1-2

Flow distance, inch	7.5	7.5	7.5	7.5
S_w, %	20	50	80	100
Height above OWC, inch	0.55	0.35	0.2	0

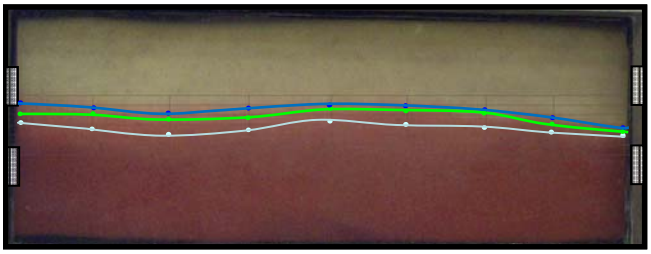

Figure A-11 Experiment in #2 Q-ROK sand -3 (Run # s-1-3, Picture #446)

Table A-11 S_w isoline location – Run # s-1-3

Flow distance, inch	7.5	7.5	7.5	7.5
S_w, %	20	50	80	100
Height above OWC, inch	0.65	0.4	0.3	0

APPENDIX B

TRANSITION ZONE AT WELLS – OTHER THAN TRANSVERSE MIXING

The purpose of this section is to understand the known mechanisms of water-oil transition zone, which do not involve any transverse mixing mechanism. This chapter presents a study of a transition zone over a flat water oil contact away from the well. The transition zone movement is considered to be a consequence of a frontal water displacement in the vertical direction in the well vicinity.

First, by using analytical methods and a numerical simulator, a transition zone in a stable water cone is proved, and then analyzed. At that point, dimensionless groups are applied to evaluate the sensitivity of properties of the formation and fluids, finding relationships using experimental design.

B.1 Water Saturation Profile before Water Breakthrough

The similarity of analytical and simulated water-oil transition zone reveals that viscous, capillary, and gravity forces are the valid driving forces in current simulators. Inertial force (or Navier-Stokes equation) is not applied.

B.1.1 Flow Model Review

In fractional flow, thickness averaged water saturation is used. The following equations are used to evaluate the water cut for any injection rate.

Equation for water saturation behind front water:

$$\bar{S}_w = S_{we} + (1 - f_{we})W_{id} \quad \text{.....(B.1)}$$

Equation for water cut in fractional flow:

$$f_{we} = \frac{1 - \frac{kk_{ro}A}{q_t\mu_o}\frac{\Delta\rho g}{1.033\times10^6}}{1 + \frac{\mu_w}{k_{rw}}\frac{k_{ro}}{\mu_o}} \quad \text{.....(B.2)}$$

For segregated flow, the following equations can be applied, only when the water oil contact has a sharp interface.

$$G = \frac{kk_{rw}A\Delta\rho g}{1.0133\times10^6 q_t\mu_w} \quad \text{.....(B.3)}$$

$$M = G\left(\frac{dy}{dx}\frac{1}{\tan\theta} + 1\right) + 1 \quad \text{.....(B.4)}$$

$$f_{we} = \frac{Mb_e - b_e(1-b_e)G}{1 + (M-1)b_e} \quad \text{.....(B.5)}$$

B.1.2 Transition Zone Profile in a Stable Cone

Table B-1 The basic input data

k_{ro}	Oil Relative Permeability End Point	0.65
k_{rw}	Water Relative Permeability End Point	0.33
μ_o	Oil Viscosity (cp)	20
μ_w	Water Viscosity (cp)	0.70
S_{or}	Residual Oil Saturation (Fraction)	0.40
S_{wirr}	Irreducible Water Saturation (Fraction)	0.45
n_o	Corey Exponent for Oil	1.8
n_w	Corey Exponent for Water	3.1
α_d	Inclined Angle (Degree)	90
ρ_o	Relative Oil Gravity	0.8
ρ_w	Relative Water Gravity	1.01
q_T	Total Flow Rate (b/d)	0.5
A	Flow Area (ft^2)	25
k	Average Permeability (md)	10
ϕ	Porosity (Fraction)	0.22
L	Thickness (ft)	35
V_b	Reservoir Bulk Volume (rb)	155.8

Assuming fluids and formation properties shown in Table B-1, I ran an analytical fractional flow model of vertical displacement with no capillary pressure. The relative permeability calculation

is based on the Corey Model. The exponent of the Corey function for water and oil are B.1 and 1.8, respectively.

The computed water saturation above the initial OWC is shown in Figure B-1. Water saturation increase slowly as it displaces oil vertically. The saturation profile is calculated from Eq. (B.1) and (B.2).

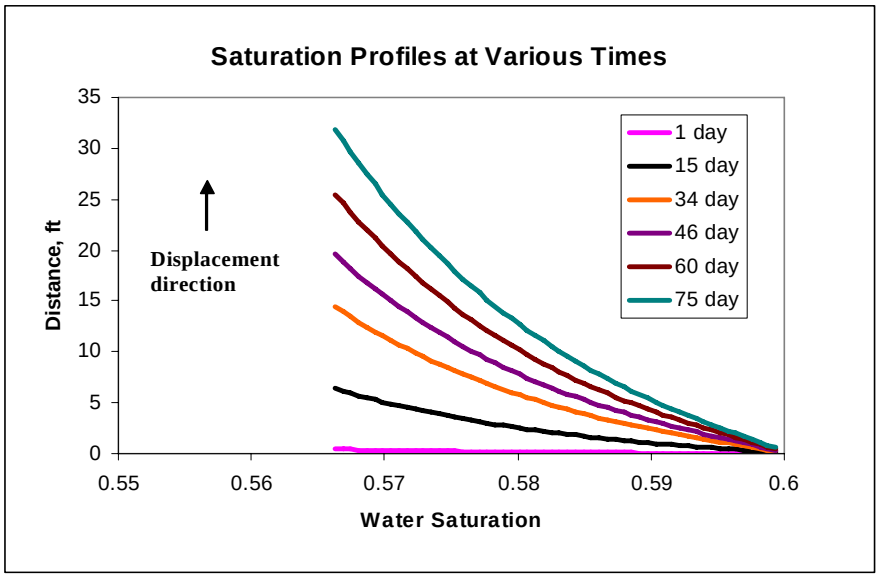

Figure B-1 Analytical computation of transition zone buildup at the water cone

The transition zone buildup at the water cone was also computed for the same formation and fluids properties, by using a radial flow numerical simulator. In this model, one producer and one injector are located in the center of the reservoir and the boundary, respectively. Radial model is used. Grids in IJK are 30, 1 and 300, respectively. k_v/k_h equals to 0.1. An appropriate ratio of production and injection rates is applied to the wells. The formation reached a dynamic stable condition, which lasts over twenty years. At this stage, we assume the producer reaches a steady state condition. Figure B-2 shows a water cone built around the well as the system reaches a steady state. The original water oil interface away from the producer is stabilized.

The shape and trend of a series of water saturation curves (Figure B-3) are found to be similar to the analytical results. The similarity of the simulated and analytical results indicates

that the process of the water cone buildup prior to water breakthrough may be considered a displacement controlled by fractional flow. Thus, we select the parameters used for sensitivity analysis as based on analytical equations.

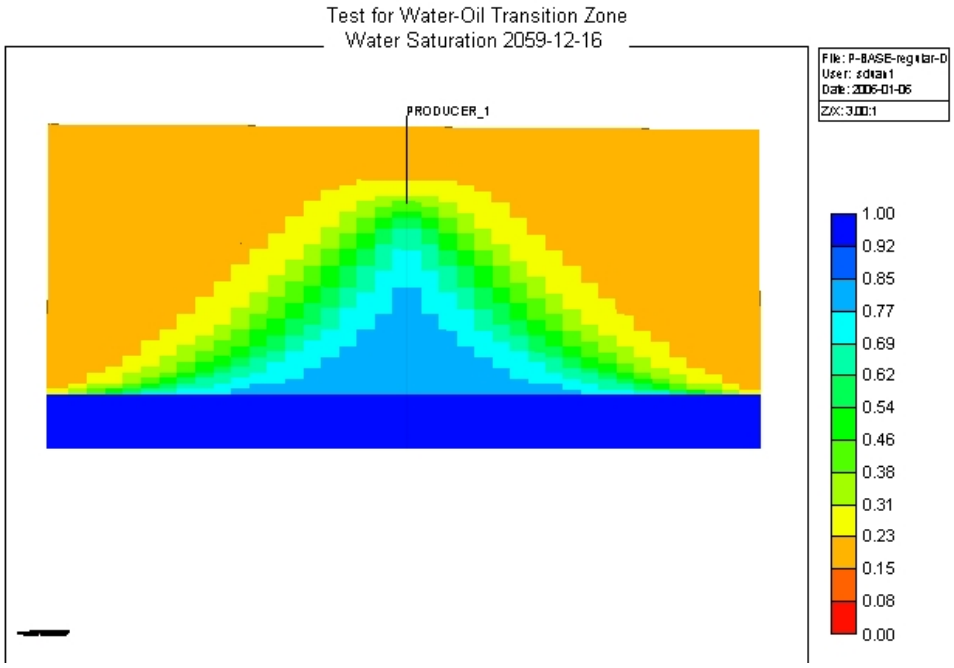

Figure B-2 Simulated buildup of transition zone at the water cone

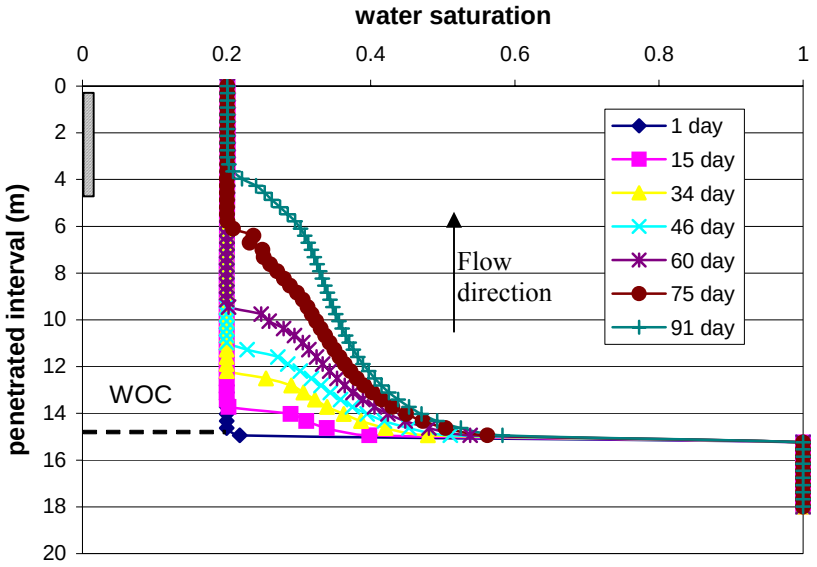

Figure B-3 Transition zone water saturation profiles at 4ft from the producer (4.5 m completion)

Prior to the water breakthrough, the water saturation profiles 20 feet away from the well in Figure B-4 indicate the same behavior of water displacement as those at 4 feet from the well,

but the plots are simply "slimmer." It means that water saturation is reduced at a position away from the producer.

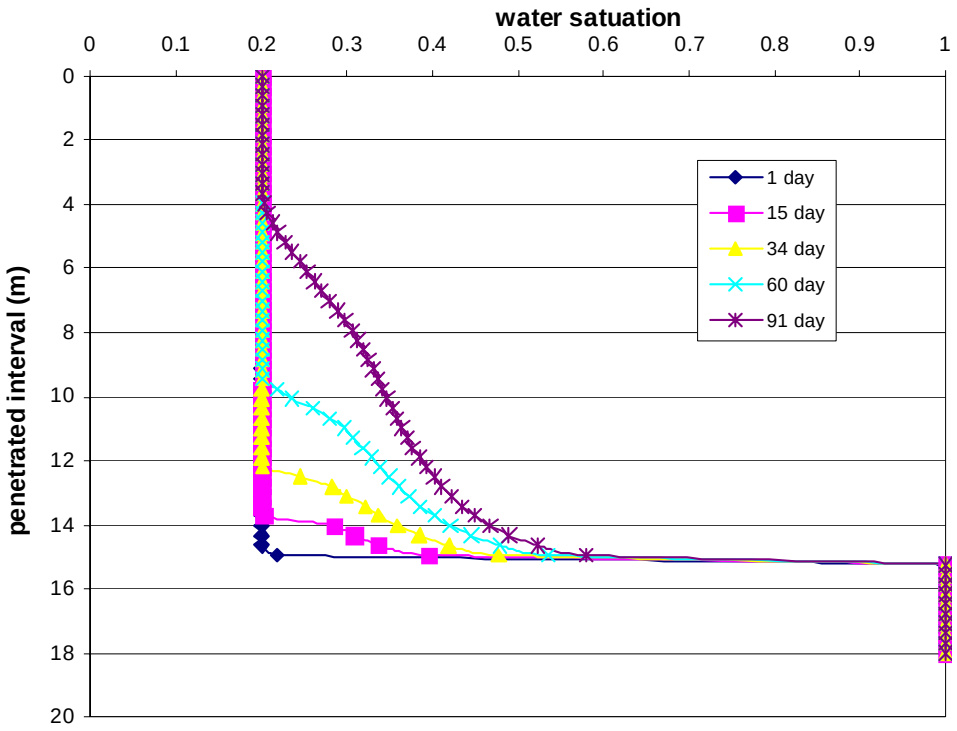

Figure B-4 Water saturation profiles at different times at 20 ft away from the producer (4.5 m completion)

B.2 Water Saturation Profile after Water Breakthrough

B.2.1 Transition Zone Profile in a Stable Cone

After the water breakthrough at the well's completion, transition zone development changes because the process is not controlled only by the mechanisms of linear displacement. As shown in Figure B-5, water saturation profiles change from exponential to parabolic with a distinct maximum value representing the top of the stabilized water cone. Since the top of the water cone resides at the bottom of the well completion, the remaining completion is open to oil inflow. In this case, the water flow path to the producer is located at only the very top of the transition zone.

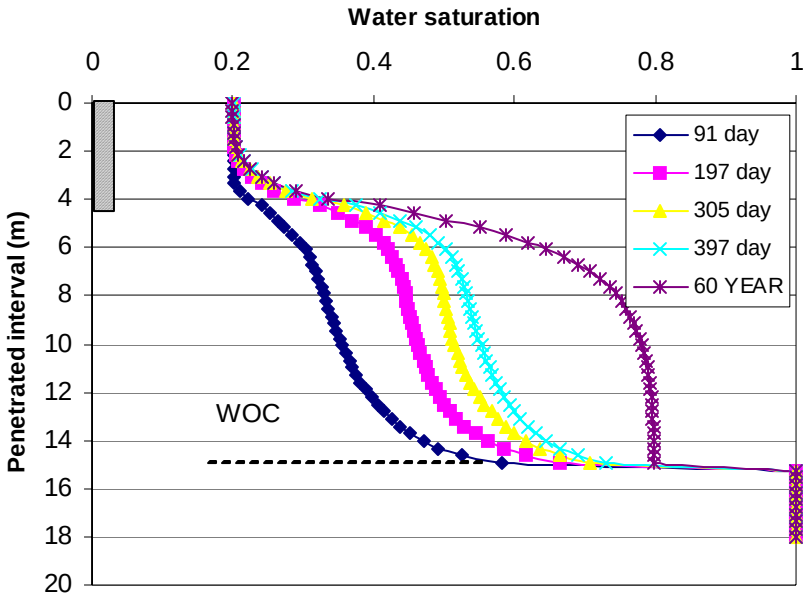

Figure B-5 Water saturation profile (r = 4ft) after water breakthrough and cone stabilization

B.2.1 Ultimate Water Cut for a Single Well

Using Eclipse, a commercially available numerical simulation tool, the numerical results of ultimate water cut show some difference from the analytical results.

To verify the concept of a stabilized water cut, we experimented with several simulations, applying radial systems having constant water supply at boundary, two different radial extents, and constant production rate of fluids, 10,000 bfpd. The reservoir and fluid properties used in the simulation were as follows:

Table B-2 The reservoir and fluid properties

k_h	Horizontal Permeability (md)	350
k_v	Vertical Permeability (md)	10
h_w	Water Zone Thickness (ft)	10
h_o	Oil Zone Thickness (ft)	50
q_T	Perforated Interval (ft)	15
μ_w	Water Viscosity (cp)	0.60
μ_o	Oil Viscosity (cp)	1.0
q_T	Total Flow Rate (b/d)	10000
t_p	Product Time (Years)	60

Two cases in a radial system are examined. Both Reservoir radiuses in case 1 and 2 are 200 ft and 500 ft, respectively.

The simulation gave slightly different results for each radii of the flow system; the water cut was 11.63% for case 1, and 11.56% for case 2. Interestingly, the ultimate water cut from the analytical model is 11.1%. The equation is used for

$$WCT_{ultimate} = \frac{\frac{k_w}{\mu_w} h_w}{\frac{k_w}{\mu_w} h_w + \frac{k_o}{\mu_o} h_o} \quad \text{.....(B.6)}$$

Apparently, there is good agreement in the numerical vs. analytical predictions for the "ultimate" water cut in the analytical model (Kuo and DesBrisay, 1983). A small discrepancy may be dependent on the relative permeability in the cone or numerical dispersion.

The discrepancy from the relative permeability may be explained. In numerical simulation, the transition zone develops and hampers water delivery to the well, since the water relative permeability within the transition zone is smaller than the end-point water permeability used in the analytical model.

B.3 Parameters Sensitivities Analysis of Water Oil Transition

The water oil transition zone around a production oil well influences oil productivity. To investigate the size of the transition zone, a series of numerical simulation runs must be executed. All the runs are populated with various combinations of dimensionless groups using experimental designs. To find the relationship between factors and the computed transition zone, a response surface methodology is used. In this study, the responding factor is the ratio of dynamic and static transition thickness, calculated after the flowing system reaches the steady state condition. Then regression patterns are used to find the transition zone interactions with different factors.

B.3.1 Description of Water Coning in a Bottom Water System

A conceptual numerical model is built for studying the process of water coning. The model features an isotropic reservoir with a partially perforated production well, located in the center of formation. Two injection wells are located at the boundary for maintenance of the formation pressure. The basic parameters are listed in Table B-2.

To obtain a steady state flow condition for the model, the ultimate water cut theory (Kuo and DesBrisay, 1983) was applied. Regarding the capillary effect, the ultimate water cut was approximately evaluated for each case. With a constant water injection pressure, small adjustments were performed on the oil injection rate. In the results, the original W/O contact, cone size, formation pressure, production, and injection rates are examined to ascertain whether the system has reached a steady state.

Table B-2 Parameters used for transition zone model

ρ_o	Oil Density (lb/ft^3)	48.7
ρ_w	Water Density (lb/ft^3)	64
μ_o	Oil Viscosity (cp)	0.5
μ_w	Water Viscosity (cp)	1.0
k_H	Horizontal Permeability (mD)	350
k_V	Vertical Permeability (mD)	30
h_o	Thickness of Oil Layer (ft)	50
h_w	Thickness of Water Layer (ft)	10
h_p	Perforated Interval (ft)	15
Q	Flow Rate (B/D)	1000

Due to capillary pressure the initial water oil transition zone is 5 feet. The static status of water oil distribution is shown in Figure B-6. After the well starts to produce, the fluid is 100% oil. At this stage, Figure B-7 demonstrates that a dynamic water cone is building up between the bottom of the perforation and W/O contact. The transition zone thickness is 11.2 ft. As production continues, the water break through time is 2 months after production. The transition zone thickness in Figure B-8 is 17.8 ft. The water oil transition zone shows the largest thickness

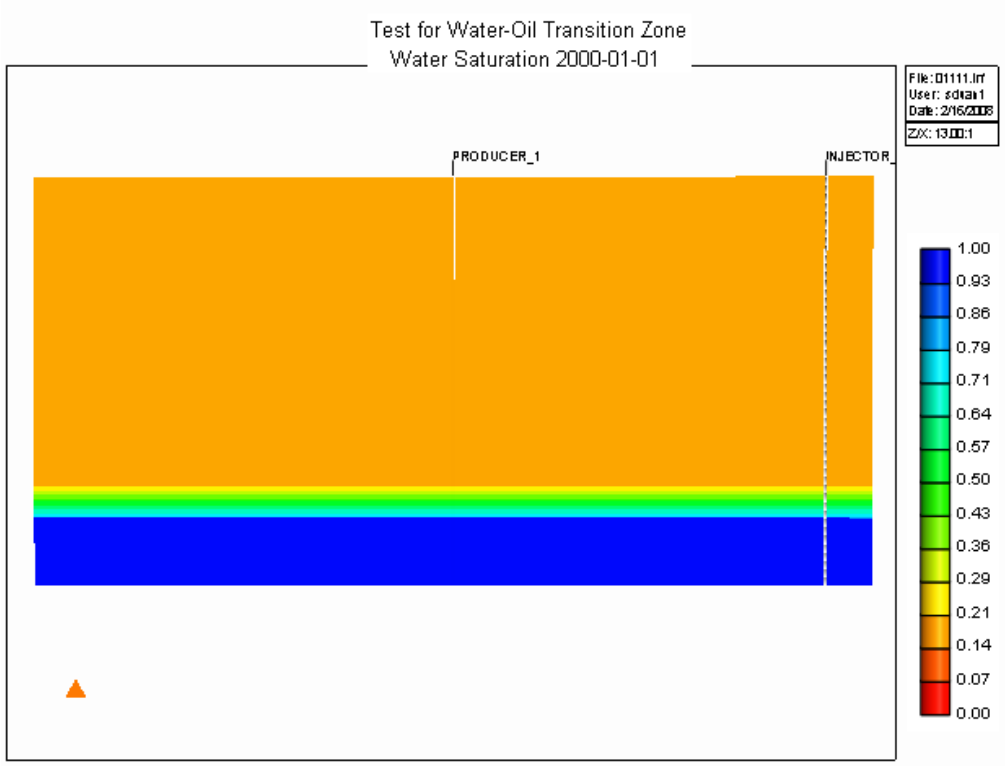

Figure B-6 Water oil contact and transition zone at initial static condition

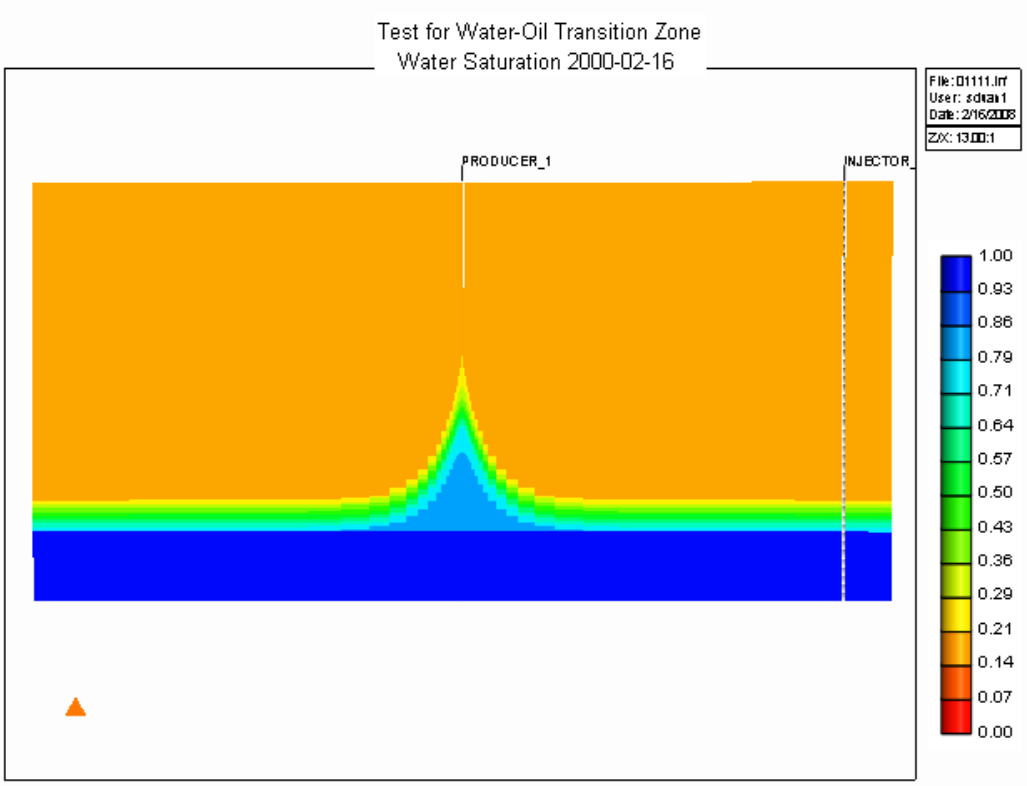

Figure B-7 Water oil transition zone during water cone building up

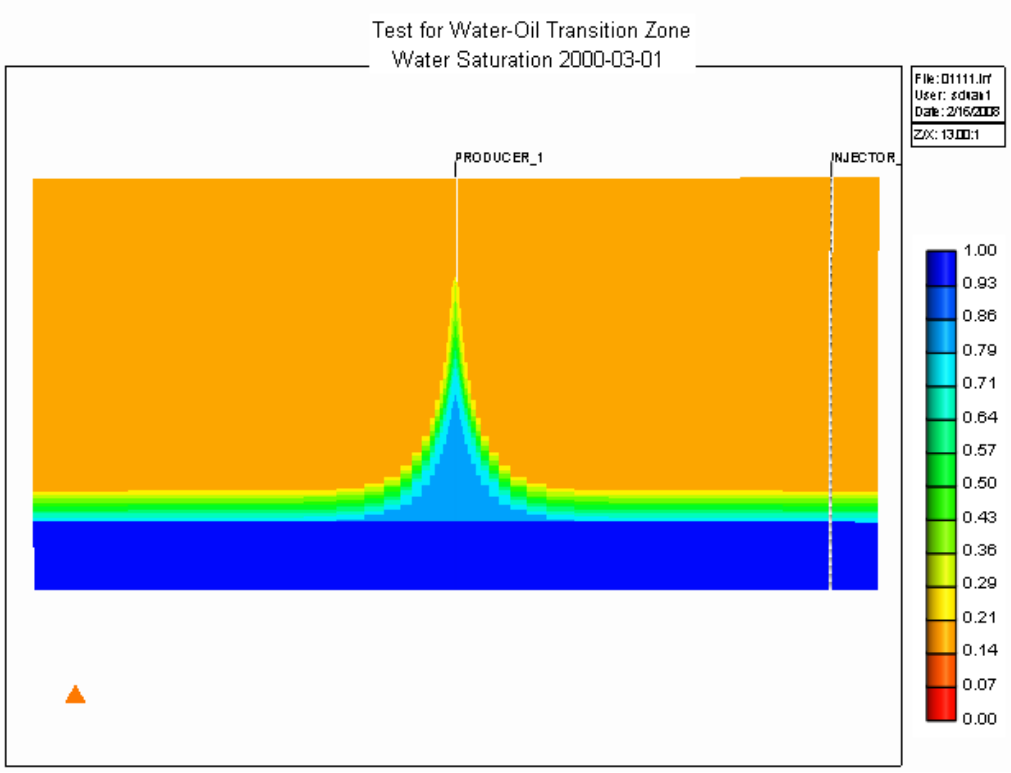

Figure B-8 Water oil transition zone during water breaking through

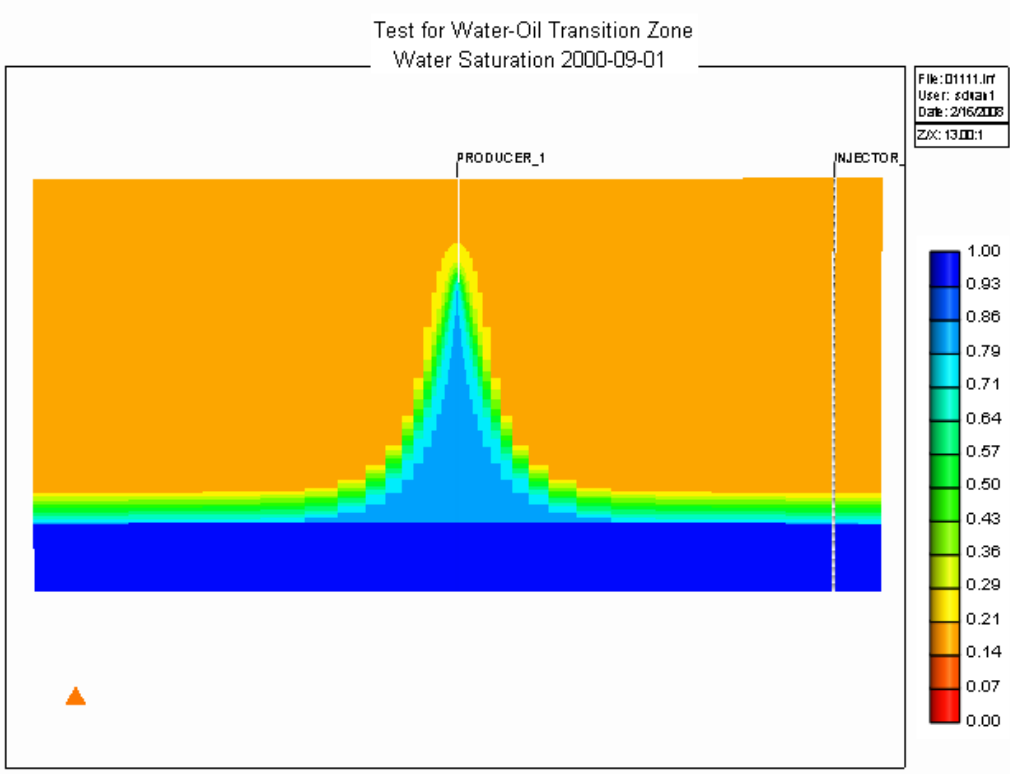

Figure B-9 Water oil transition zone as water takes over the perforated interval

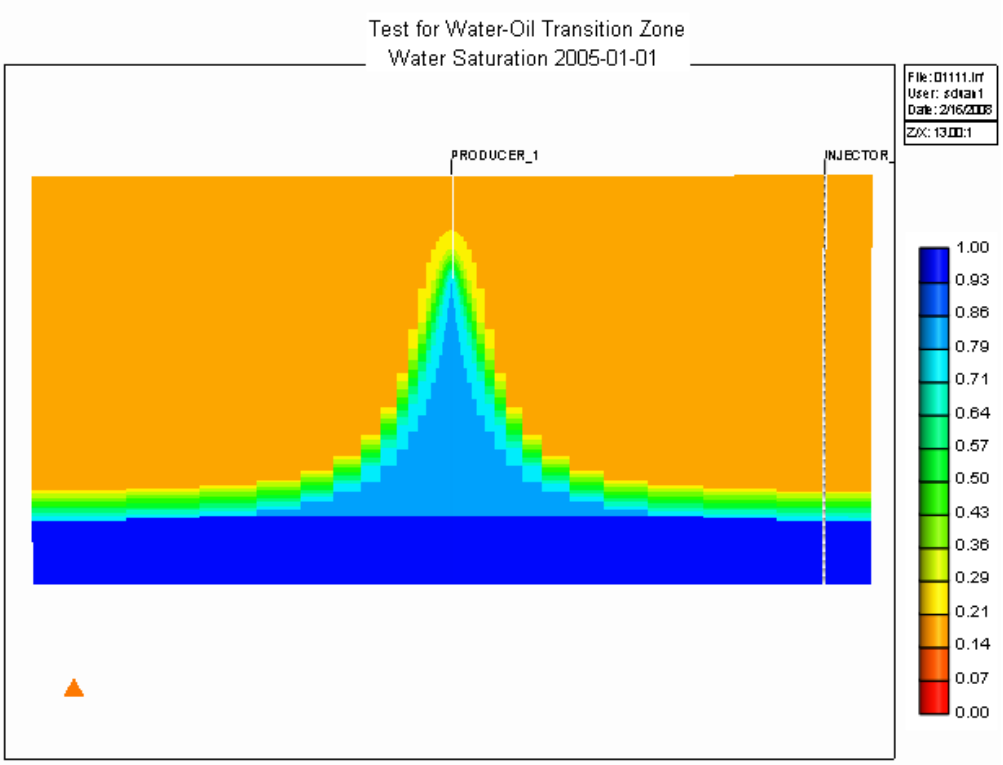

Figure B-10 Water oil transition zone in a stabilized water cone

at 26th months. At the point, the transition zone stops its upward move, but water continues to displace the residual oil in the cone, leading to transition zone thickness reduces to 8.4 ft. The water cut stabilizes at 10.5% for 15 months (Figure B-9), which indicates the system is in a steady-state condition (Figure B-10).

The mechanism of stabilization may be explained by the evolution of pressure and the saturation profile. Figure B-11 shows a near-wellbore formation pressure profiles at various production periods. The straight line shows the pressure drop at a static state. When comparing the initial pressure drop, the pressure drawdown in the interval near the well shows a large alternation at any other production time. To show the mechanism, the pressure drawdown profile is divided into two sections: at perforated interval and below the interval. The two ends' gradients are similar. But the upper pressure profile takes a longer time to reach steady state. After the pressure drawdown stops in its decreasing, the water cone shows little change for over 15 months (shown in Figure B-11). Figure B-12 shows the correspondingly stabilized water

saturation profile. Finally, it is the perforation interval after water breakthrough that controls the transition zone.

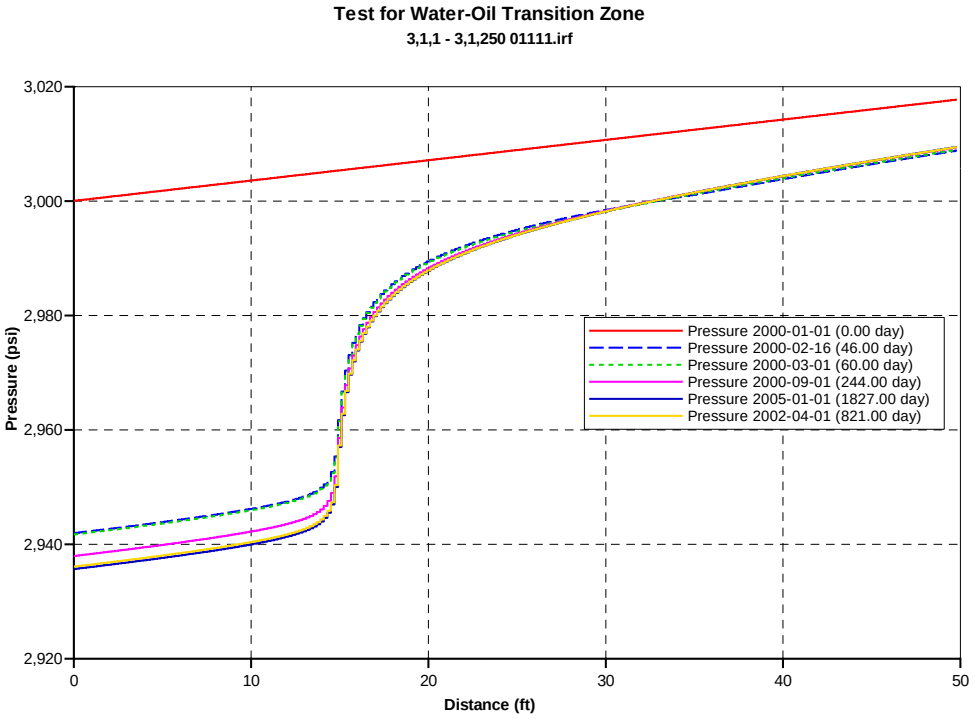

Figure B-11 Pressure profile in water cone stabilizes by 26 months

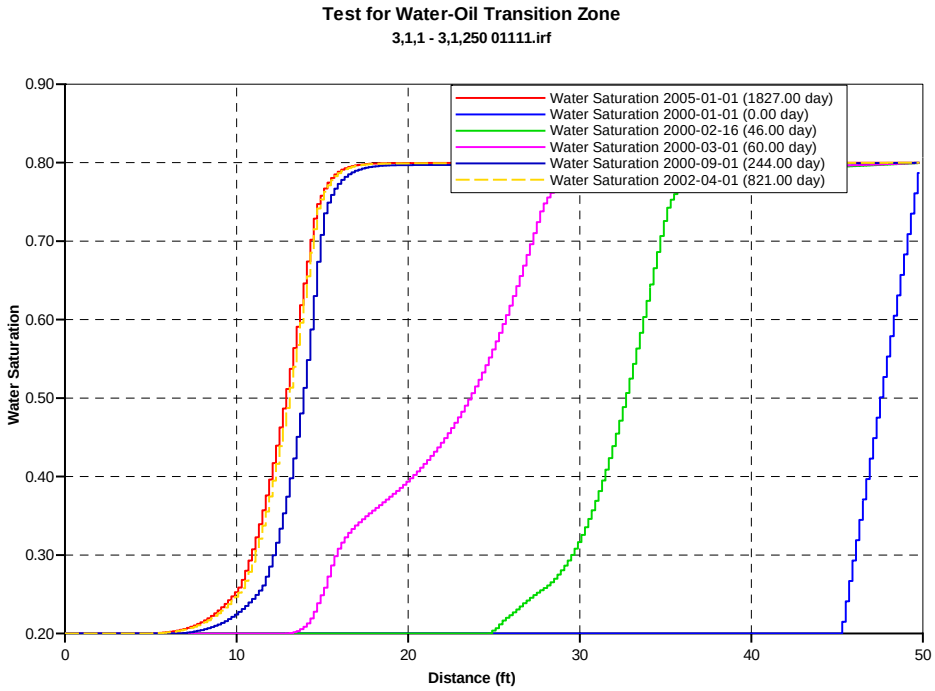

Figure B-12 Water saturation in water cone stabilizes by 26 months

B.3.2 Determination of Dimensionless Groups

The criteria of defining a dimensionless group are:

1) Each dimensionless group may be regarded as independent from other groups.

2) The parameters in the groups should involve all the important factors controlling the process.

Referring to other studies on the water coning process (Henley, 1963 and Zhou, 1981), the dimensionless groups are used (shown in Table B-3).

Table B-3 Dimensionless group design

Symbol	Dimensionless Name	Expression
M	Mobility Ratio	$M_W^o = \frac{k_{rw}^o \mu_o}{k_{ro}^o \mu_w}$
F_p	Penetration Ratio	$F_p = \frac{h_p}{h_o}$
N_B	Bond Number	$N_B = \frac{\Delta\rho g h_o}{p_c}$
W_{sp}	Well Spacing	$W_{sp} = \frac{a}{h_o}\sqrt{\frac{k_V}{k_H}}$
G	Gravity Number	$G = 4.9\times10^{-4}\frac{k k_{rw}^o A \Delta\rho g}{q_t \mu_w}$

k_{rw}^o = relative permeability for water phase at end point

k_{ro}^o = relative permeability for oil phase at end point

a = inter-well distance

A = area per well

h_o = thickness of oil layer

h_p = perforation interval

q_t = total flow rate

To ensure that every group has a monotonic increase, a reverse of Bond and Gravity number is used. Based on the dissertation of Hernandez's (2007), "Energy Statistics," a four-

level experiment with seven factors is designed in Table B-4. Using the following relations, the factor values may be normalized into various levels.

In those expressions (from Eq. (B.7) to Eq. (B.13)), x represents the level, and y represents the factor.

Oil viscosity: $y = 0.48e^{1.32x}$……....(B.7)

Perforation ratio: $y = 0.1x + 0.2$…….....(B.8)

Capillary Pressure: $y = 0.1x + 0.3$ …….....(B.9)

Vertical Permeability: $y = 13.94e^{0.88x}$……..(B.10)

Oil Density: $y = 2.11x + 46.76$…….(B.11)

Flow Rate: $y = 240.22e^{1.33x}$……..(B.12)

Well Space: $y = 320.00x + 470.00$……...(B.13)

Table B-4 Seven parameters in four levels

Symbol	Factor Name	Unit	Factor Range			
			0	1	2	3
μ_o	Oil Viscosity	cp	0.5	2	5	30
F_p	Penetration Ratio	fraction	0.2	0.3	0.4	0.5
p_c	Capillary Pressure	psi	0.3	0.4	0.5	0.6
k_V	Vertical Permeability	md	10	30	80	150
ρ_o	Oil Density	lb/ft^3	46.8	48.7	51.2	53
Q	Flow Rate	B/D	200	1000	5000	10000
A	Well Space	ft	500	800	1200	1500

The corresponding dimensionless groups have four levels as well (shown in Table B-5). In this water oil transition zone study, the oil and water velocity are uncertain without running the model. Hence, a capillary number is not applicable. However, a Bond number is useful, as cited by Zhou et al. (1997). Values of $1/N_B$ in this study have the same range as Zhou's scaling analysis. Values of M, $W_{SP,}$ and 1/G are in the same range of Hernandez's practical range of a bottom water drive. F_P is selected from the general perforation conditions mentioned in many literatures. To reduce the total runs of full factorial experiments, an orthogonal array is used to

determine the minimum runs, as well as meanwhile obtain a reasonable relationship between the dimensionless groups.

Table B-5 Dimensionless groups in four levels

Symbol	Factor Name	Factor Range			
		0	1	2	3
M	Mobility Ratio	0.50	2.00	5.00	30.00
F_p	Penetration Ratio	0.20	0.30	0.40	0.50
$1/N_B$	Capillary to Viscous Force Ratio	0.0534	0.0806	0.1221	0.1729
W_{sp}	Well Spacing	1.7	4.7	11.5	19.6
1/G	Viscous to Gravity Force Ratio	0.006	0.013	0.034	0.052

In each simulation run, an ultimate water cut for the bottom water system is considered in order to make the flowing system reach stabilization. The following plots (Figures B.13 to B.16) consist of the 16 cases. The combination was generated using the method of orthogonal array. The transition zone ratio (a response factor) is calculated for each case. The combinations of five dimensionless groups are listed in Table B-6.

Table B-6 The results of four-level of five factors using Orthogonal Array

Orthogonal Arrays	**M**	**F_p**	**$1/N_B$**	**W_{sp}**	**1/G**	***H_{TZ}* (ft) at $r=r_w$**	***Static Water Transition Zone Thickness(ft)***	***Ratio of Water Transition Zone Thickness (Dynamic/Static)***
00000	0.50	0.20	0.053	1.69	0.01	2.8	2.6	1.08
01111	0.50	0.30	0.081	6.05	0.01	8.4	5.0	1.68
02222	0.50	0.40	0.122	10.69	0.05	17.8	7.0	2.54
03333	0.50	0.50	0.173	19.64	0.05	19.4	10.6	1.83
10123	2.00	0.20	0.081	10.69	0.05	14.8	5.0	2.96
11032	2.00	0.30	0.053	19.64	0.05	17.8	2.6	6.85
12301	2.00	0.40	0.173	1.69	0.01	13.4	10.6	1.26
13210	2.00	0.50	0.122	6.05	0.01	8.8	7.0	1.26
20231	5.00	0.20	0.122	19.64	0.01	17.4	7.0	2.49
21320	5.00	0.30	0.173	10.69	0.01	16.4	10.6	1.55
22013	5.00	0.40	0.053	6.05	0.05	15	2.6	5.77
23102	5.00	0.50	0.081	1.69	0.05	13.6	5.0	2.72
32130	30.00	0.40	0.081	19.64	0.01	11.8	5.0	2.36
33021	30.00	0.50	0.053	10.69	0.01	15	2.6	5.77
33231	30.00	0.50	0.122	19.64	0.01	16.6	7.0	2.37
32220	30.00	0.40	0.122	10.69	0.01	13.4	7.0	1.91

The results in Table B-6 indicate that a run with less capillary pressure may have a similar transition zone as larger capillary cases, after the water cone stabilizes at the perforated interval. The results also show that there is no direct relationship between the thickness of the original static transition zone and the dynamic transition zone. Yet the thickness affects the ratio of the transition zone, because a fractional flow dominates the upward water coning.

All sixteen runs having stabilized water cones are shown in Figures B.13 to B.16. The sixteen snapshots are grouped on oil viscosity. For each simulation case, the snapshot shows a stabilized transition zone in a reservoir, which reaches a steady state condition for at least 10 years.

Analyzing the iso-saturation curves, the low water saturation layers are thicker than high water saturation. For instance Case 01111 in Figure B-13, the thickness of the transition zone for 6 ft of water saturation equals between 0.2 and 0.5. There is only 2.4 ft between water saturation 0.5 to 0.8. Less water saturation has a closer density to oil, while a viscous force has more impact on the transition zone.

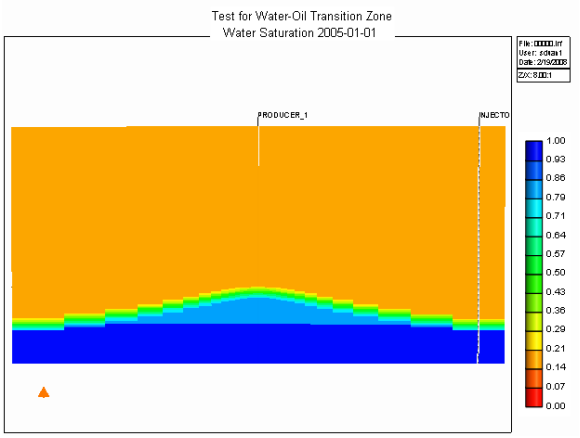

Case 00000
Radius of reservoir=500 ft
Thickness of static transition zone =2.6 ft
Thickness of dynamic transition zone at well =8.4 ft

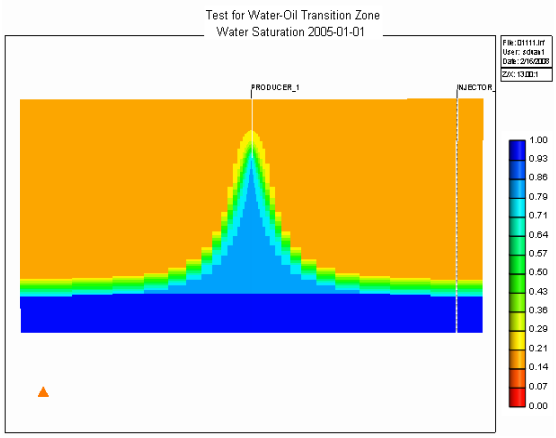

Case 01111
Radius of reservoir=800 ft
Thickness of static transition zone =5 ft
Thickness of dynamic transition zone at well =2.8 ft

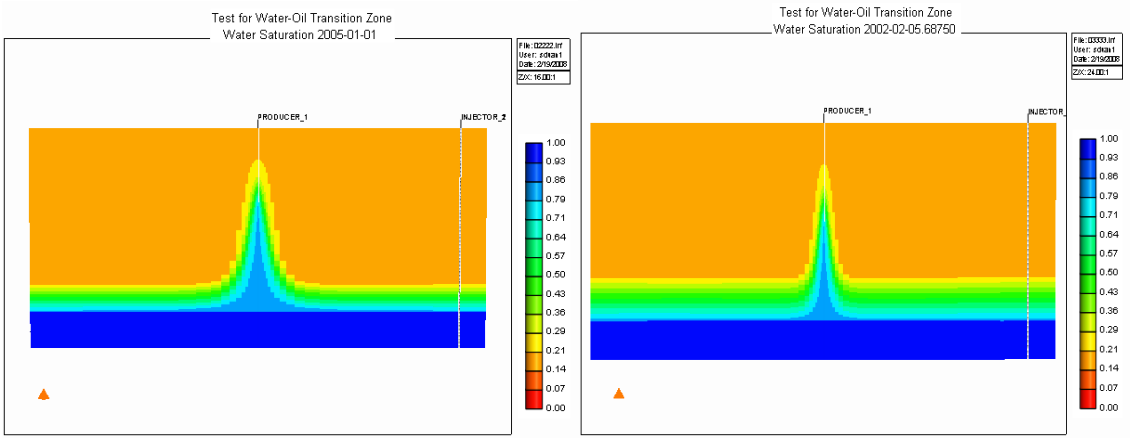

Case 02222
Radius of reservoir=1000 ft
Thickness of static transition zone =7 ft
Thickness of dynamic transition zone at well =19.4 ft

Case 03333
Radius of reservoir=1500 ft
Thickness of static transition zone =10.6 ft
Thickness of dynamic transition zone at well = 17.8 ft

Figure B-13 Water cone in steady state when oil viscosity is 0.2 cp

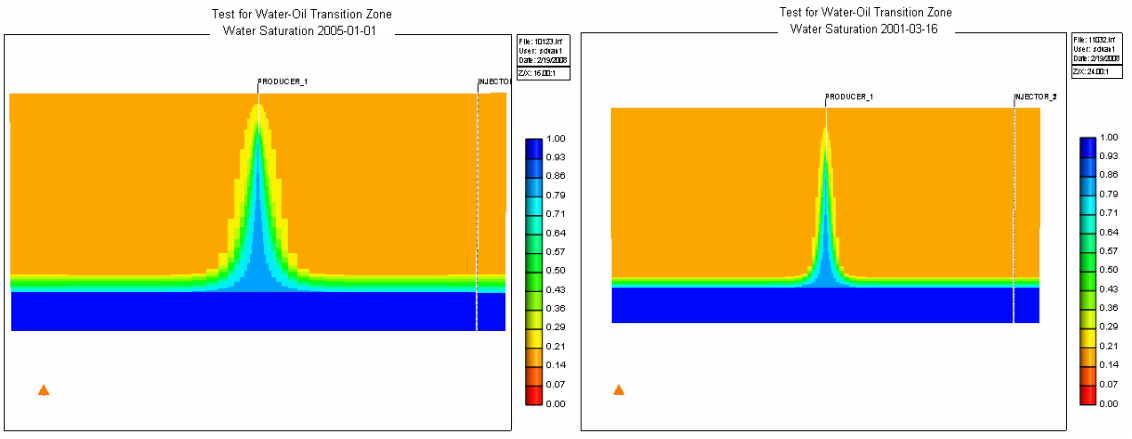

Case 10123
Radius of reservoir=1000 ft
Thickness of static transition zone = 5 ft
Thickness of dynamic transition zone at well = 14.8 ft

Case 11032
Radius of reservoir=1500 ft
Thickness of static transition zone = 2.6 ft
Thickness of dynamic transition zone at well = 17.8 ft

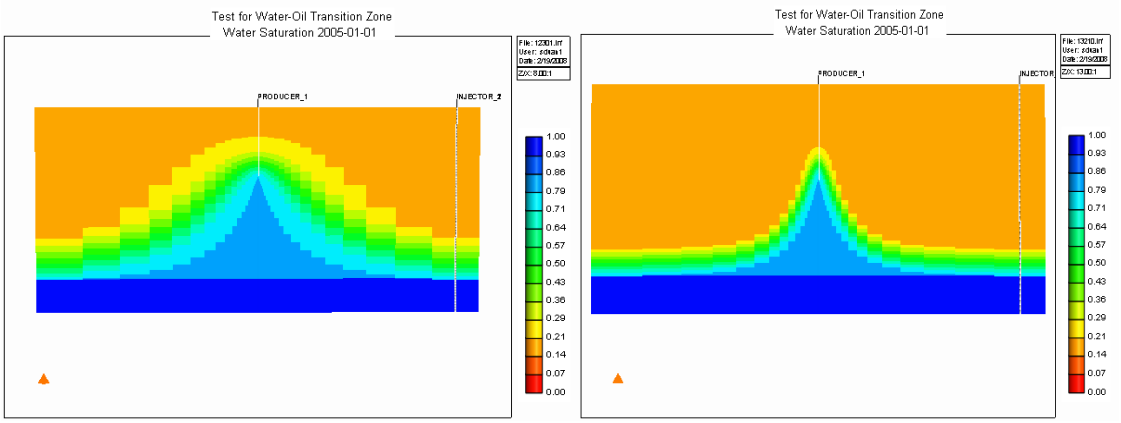

Case 12301
Radius of reservoir=500 ft
Thickness of static transition zone =10.6 ft
Thickness of dynamic transition zone at well = 8.8 ft

Case 13210
Radius of reservoir=800 ft
Thickness of static transition zone =7 ft
Thickness of dynamic transition zone at well =13.4 ft

Figure B-14 Water cone in steady state when oil viscosity is 2 cp

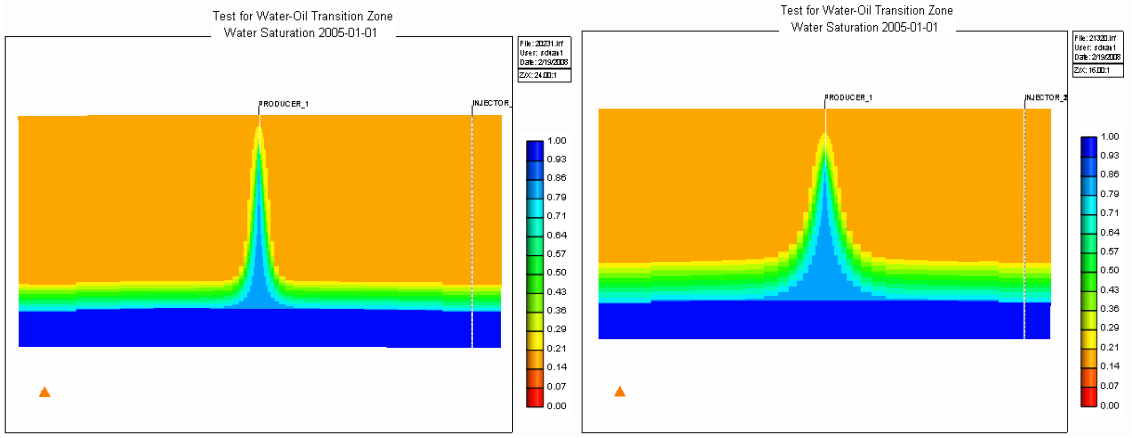

Case 20231
Radius of reservoir=1500 ft
Thickness of static transition zone =7 ft
Thickness of dynamic transition zone at well = 16.4 ft

Case 21320
Radius of reservoir=1000 ft
Thickness of static transition zone =10.6 ft
Thickness of dynamic transition zone at well =17.4 ft

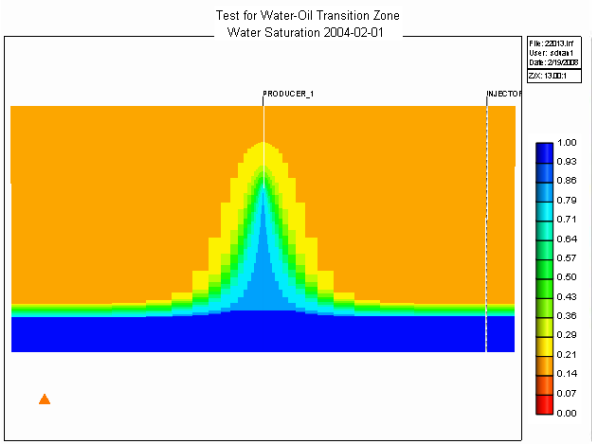

case 22013
Radius of reservoir=800 ft
Thickness of static transition zone =2.6 ft
Thickness of dynamic transition zone at well= 13.6 ft

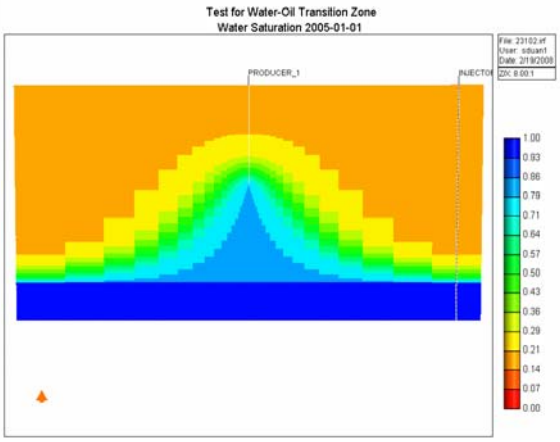

case 23102
Radius of reservoir=500 ft
Thickness of static transition zone =5 ft
Thickness of dynamic transition zone at well = 15 ft

Figure B-15 Water cone in steady state when oil viscosity is 5 cp

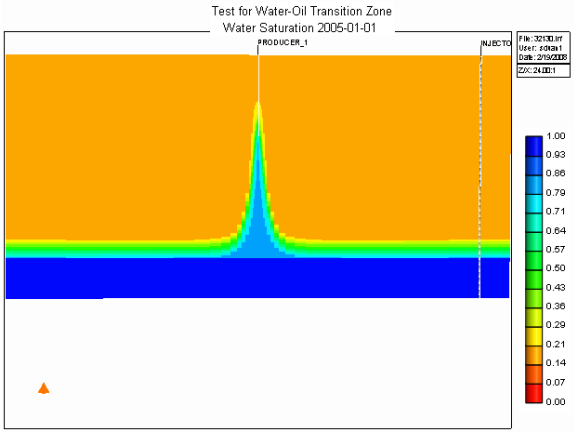

Case 32130
Radius of reservoir=1500 ft
Thickness of static transition zone =5 ft
Thickness of dynamic transition zone at well = 15 ft

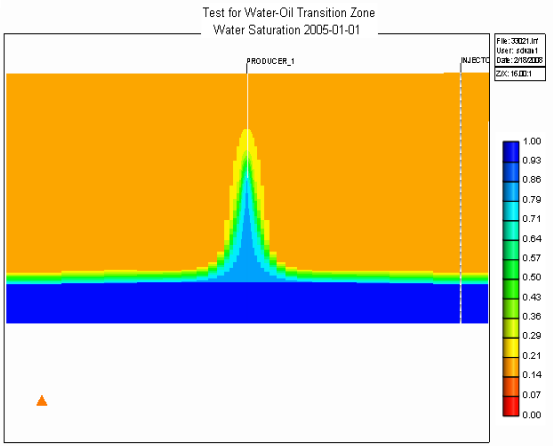

Case 33021
Radius of reservoir=1000 ft
Thickness of static transition zone =2.6 ft
Thickness of dynamic transition zone at well =11.8 ft

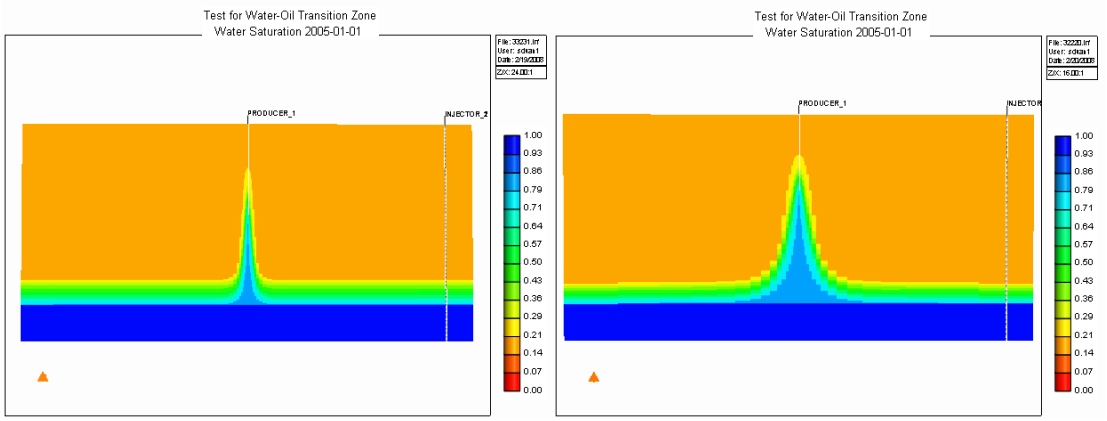

Case 33231
Radius of reservoir=1500 ft
Thickness of static transition zone =7 ft
Thickness of dynamic transition zone at well = 13.4 ft

Case 32220
Radius of reservoir=1000 ft
Thickness of static transition zone =7 ft
Thickness of dynamic transition zone at well = 16.6 ft

Figure B-16 Water cone in steady state when oil viscosity is 30 cp

B.3.3 Sensitivity analysis and regression

The response is interpreted using the statistical package R (VER 2.5). Based on 26 runs, two types of regression are used to find the relationships between factors and the response.

B.3.3.1 Linear relation:

$$Y=2.9585+0.2614*\ln(M)+1.588F_P-25.24171/N_B+0.0661*W_{SP}+32.6798*1/G \text{.....(B.14)}$$

Here, Y represents the transition zone ratio. In this regression, multiple R-Squared (correlation coefficient) is 0.75; Residual standard error is 1.09 on 20 degrees of freedom. Table B-7 shows ANOVA results.

Table B-7 ANOVA results of linear regression

	Df	Sum Sq	Mean Sq	F value	Pr(>F)	
X	5	41.234	8.247	11.79	2.09E-05	***
Residuals	20	13.989	0.699			

B.3.3.2 Quadratic relation:

$$Y=1.6085-0.9665*\ln(M)+87.086*F_P-31.8873*1/N_B+0.0295*W_{SP}+30.3159*1/G-0.2196*(\ln(M))^2-10.44*F_P^2+80.5801(1/N_B)^2-0.0041*W_{SP}^2+199.2426*(1/G)^2 \text{……(B.15)}$$

In this regression, multiple R-Squared (correlation coefficient)is 0.94; Residual standard error: 0.7556 on 15 degrees of freedom. Table B-8 shows ANOVA results.

Table B-8 ANOVA results of quadratic regression

	Df	Sum Sq	Mean Sq	F value	Pr(>F)	
X	10	51.875	5.187	23.237	2.42E-07	***
Residuals	15	3.349	0.223			

B.3.4 Discussion

In equation (B.14) to (B.15), the correlation coefficient of linear regression shows that the factors show poor relations with response factor. However, when comparing linear regression, the quadratic equation (B.15) indicates a relatively good relation between the factors and the response.

In a further investigation of quadratic relations, the analysis of variance is shown in Table B-9. The Pareto plot for the normalized coefficient is shown in Figure B-17. The Bond number related to capillary pressure is the most sensitive factor for the transition zone size. Its influence is most significant.

Table B-9 Coefficients significance evaluation from t-Test

Level	Estimate	Std. Error	t value	Pr(>|t|)	
(Intercept)	1.20536	0.42159	2.859	0.011945	*
M	1.21503	0.33372	3.641	0.002415	**
F_p	0.65287	0.33403	1.955	0.06954	.
$1/N_B$	-2.4707	0.33385	-7.401	2.22E-06	***
W_{sp}	1.10739	0.32994	3.356	0.004329	**
1/G	1.91055	0.34174	5.591	5.15E-05	***
M^2	-0.26866	0.10692	-2.513	0.023898	*
$(F_p)^2$	-0.16557	0.09932	-1.667	0.116234	
$(1/N_B)^2$	0.51607	0.10653	4.844	0.000214	***
$(W_{sp})^2$	-0.21461	0.10569	-2.031	0.060417	.
$(1/G)^2$	-0.45983	0.11982	-3.838	0.001614	**

Signif. codes: 0 '***' 0.001 '**' 0.01 '*' 0.05 '.' 0.1 ' ' 1

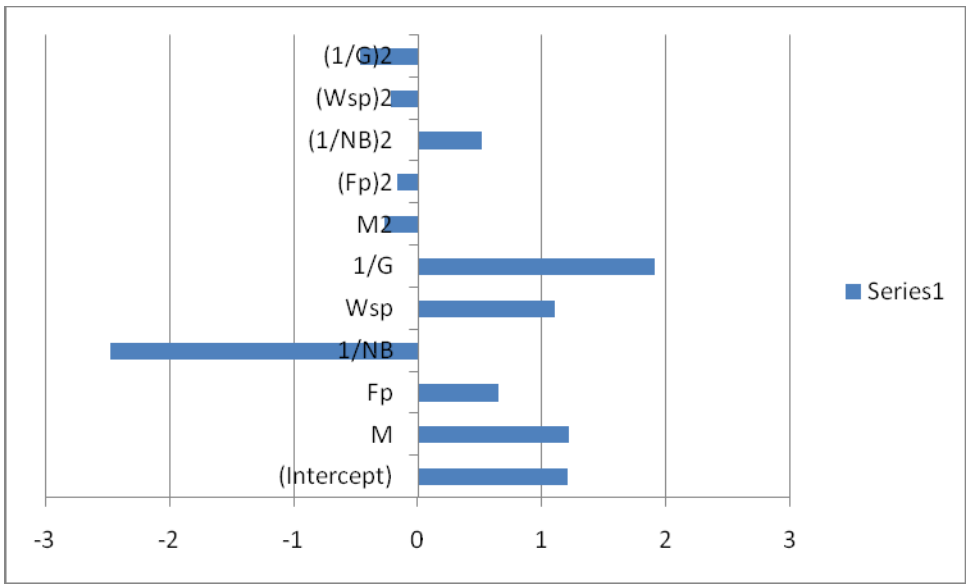

Figure B-17 "Normalized" coefficient for quadratic model of transition zone ratio

B.4 Summary

1. Analogous to a vertical, fractional water displacement, the mechanism of water coning is analyzed using associated displacement parameters.
2. To make the study practical, dimensionless groups for water displacement were used in construction of the numerical models. A numerical simulation of the transition zone was applied. The dynamic water oil transition zone in a water cone is found to always be larger than the static capillary transition zone.
3. Based on the transition zone surface model and analysis, the model's correlation coefficient (R-squared) of the quadratic regression is 0.94. This indicates a good relationship between factors and the ratio of transition zone thickness. With the derived equation (Eq. (B.15)), the transition zone thickness can be evaluated.
4. From the variance analysis, the Bond number and gravity number have significant impact on the ratio of transition zone thickness.

APPENDIX C

MECHANISTIC ANALYSIS OF TRANSVERSE MIXING

C.1 Distribution of Water and Oil in a Throat

The two phases' saturation can be computed when throat area S_p and area of oil blob can be estimated. Figure C-1 and C-2 shows different schematics of the side view and cross-section of oil blobs flowing through throats (Patzek, 2001).

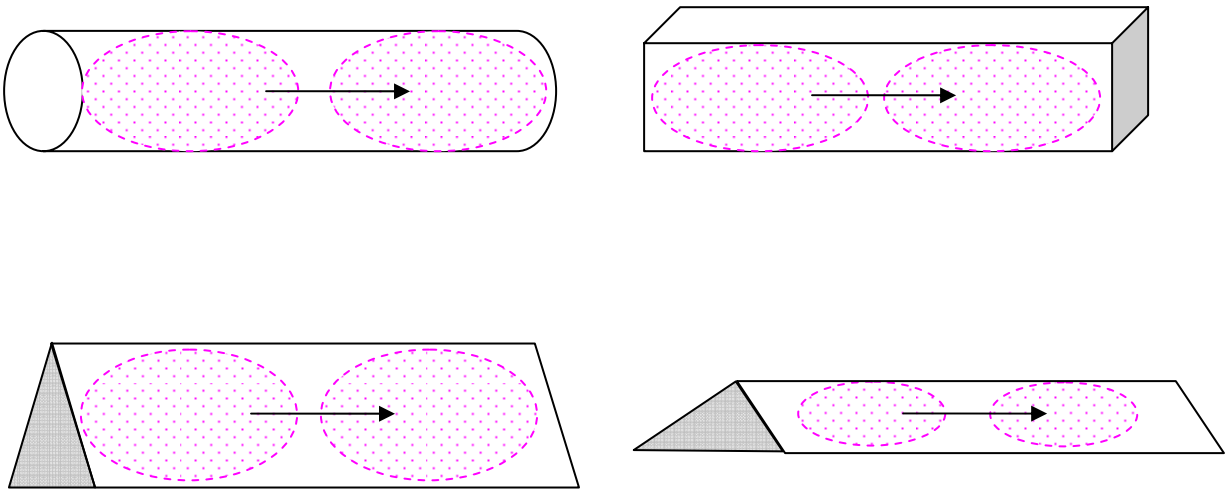

Figure C-1 Side view of water oil distribution in different shapes of throat

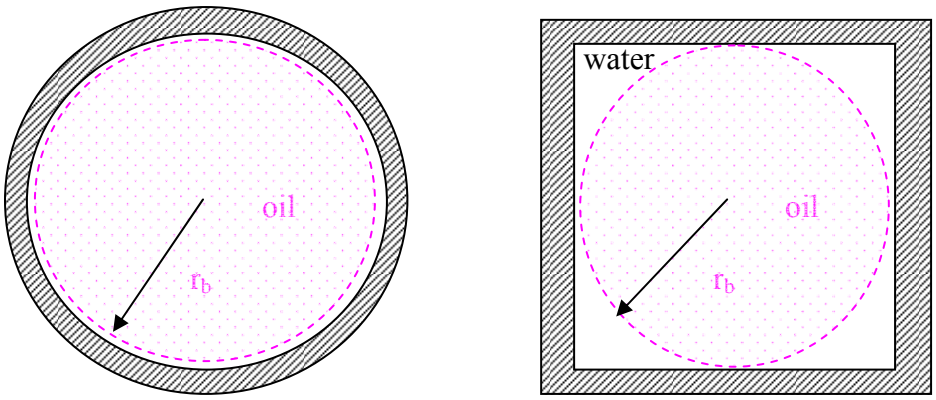

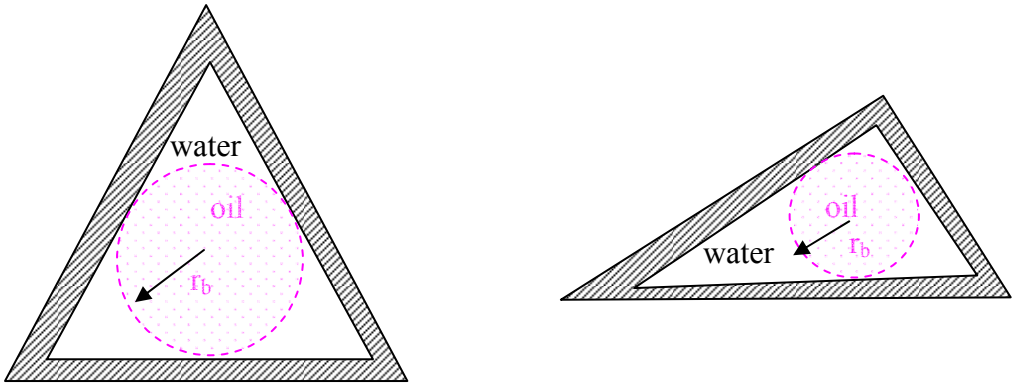

Figure C-2 Schematics of water oil distribution in different shapes of throat (cross-section)

In Figure C-2, various shapes of throats with effective flow area (S_{pe}) is shown, accompanying the wet phase's (shadowed) film. The S_{pe} value for a round throat could be approximately known from capillary tube experiments. For square and triangular throats, S_{pe} could be computed if connate water saturation is known.

$$1 - S_{wc} = \frac{S_{pe}}{S_p} \quad \text{.....(C.1)}$$

Where, S_p = area of throat, $[L^2]$

When oil blob occupies the space of throat, the saturation of movable water is computed by the remained area divided by total effective flow area,

$$S_w = \frac{(S_{pe} - S_b)}{S_{pe}} \quad \text{.....(C.2)}$$

Where, S_b = area of oil blobs, $[L^2]$

Since the distribution of oil phase in porous media is related to displacement patterns (Raimondi and Torcaso, 1964 and Dixit et al, 1998), the fluids distribution due to collision in transverse direction should be described in piston-like displacement and snap-off displacement. Hence, piston-like displacement mostly occurs in round throats; Snap-off may occur in other shapes throats.

C.2 Piston-Like Displacement after Collision

Collisions between objects are governed by laws of momentum and energy. In theory, when a collision occurs in an isolated system, the total momentum of the system of objects is conserved. (Provided that there are no net external forces acting upon the objects, the momentum of all objects before the collision equals the momentum of all objects after the collision.) If there are only two objects involved in the collision, the momentum change of individual objects is equal in magnitude and opposite in direction.

Figure 4.4-b in Chapter 4 represents one type of flow in water oil transition zone. Here, we use this model to analyze the process of fluid/grain and fluid/fluid collisions (Figure C-3). For homogeneous rocks, the flow direction of fluid after the fluid collides with the grain will change (Perkins and Johnston, 1969 and Greenkorn et al, 1964) - "1" represents the horizontal flowing direction. "2" represents the downwards direction and "3" represents the upwards direction. It is also assumed that the average sizes of throats where water and oil flow are the same.

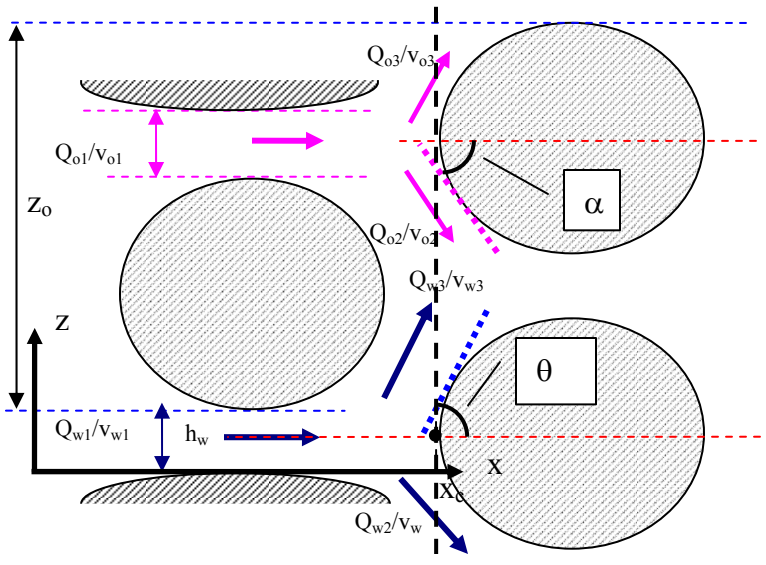

Figure C-3 Schematic of collision effect at W/O interface

The boundary conditions:

S_w ($x<x_c$, $z>h_w$, t) = S_{wi}

S_w ($x<x_c$, $z<h_w$, t) = 1-S_{oi}

Where, x_c is the position where water stream collide with the grain.

t is time.

S_{wi} is irreducible water saturation.

S_{oi} is unmovable oil saturation.

In Figure C-3, the water and oil prior to collision flow in separated throats. The thickness of oil layer is z_o, below it is water layer. A dash line at x_c separates the status of "before" and "after" collision. The fluid-grain collision angles for water and oil are represented by θ and α, respectively. Both angles should be bigger than zero and less than 90 degree. In other words, after collisions, the momentum transfer in vertical direction must not be zero in the following derivations. In homogeneous rocks, θ is assumed equal to α; if rock is heterogeneous, θ is assumed not equal to α, this case will be not discussed here.

Based on the momentum theory and a bifurcated flow model, two continuous processes will take place, i.e., the fluid collide with the grain surface and deviated fluids will combine. As the flow in the well vicinity has relatively high velocity, the Reynolds number of the flow is over 0.1. Therefore, the velocity solution of a laminar flow around a sphere (Greenkorn et al, 1964) gives a good velocity reference in the bifurcated flow model. The velocity of water after an impingement can be expressed as

$$v_{w2} = v_{w1} C_v(\mathrm{Re}, a, \omega) \quad \text{.....(C.3)}$$

Where, C_v is a parameter determined by Reynolds number (R_e), distance (a) away from the center of the impinging grain (sphere), and the angle ω (usually 90 degree). v_{w3}, v_{o2}, and v_{o3} have the similar correlation.

Considering no energy loss at collision, water velocity and rate in each direction is

$$Q_{w1} = Q_{w2} + Q_{w3} \quad \text{.....(C.4)}$$

And similarly, oil velocity and rate in each direction is

$$Q_{o1} = Q_{o2} + Q_{o3}$$

Then the collision between two deviated fluid streams or the total momentum of collision of two fluids at the W/O contact is

$$m_{w3}v_{w3} - m_{o2}v_{o2} \quad \text{.....(C.5)}$$

Eq. (C.5) can be written as

$$Q_{w3}\rho_w v_{w3} - Q_{o2}\rho_o v_{o2} \quad \text{.....(C.6)}$$

The momentums vector is partitioned into two parts, which consist of horizontal and vertical components. The horizontal momentums will not affect the transverse flow after collision. Hence, only vertical momentum contributes to the transverse flow. The comparison of vertical momentum becomes

$$Q_{w3}\rho_w v_{w3}\sin^2\theta - Q_{o2}\rho_o v_{o2}\sin^2\alpha \quad \text{.....(C.7)}$$

In Figure C-2, $F=\rho v^2 A$ is used to evaluate the resultant force for the collision of two flow streams.

In order to find the transverse velocity of the deviated flow, the flow streams' forces after collision are partitioned into vertical and horizontal components. The horizontal component is described as $\rho_w {v_{w3}}^2 A_{w3}\cos^2\theta$ and $\rho_o {v_{o2}}^2 A_{o2}\cos^2\alpha$ for water and oil streams, respectively. The horizontal components do not affect the transverse flow. The vertical component is described as $\rho_w {v_{w3}}^2 A_{w3}\sin^2\theta$ and $\rho_o {v_{o2}}^2 A_{o2}\sin^2\alpha + \rho_w V_{w3}$ for water and oil streams, respectively.

If the vertical water force is bigger than the vertical oil force,

$$\rho_w {v_{w3}}^2 A_{w3}\sin^2\theta > (\rho_o {v_{o2}}^2 A_{o2}\sin^2\alpha + \rho_w V_{w3}) \quad \text{.....(C.8)}$$

It indicates that the upward force on the water is larger than the downward force on the oil. When the two fluids impact after collision, the collided two streams will move upward, and the velocity will change to

$$Q_{w3}\rho_w v_{w3}\sin^2\theta - Q_{o2}\rho_o v_{o2}\sin^2\alpha = (Q_{w3}\sin\theta\rho_w + Q_{o2}\sin\alpha\rho_o)v_{wo3} \quad \text{.....(C.9)}$$

We have upward water velocity

$$v_{wo3} = \frac{Q_{w3}\rho_w v_{w3}\sin^2\theta - Q_{o2}\rho_o v_{o2}\sin^2\alpha}{Q_{w3}\rho_w \sin\theta + Q_{o2}\rho_o \sin\alpha} \quad \text{.....(C.10)}$$

When the vertical water force is less than vertical oil force,

$$\rho_w {v_{w3}}^2 A_{w3}\sin^2\theta < (\rho_o {v_{o2}}^2 A_{o2}\sin^2\alpha + \rho_w V_{w3}) \quad \text{.....(C.11)}$$

It indicates that there is no upward dispersed water. In other words, the downward oil force is larger than the upward water force. When the two fluids impact each other, the resultant velocity will change to

$$Q_{o2}\sin\alpha\rho_o v_{o2}\sin\alpha - Q_{w3}\sin\theta\rho_w v_{w3}\sin\theta = (Q_{w3}\sin\theta\rho_w + Q_{o2}\sin\alpha\rho_o)v_{ow3} \quad \text{.....(C.12)}$$

Then, we have downward oil velocity

$$v_{ow2} = \frac{Q_{o2}\rho_o v_{o2}\sin^2\alpha - Q_{w3}\rho_w v_{w3}\sin^2\theta}{Q_{w3}\rho_w \sin\theta + Q_{o2}\rho_o \sin\alpha} \quad \text{.....(C.13)}$$

C.3 Ratio of Dispersed Flow Rate

The momentum equation of flowing fluids can be converted from $Ft = m\Delta v$ to

$$F = \rho v^2 A \quad \text{.....(C.14)}$$

In Figure C-3, there is no force parallel to the horizontal direction. The oil flow based on Eq. (C.14)

$$-\rho_o {v_{o1}}^2 A_{o1}\cos^2\alpha - \rho_o {v_{o3}}^2 A_{o3} + \rho_o {v_{o2}}^2 A_{o2} = 0 \quad \text{.....(C.15)}$$

Where, ρ_o and v_o are the oil density and the velocity. They are both constant values in case that the flow stream is away from the grain's center. Hence,

$$-A_{o1}\cos^2\alpha - A_{o3} + A_{o2} = 0 \quad \text{.....(C.16)}$$

Because the flow rate is a constant value,

$$A_{o1} = A_{o2} + A_{o3} \quad \text{.....(C.17)}$$

Substitute Eq. (C.17) to (C.16), we get

$$\frac{A_{o3}}{A_{o2}} = \frac{\sin^2\alpha}{1+\cos^2\alpha} \quad \text{.....(C.18)}$$

The velocities in two directions are the same, so

$$\frac{Q_{o3}}{Q_{o2}} = \frac{\sin^2\alpha}{1+\cos^2\alpha} \quad \text{.....(C.19)}$$

Rearranging Eq. (C.19), we have

$$Q_{o2} = \frac{1+\cos^2\alpha}{2} Q_{o1} \quad \text{.....(C.20)}$$

$$Q_{o3} = \frac{\sin^2\alpha}{2} Q_{o1} \quad \text{.....(C.21)}$$

For water impulsion, the results are similar.

$$\frac{A_{w3}}{A_{w2}} = \frac{\sin^2\theta}{1+\cos^2\theta} \quad \text{.....(C.22)}$$

$$\frac{Q_{w3}}{Q_{w2}} = \frac{\sin^2\theta}{1+\cos^2\theta} \quad \text{.....(C.23)}$$

$$Q_{w2} = \frac{1+\cos^2\theta}{2} Q_{w1} \quad \text{.....(C.24)}$$

$$Q_{w3} = \frac{\sin^2\theta}{2} Q_{w1} \quad \text{.....(C.25)}$$

Water and oil flow rate ratios are obtained

$$\frac{Q_w}{Q_o} = \frac{A_{w1}\mu_o}{A_{01}\mu_w} \quad \text{.....(C.26)}$$

$$Q_{w1} = \frac{A_{w1}\mu_o}{A_{o1}\mu_w} Q_{o1} \quad \text{.....(C.27)}$$

C.4 Water Saturation after Collision

After fluids collide with grains, the split fluids will start to collide to each other. Thus, there are uncertainties of water invasion to oil stream, and vice versa which depends on the fluid's momentum. For a certain space such as the oil layer (z_o) before collision (Figure C-3), the ratio of water rate to the total flow rate (Q_{o1}) in the incident flow status may be approximately equal to the movable water saturation in the rock based on the theory of material balance. To evaluate saturation change, three possible consequences after a collision are discussed as follows.

Condition A: When the oil stream's momentum is larger than the water stream's momentum (see Eq. C.11), the amount of oil invading to water stream is Q_{o2} in Eq. (C.20). No water enters oil stream. The increased oil saturation that disperses into the water stream after the collision is

$$S_{o2} = \frac{\frac{1+\cos^2\alpha}{2} Q_{o1}}{(\frac{\mu_o}{\mu_w})Q_{o1}} = \frac{(1+\cos^2\alpha)\mu_w}{2\mu_o} \quad \text{.....(C.28)}$$

Condition B: When the water's momentum is larger than the oil momentum (see Eq. C.8). Change of the water saturation in the oil stream is Q_{w3} in Eq. (C.25).

$$S_{w3} = \frac{\frac{\sin^2\theta}{2} Q_{w1}}{(\frac{\mu_w}{\mu_o})Q_{w1}} = \frac{\sin^2\theta\mu_o}{2\mu_w} \quad \text{.....(C.29)}$$

Condition C: When the water stream's momentum is the same as oil stream, there is no mass transfer between the two fluids.

C.5 Snap-Off Displacement after Collision

Based on the momentum theories discussed in the previous section, fluids will alter their flow path according to Eq. (C.8) and (C.11). We assume that water has lower viscosity in the case, thus water will invade oil layer.

Instead of piston-like displacement, however, Figure C-4 shows the oil streams (pink dash line) may be split by water streams (blue dash line) in water-wet porous media after a collision. For this type of displacement process, Roof (1970) included a discussion that for a given shape of constriction, there is the minimum size to the protruding portion of the oil that permits snap-off.

If the radius of blob is known as r_b, volume of the blob V_b is

$$V_b = \frac{4}{3}\pi r_b^{\,3} \qquad \text{.....(C.30)}$$

If oil blob is lagged due to capillary pressure, the snap-off time should be evaluated.

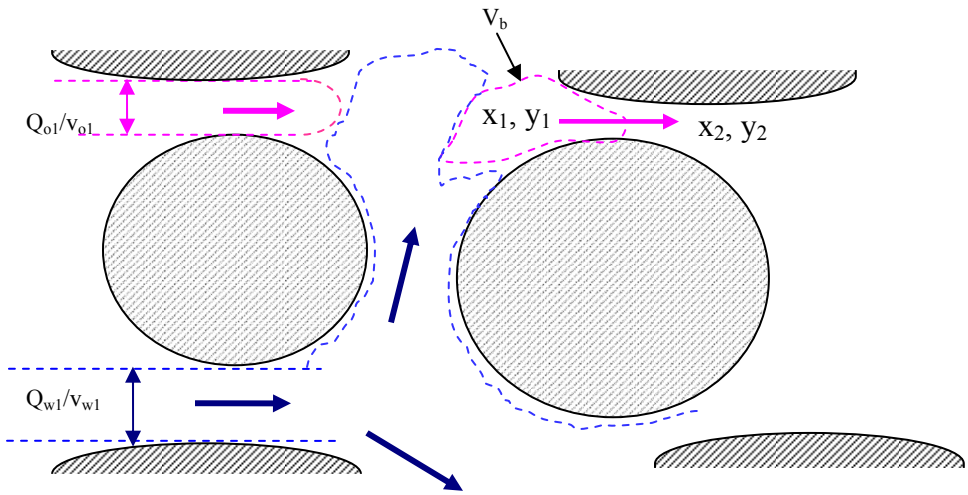

Figure C-4 Schematic of snap-off after collision at W/O interface

The snap-off time may be computed using Eq. (C.30) by Fall *et al.* (1988)

$$t_{so} = \frac{a_{so}}{p_{(x_1,y_1)} - p_{(x_2,y_2)} - p_c} \qquad \text{.....(C.31)}$$

Where, a_{so} = constant of proportionality, Pa.s

$p_{(x1,y1)}$ = pressure at starting point in a pore throat, psi

$p_{(x2,y2)}$ = pressure at ending point in a pore throat, psi

Mogensen and Stenby (1998) presented a way to compute the flow rate in pore scale,

$$G' = \frac{\pi r_{eff}^{4}}{8\mu l} \quad \text{.....(C.32)}$$

Where, G' = conductance, $ft^3/s/psi$

l = length of capillary segment, [L]

r_{eff} = effective cross-sectional area during snap-off, [L]

Hence, water flow rate can be computed from pressure difference in Eq. (C.31)

$$Q_w = G(p_{(x_1,y_1)} - p_{(x_2,y_2)}) \quad \text{.....(C.33)}$$

The total water flow volume during oil snap-off is

$$V_w = G(p_{(x_1,y_1)} - p_{(x_2,y_2)}) \times t_{so} \quad \text{.....(C.34)}$$

The water saturation may be computed in a certain space

$$S_w = \frac{V_w}{V_w + V_b} \quad \text{.....(C.35)}$$

$$S_w = \frac{\frac{(r_{pe} - r_b)^4}{\mu_w l} a}{\frac{(r_{pe} - r_b)^4}{\mu_w l} a + \frac{32}{3} r_b^{\,3} \Delta p} \quad \text{.....(C.36)}$$

Where, $\Delta p = p_{(x_1,y_1)} - p_{(x_2,y_2)} - p_c$

Eq. (C.36) indicates that the water saturation after collision with snap-off is functions of the sizes of throat and blob, pressure gradient and water viscosity. Arriola *et al.* (1980) noted that the size of blobs may be various in sizes in tube experiments. Therefore, the evaluation of water saturation has more uncertainty in snap-off condition than in piston-like displacement.

C.6 Stabilization Evaluation of Transverse Mixing

The gravity force is the primary variable for evaluating the range of consecutive dispersion. Commonly, the theory of hydraulic jump is applied in a macroscopic scale flowing system. However, at the pore scale, the conservation of energy theory is also applicable, neglecting capillary effect.

The Froude number is essentially applied. The dimensionless number is defined as

$$Fr = \frac{v_{up}}{\sqrt{gh_{up}}} \quad \text{.....(C.37)}$$

Where, v_{up} = upstream velocity, [L]/[T]

h_{up} = fluid thickness at upstream, [L]

This highly energized flow will go from supercritical (Fr >1) to subcritical (Fr <1) through a jump. Thus, the fluid's velocity should be large enough to let Fr be larger than 1; thus allowing the deviated water stream to overpass the grain after collision.

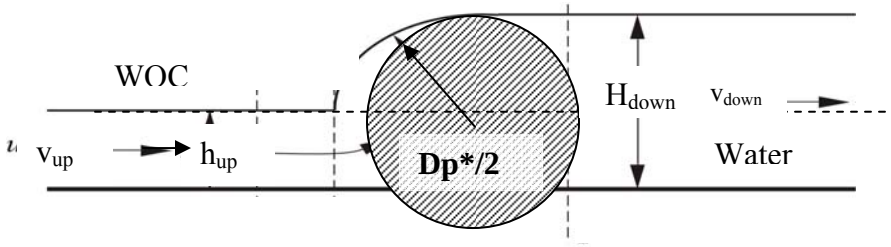

Figure C-5 Sketch of a hydraulic jump through a particle

The height of jump in a porous media can be derived, based on the theory of energy conservation. The symbols are shown in Figure C-5. We assume that the capillary effect is negligible. By application of Bernoulli's equation to the process, the energy is constant after the jump. It gives

$$\frac{p_{up}}{\rho g} + h_{up} + \frac{v_{up}^2}{2g} = \frac{p_{down}}{\rho g} + h_{down} + \frac{v_{down}^2}{2g} \quad \text{.....(C.38)}$$

Where, v_{down} = downstream velocity, [L]/[T]

h_{down} = fluid thickness at downstream, [L]

For the water flow in Figure C-5, any pressure difference is neglected. Applying the model to collision model, the water height is h_{up}. If the water stream's velocity is high enough, h_{down} will be the final water height after collision. This yields from Eq. (C.38):

$$\frac{h_{up}}{2}+\frac{v_{w1}^2}{2g}=\frac{h_{down}}{2}+\frac{v_{w3}{}^2}{2g} \quad \text{(C.39)}$$

The solution is

$$h_{down}=\frac{1}{2}(-1+\sqrt{1+8Fr_{up}})h_{up} \quad \text{(C.40)}$$

The v_{w1} is the water velocity in the main stream, and h_w' is the stable water height after collision. The ultimate dispersed water velocity v_{w3}' is the oil main stream velocity.

APPENDIX D

RESERVOIR SIMULATION DATA DECK (CMG IMEX)

D.1 Code of Two Segregated Flow in Radial Coordinate (No Mixing)

```
*TITLE1
'Test for Water-Oil Transition Zone'
*TITLE2
'35x1x140 radial grid two-phase gravity segregated problem'
*INUNIT *FIELD
*WPRN  *WELL *TIME
*WPRN  *GRID *TIME
*WPRN   *ITER    *ALL
*OUTPRN *WELL *LAYER
*OUTPRN *GRID *SO *SW *OILPOT *PRES *BPP
*XDR
*WSRF  *GRID *TIME
*OUTSRF *GRID  *SO *SW *PRES *BPP *FLUXRC *VELOCRC *STRMLN
*GRID *RADIAL 35   1   140
KDIR DOWN
**********************************************************************
** Reservoir Description section
**********************************************************************
*DI  *IVAR
```

```
  0.25 .2 .2 .2 .2 .2 .2 .2 .2 .2 .2 .2 .2 .2 .2 .5 .5 1.0 1.0 1.0 1.0 1.0 1.0 1.0 1.0 1.0 1.0 1.0 1.0
5.0 5.0 10.0 33330.36 933370.33
  *DJ  *CON  360.0
  *DK *KVAR
  140*0.1
  *DTOP
   35*5000
    *POR  *MATRIX  *IJK
  1:25     1:1  1:140  0.39
  26:35     1:1  1:140  0.39
   *PERMI *MATRIX *IJK
  1:35     1:1  1:140   290000.
  *PERMJ *MATRIX *IJK
  1:35     1:1  1:140   290000.
  *PERMK *MATRIX *IJK
  1:35     1:1  1:140   290000.
   *PRPOR    3600.0              ** Rock compressibility and
  *CPOR     4.0E-6              ** reference pressure
 ***************************************************************************
  ** Component Properties section
***************************************************************************
   *MODEL *OILWATER              ** Two phase, water-oil problem.
   *PVT
   **    p      rs        bo        eg          viso     visg
```

```
 800.000   335.000   1.002550   338.980    2.5009000  0.0135
 1200.000   500.000   1.003800   510.200    2.500800  0.0140
 2000.000   828.000   1.006300   847.460    2.500600  0.0150
 2400.000   985.000   1.007500  1020.400    2.500500  0.0155
 2800.000  1030.000   1.008700  1190.500    2.500400  0.0160
 3200.000  1070.000   1.009850  1351.400  2.50030000  0.0165
 3600.000  1090.000   1.011000  1538.500  2.50020000  0.0170
** Light oil and normal water
*DENSITY *OIL   62.0
*DENSITY *GAS    0.07
*DENSITY *WATER 62.4
*CO       3.50E-6
*CVO      0.0
*BWI      1.0
*CW       3.50E-6
*REFPW    15.0
*VWI      0.6
*CVW      0.0
**********************************************************************
** Rock-fluid Properties Section
**********************************************************************
*ROCKFLUID
*RPT  1
*SWT
```

```
 **  Sw        krw       krow    Pcow
  0.1        0.00      1.0     0.0
  0.90       1.00      0.0     0.0
*RTYPE *IJK
   1:35    1:1    1:140    1    ** Top and bottom layers are the same
*INITIAL
**********************************************************************
** Initial Conditions Section
**********************************************************************
*VERTICAL *BLOCK_CENTER  *WATER_OIL        ** Use depth averaged initialization.
**WATER_OIL
**USER_INPUT
*PB *CON  16.                ** Initial bubble point pressure is constant.
*REFPRES  3000.               ** Reference pressure taken at
*REFDEPTH 5000.               ** reference depth.
*DWOC    5007.0              ** Water-oil contact.
 *NUMERICAL
**********************************************************************
** Numerical Control Section
**********************************************************************
*DTMAX  5
*RUN
**********************************************************************
** Well Data Section
```

```
**************************************************************************
*DATE   2000  1  1
*DTWELL 0.0025
*AIMSET *CON  1    ** This problem is run fully implicit
*CONVERGE *SATUR 0.001
*WELL 1 'PRODUCER_1'
*PRODUCER 1
*OPERATE *MIN *BHP      200.000
*OPERATE *Max *STW      20000.000
*GEOMETRY *K 0.3 .5 1. 0.
*PERF  *GEO 'PRODUCER_1'
** if     jf     kf     wi
   1      1    1:140   1.0000E+1
*INCLUDE 'time-step-short.txt'
*STOP
```

D.2 Code of Dispersed Water Flow in Radial Coordinate for Single Oil Phase

```
*TITLE1
'Test for Water-Oil Transition Zone'
*TITLE2
'35x1x70 radial grid two-phase gravity segregated problem'
*INUNIT *FIELD
*WPRN  *WELL *TIME
*WPRN  *GRID *TIME
*WPRN   *ITER    *ALL
```

```
*OUTPRN *WELL *LAYER
*OUTPRN *GRID *SO *SW *OILPOT *PRES *BPP
*XDR
*WSRF  *GRID *TIME
*OUTSRF *GRID  *SO *SW *PRES *BPP *FLUXRC *VELOCRC *STRMLN
*GRID *RADIAL 35   1   70
KDIR DOWN
**********************************************************************
** Reservoir Description section
**********************************************************************
*DI  *IVAR
0.25 .2 .2 .2 .2 .2 .2 .2 .2 .2 .2 .2 .2 .2 .2 .5 .5 1.0 1.0 1.0 1.0 1.0 1.0 1.0 1.0 1.0 1.0 1.0 1.0
5.0 5.0 10.0 33330.36 933370.33
*DJ  *CON  360.0
*DK *KVAR
70*0.1
*DTOP
 35*5000
   *POR  *MATRIX  *IJK
1:25     1:1  1:140  0.39
26:35     1:1  1:140  0.39
*PERMI *MATRIX *IJK
1:35     1:1   1:70   290000.0
1:13     1:1  70:70        0.
```

1:10 1:1 69:69 4495.

11:17 1:1 69:69 4495.

1:5 1:1 67:69 17980.

6:13 1:1 68:68 17980.

14:19 1:1 69:69 17980.

1:4 1:1 65:67 40454.

5:5 1:1 66:67 40454.

6:7 1:1 66:68 40454.

8:14 1:1 67:68 40454.

15:19 1:1 68:68 40454.

1:4 1:1 62:64 71919.

5:5 1:1 63:65 71919.

6:7 1:1 63:65 71919.

8:9 1:1 64:66 71919.

10:12 1:1 65:67 71919.

13:15 1:1 66:67 71919.

16:20 1:1 67:67 71919.

1:4 1:1 58:61 112373.

5:5 1:1 60:62 112373.

6:7 1:1 59:62 112373.

8:8 1:1 60:63 112373.

9:12 1:1 62:64 112373.

13:16 1:1 64:66 112373.

17:20 1:1 66:66 112373.

1:4 1:1 53:57 161817.

5:5 1:1 55:59 161817.

6:7 1:1 54:58 161817.

8:8 1:1 56:59 161817.

9:11 1:1 58:61 161817.

12:14 1:1 62:64 161817.

15:17 1:1 62:63 161817.

17:20 1:1 65:65 161817.

1:4 1:1 48:52 220251.

5:5 1:1 50:54 220251.

5:7 1:1 49:53 220251.

8:9 1:1 51:55 220251.

10:12 1:1 54:57 220251.

12:14 1:1 59:61 220251.

15:17 1:1 60:61 220251.

17:20 1:1 64:64 220251.

*PERMJ *MATRIX *IJK

1:35 1:1 1:70 290000.

1:13 1:1 70:70 0.

1:10 1:1 69:69 4495.

11:17 1:1 69:69 4495.

1:5 1:1 67:69 17980.

6:13 1:1 68:68 17980.

14:19 1:1 69:69 17980.

1:4 1:1 65:67 40454.

5:5 1:1 66:67 40454.

6:7 1:1 66:68 40454.

8:14 1:1 67:68 40454.

15:19 1:1 68:68 40454.

1:4 1:1 62:64 71919.

5:5 1:1 63:65 71919.

6:7 1:1 63:65 71919.

8:9 1:1 64:66 71919.

10:12 1:1 65:67 71919.

13:15 1:1 66:67 71919.

16:20 1:1 67:67 71919.

1:4 1:1 58:61 112373.

5:5 1:1 60:62 112373.

6:7 1:1 59:62 112373.

8:8 1:1 60:63 112373.

9:12 1:1 62:64 112373.

13:16 1:1 64:66 112373.

17:20 1:1 66:66 112373.

1:4 1:1 53:57 161817.

5:5 1:1 55:59 161817.

6:7 1:1 54:58 161817.

8:8 1:1 56:59 161817.

9:11 1:1 58:61 161817.

12:14 1:1 62:64 161817.

15:17 1:1 62:63 161817.

17:20 1:1 65:65 161817.

1:4 1:1 48:52 220251.

5:5 1:1 50:54 220251.

5:7 1:1 49:53 220251.

8:9 1:1 51:55 220251.

10:12 1:1 54:57 220251.

12:14 1:1 59:61 220251.

15:17 1:1 60:61 220251.

17:20 1:1 64:64 220251.

*PERMK *MATRIX *IJK

1:35 1:1 1:70 290000.

1:13 1:1 70:70 0.

1:10 1:1 69:69 4495.

11:17 1:1 69:69 4495.

1:5 1:1 67:69 17980.

6:13 1:1 68:68 17980.

14:19 1:1 69:69 17980.

1:4 1:1 65:67 40454.

5:5 1:1 66:67 40454.

6:7 1:1 66:68 40454.

8:14 1:1 67:68 40454.

15:19 1:1 68:68 40454.

1:4 1:1 62:64 71919.

5:5 1:1 63:65 71919.

6:7 1:1 63:65 71919.

8:9 1:1 64:66 71919.

10:12 1:1 65:67 71919.

13:15 1:1 66:67 71919.

16:20 1:1 67:67 71919.

1:4 1:1 58:61 112373.

5:5 1:1 60:62 112373.

6:7 1:1 59:62 112373.

8:8 1:1 60:63 112373.

9:12 1:1 62:64 112373.

13:16 1:1 64:66 112373.

17:20 1:1 66:66 112373.

1:4 1:1 53:57 161817.

5:5 1:1 55:59 161817.

6:7 1:1 54:58 161817.

8:8 1:1 56:59 161817.

9:11 1:1 58:61 161817.

12:14 1:1 62:64 161817.

15:17 1:1 62:63 161817.

17:20 1:1 65:65 161817.

1:4 1:1 48:52 220251.

5:5 1:1 50:54 220251.

```
 5:7      1:1  49:53   220251.
 8:9      1:1  51:55   220251.
 10:12    1:1  54:57   220251.
 12:14    1:1  59:61   220251.
 15:17    1:1  60:61   220251.
 17:20    1:1  64:64   220251.
  *PRPOR    3600.0              ** Rock compressibility and
  *CPOR     4.0E-6              ** reference pressure
**************************************************************************
  ** Component Properties section
**************************************************************************
   *MODEL *OILWATER             ** Two phase, water-oil problem.
   *PVT
   **    p      rs        bo        eg          viso     visg
    800.000   335.000   1.002550   338.980    2.5009000  0.0135
   1200.000   500.000   1.003800   510.200    2.500800  0.0140
   2000.000   828.000   1.006300   847.460    2.500600  0.0150
   2400.000   985.000   1.007500  1020.400    2.500500  0.0155
   2800.000  1030.000   1.008700  1190.500    2.500400  0.0160
   3200.000  1070.000   1.009850  1351.400  2.50030000  0.0165
   3600.000  1090.000   1.011000  1538.500  2.50020000  0.0170
  ** Light oil and normal water
  *DENSITY *OIL   62.0
  *DENSITY *GAS    0.07
```

```
*DENSITY *WATER 62.4
*CO      3.50E-6
*CVO     0.0
*BWI     1.0
*CW      3.50E-6
*REFPW   15.0
*VWI     0.6
*CVW     0.0
**********************************************************************
** Rock-fluid Properties Section
**********************************************************************
*ROCKFLUID
*RPT  1
*SWT
 **  Sw       krw      krow    Pcow
  0.1       0.00      1.0     0.0
  0.90      1.00      0.0     0.0
*RTYPE *IJK
   1:35    1:1    1:70    1    ** Top and bottom layers are the same
*INITIAL
**********************************************************************
** Initial Conditions Section
**********************************************************************
*VERTICAL *BLOCK_CENTER  *WATER_OIL        ** Use depth averaged initialization.
```

```
**WATER_OIL
**USER_INPUT
*PB *CON  16.                ** Initial bubble point pressure is constant.
*REFPRES  3000.              ** Reference pressure taken at
*REFDEPTH 5000.              ** reference depth.
*DWOC    6050.0              ** Water-oil contact.
 *NUMERICAL
**********************************************************************
** Numerical Control Section
**********************************************************************
*DTMAX  5
*RUN
**********************************************************************
** Well Data Section
**********************************************************************
*DATE   2000  1  1
*DTWELL 0.0025
*AIMSET *CON  1    ** This problem is run fully implicit
*CONVERGE *SATUR 0.001
*WELL 1 'PRODUCER_1'
*PRODUCER 1
*OPERATE *MIN *BHP      200.000
*OPERATE *Max *STO      4400.000
*GEOMETRY *K 0.3 .5 1. 0.
```

```
*PERF  *GEO 'PRODUCER_1'
** if    jf    kf    wi
  1     1    1:70   1.0000E+1
*INCLUDE 'time-step-short.txt'
*STOP
```

D.3 Code of Dispersed Water Flow in Radial Coordinate for Single Oil Phase

```
*TITLE1
'Test for Water-Oil Transition Zone'
*TITLE2
'35x1x140 radial grid two-phase gravity segregated problem'
*INUNIT *FIELD
*WPRN  *WELL *TIME
*WPRN  *GRID *TIME
*WPRN   *ITER    *ALL
*OUTPRN *WELL *LAYER
*OUTPRN *GRID *SO *SW *OILPOT *PRES *BPP
*XDR
*WSRF  *GRID *TIME
*OUTSRF *GRID  *SO *SW *PRES *BPP *FLUXRC *VELOCRC *STRMLN
*GRID *RADIAL 35   1   140
KDIR DOWN
**************************************************************************
** Reservoir Description section
**************************************************************************
```

*DI *IVAR

0.25 .2 .2 .2 .2 .2 .2 .2 .2 .2 .2 .2 .2 .2 .2 .5 .5 1.0 1.0 1.0 1.0 1.0 1.0 1.0 1.0 1.0 1.0 1.0 1.0 1.0 1.0 1.0 5.0 5.0 10.0 33330.36 933370.33

*DJ *CON 360.0

*DK *KVAR

140*0.1

*DTOP

35*5000

*POR *MATRIX *IJK

1:25 1:1 1:140 0.39

26:35 1:1 1:140 0.39

*PERMI *MATRIX *IJK

1:35 1:1 1:70 0.

1:35 1:1 71:140 290000.

1:13 1:1 70:70 290000.

1:10 1:1 69:69 222286.

11:17 1:1 69:69 222286.

1:5 1:1 67:69 163562.

6:13 1:1 68:68 163562.

14:19 1:1 69:69 163562.

1:4 1:1 65:67 113828.

5:5 1:1 66:67 113828.

6:7 1:1 66:68 113828.

8:14 1:1 67:68 113828.

15:19 1:1 68:68 113828.

1:4 1:1 62:64 73083.

5:5 1:1 63:65 73083.

6:7 1:1 63:65 73083.

8:9 1:1 64:66 73083.

10:12 1:1 65:67 73083.

13:15 1:1 66:67 73083.

16:20 1:1 67:67 73083.

1:4 1:1 58:61 41329.

5:5 1:1 60:62 41329.

6:7 1:1 59:62 41329.

8:8 1:1 60:63 41329.

9:12 1:1 62:64 41329.

13:16 1:1 64:66 41329.

17:20 1:1 66:66 41329.

1:4 1:1 53:57 18564.

5:5 1:1 55:59 18564.

6:7 1:1 54:58 18564.

8:8 1:1 56:59 18564.

9:11 1:1 58:61 18564.

12:14 1:1 62:64 18564.

15:17 1:1 62:63 18564.

17:20 1:1 65:65 18564.

1:4 1:1 48:52 4790.

5:5 1:1 50:54 4790.

5:7 1:1 49:53 4790.

8:9 1:1 51:55 0.

10:12 1:1 54:57 0.

12:14 1:1 59:61 0.

15:17 1:1 60:61 0.

17:20 1:1 64:64 0.

*PERMJ *MATRIX *IJK

1:35 1:1 1:70 0.

1:35 1:1 71:140 290000.

1:13 1:1 70:70 290000.

1:10 1:1 69:69 222286.

11:17 1:1 69:69 222286.

1:5 1:1 67:69 163562.

6:13 1:1 68:68 163562.

14:19 1:1 69:69 163562.

1:4 1:1 65:67 113828.

5:5 1:1 66:67 113828.

6:7 1:1 66:68 113828.

8:14 1:1 67:68 113828.

15:19 1:1 68:68 113828.

1:4 1:1 62:64 73083.

5:5 1:1 63:65 73083.

6:7 1:1 63:65 73083.

8:9 1:1 64:66 73083.

10:12 1:1 65:67 73083.

13:15 1:1 66:67 73083.

16:20 1:1 67:67 73083.

1:4 1:1 58:61 41329.

5:5 1:1 60:62 41329.

6:7 1:1 59:62 41329.

8:8 1:1 60:63 41329.

9:12 1:1 62:64 41329.

13:16 1:1 64:66 41329.

17:20 1:1 66:66 41329.

1:4 1:1 53:57 18564.

5:5 1:1 55:59 18564.

6:7 1:1 54:58 18564.

8:8 1:1 56:59 18564.

9:11 1:1 58:61 18564.

12:14 1:1 62:64 18564.

15:17 1:1 62:63 18564.

17:20 1:1 65:65 18564.

1:4 1:1 48:52 4790.

5:5 1:1 50:54 4790.

5:7 1:1 49:53 4790.

8:9 1:1 51:55 0.

10:12 1:1 54:57 0.

12:14 1:1 59:61 0.

15:17 1:1 60:61 0.

17:20 1:1 64:64 0.

*PERMK *MATRIX *IJK

1:35 1:1 1:70 0.

1:35 1:1 71:140 290000.

1:13 1:1 70:70 290000.

1:10 1:1 69:69 222286.

11:17 1:1 69:69 222286.

1:5 1:1 67:69 163562.

6:13 1:1 68:68 163562.

14:19 1:1 69:69 163562.

1:4 1:1 65:67 113828.

5:5 1:1 66:67 113828.

6:7 1:1 66:68 113828.

8:14 1:1 67:68 113828.

15:19 1:1 68:68 113828.

1:4 1:1 62:64 73083.

5:5 1:1 63:65 73083.

6:7 1:1 63:65 73083.

8:9 1:1 64:66 73083.

10:12 1:1 65:67 73083.

13:15 1:1 66:67 73083.

16:20 1:1 67:67 73083.

```
1:4      1:1  58:61    41329.
5:5      1:1  60:62    41329.
6:7      1:1  59:62    41329.
8:8      1:1  60:63    41329.
9:12     1:1  62:64    41329.
13:16    1:1  64:66    41329.
17:20    1:1  66:66    41329.
1:4      1:1  53:57    18564.
5:5      1:1  55:59    18564.
6:7      1:1  54:58    18564.
8:8      1:1  56:59    18564.
9:11     1:1  58:61    18564.
12:14    1:1  62:64    18564.
15:17    1:1  62:63    18564.
17:20    1:1  65:65    18564.
1:4      1:1  48:52     4790.
5:5      1:1  50:54     4790.
5:7      1:1  49:53     4790.
8:9      1:1  51:55        0.
10:12    1:1  54:57        0.
12:14    1:1  59:61        0.
15:17    1:1  60:61        0.
17:20    1:1  64:64        0.
 *PRPOR    3600.0              ** Rock compressibility and
```

```
  *CPOR     4.0E-6              ** reference pressure
 ***************************************************************************
  ** Component Properties section
***************************************************************************
   *MODEL *OILWATER              ** Two phase, water-oil problem.
   *PVT
   **    p      rs        bo        eg          viso     visg
    800.000   335.000   1.002550   338.980    2.5009000  0.0135
   1200.000   500.000   1.003800   510.200    2.500800  0.0140
   2000.000   828.000   1.006300   847.460    2.500600  0.0150
   2400.000   985.000   1.007500  1020.400    2.500500  0.0155
   2800.000  1030.000   1.008700  1190.500    2.500400  0.0160
   3200.000  1070.000   1.009850  1351.400  2.50030000  0.0165
   3600.000  1090.000   1.011000  1538.500  2.50020000  0.0170
  ** Light oil and normal water
  *DENSITY *OIL   62.0
  *DENSITY *GAS    0.07
  *DENSITY *WATER 62.4
  *CO       3.50E-6
  *CVO      0.0
  *BWI      1.0
  *CW       3.50E-6
  *REFPW    15.0
  *VWI      0.6
```

```
*CVW      0.0
**********************************************************************
** Rock-fluid Properties Section
**********************************************************************
*ROCKFLUID
*RPT  1
*SWT
 **  Sw        krw       krow    Pcow
  0.1        0.00      1.0     0.0
  0.90       1.00      0.0     0.0
*RTYPE *IJK
   1:35    1:1    1:140    1    ** Top and bottom layers are the same
*INITIAL
**********************************************************************
** Initial Conditions Section
**********************************************************************
*VERTICAL *BLOCK_CENTER  *WATER_OIL        ** Use depth averaged initialization.
**WATER_OIL
**USER_INPUT
*PB *CON  16.                ** Initial bubble point pressure is constant.
*REFPRES  3000.               ** Reference pressure taken at
*REFDEPTH 5000.                ** reference depth.
*DWOC    1050.0               ** Water-oil contact.
 *NUMERICAL
```

```
**************************************************************************
** Numerical Control Section
**************************************************************************
*DTMAX  5
*RUN
**************************************************************************
** Well Data Section
**************************************************************************
*DATE   2000  1  1
*DTWELL 0.0025
*AIMSET *CON  1    ** This problem is run fully implicit
*CONVERGE *SATUR 0.001
*WELL 1 'PRODUCER_1'
*PRODUCER 1
*OPERATE *MIN *BHP      200.000
*OPERATE *Max *STW      20500.000
*GEOMETRY *K 0.3 .5 1. 0.
*PERF  *GEO 'PRODUCER_1'
** if    jf    kf    wi
  1     1    45:140   1.0000E+1
*INCLUDE 'time-step-short.txt'
*STOP
```

APPENDIX E

NOMENCLATURE

a = distance away from center of grain [L]

a = a temporary variable in Chapter 9 [L^2/T]

a_n = wave's amplitude [in]

a_{so} = constant of proportionality in snap off [Pa.s]

A = area [ft^2]

b_e = fractional thickness of the water at the outlet, fraction

C = concentration [fraction]

c_1, c_2, c_3, c_4 = constants in Eq. (4.2), dimensionless

$C_1, C_2, C_3, \overline{C}_1, \overline{C}_2$ = constants, dimensionless

C_D = coefficient of dispersion coefficient, dimensionless

c_v = coefficient of velocity after collision, dimensionless

d = diameter of tube [L]

d_g = gap between plates [L]

d_p^* = grain diameter [inch]

d_p = grain diameter [inch]

d_{pore} = pore diameter [inch]

d_{throat} = throat diameter [inch]

D = dispersion coefficient, [L^2/T]

D_o = molecular diffusion coefficient, [L^2/T]

D_T = transverse dispersion coefficient [L^2/T]

F' = formation electrical resistivity factor

F = force [N]

F_C = capillary force [N]

F_s = shear force [N]

F_T = inertial force in transverse direction [N]

F_G = gravity [N]

Fr = Froude number [dimensionless]

f_{we} = water cut at outlet (well) [fraction]

G = gravity number, dimensionless

G' = conductance [$cm^3/s/psi$]

g = gravity acceleration coefficient [ft/sec^2]

h = height [inch]

h_c = capillary height [inch]

h_d = dispersion height [inch]

h_{mv} = minimum visible height [L]

H = height of model [inch]

k = permeability [md]

K_L, K_T= longitudinal and transverse dispersion respectively, $[L]^2/[T]$

k_{dn} = dispersion slope

l = length (capillary segment) [L]

L = length of model [inch]

m = mass [lbm]

M = end-point mobility ratio [dimensionless]

n = flux [inch/s]

N_{CV} = transverse capillary number (time ratio), dimensionless

N_{CV}' = ratio of inertial and capillary force in vertical direction, dimensionless

N_{GV} = gravity number (time ratio), dimensionless

N_{GV}' = ratio of inertial and gravity force in vertical direction, dimensionless

N_{Pe}' = modified Péclet number, dimensionless

N_{VH} = transverse dispersion and oil layer ratio, dimensionless

p = pressure [psi]

p_b = static pressure at the interface [psi]

p_{osW} = shear force at the interface of the oil and the wall [psi]

p_{wsW} = shear force at the interface of the water and the glass wall [psi]

p_{sL} = shear force at the interface of the water and the oil [psi]

p_c^* = calculated capillary pressure [psi]

p_c' = critical capillary pressure [psi]

Q = flow rate [ft^3/s]

R_i = Richardson number, dimensionless

r = radius [L]

r_0 = dispersion starting point distance away from well [ft]

r_α = volumetric source/sink terms [$lbm/L^3/T$]

r_{gb} = glass bead's radius [inch]

r_{eff} = effective radius of cross-section area of snap off [inch]

r_n = distance away from wellbore [inch]

r_w = wellbore radius [ft]

r_{mixing} = mixing size [ft]

R_e = Reynolds number, dimensionless

s = the (complex) frequency variable, [$second^{-1}$]

S = saturation [fraction]

S_b = area of blob [L^2]

S_{or} = residual oil saturation [fraction]

S_{wi} = irreducible water saturation [fraction]

S_p = flow area of throat [L^2]

S_{pe} = effective flow area of throat [L^2]

S_{wooi} = water saturation at original water oil interface [fraction]

S_w = water saturation [fraction]

$\bar{S}_w$ = water saturation [fraction]

S_{we} = water saturation at outlet (well) [fraction]

t = time [second]

T = variable related to time for separation of variables [T]

u = flowing velocity [L/T]

U = Laplace transform of function S_w [second]

v = velocity [L/T]

v_{ro} = velocity at dispersion start point [L/T]

v_{wt} = transverse velocity of water [L/T]

V = volume [ft^3]

V_{mixing} = mixing fluid volume [ft^3]

v_T = interstitial velocity [L/T]

$WCT_{ultimate}$ = ultimate water cut [fraction]

W_e = weber number, dimensionless

W_{id} = pore volume of injected water, dimensionless

x, y = x and y distance in horizontal plane [L]

x_0 = coordinate of transverse mixing onset in linear flow [L]

X = a temporary variable in Chapter 9, dimensionless

Y = temporary variable in Chapter 7

z = transverse distance in vertical plane [L]

Z = variable related to z distance for separation of variables [L]

α = dispersivity, [L]

α = flow angle (after collision) in Appendix C [degree]

α' = immiscible dispersivity, [L]

β = flow angle in Appendix C [degree]

β = non-Darcy coefficient in Chapter 4 [L^{-1}]

γ = shear rate [T^{-1}]

θ = contact angle at interface [degree]

ξ = flow angle [degree]

κ = a temporary variable, [L^{-2}]

ϕ = porosity [fraction]

μ = viscosity [cp]

λ = wave length [L]

λ = a temporary variable in Chapter 9, [$second^{-1}$]

Φ = potential of any fluid [L^{-1}]

$(\Phi_w)_w$ = potential of the water [L^{-1}]

$(\Phi_o)_o$ = potential of the oil [L^{-1}]

ω = velocity angle deviated from center line [degree]

σ = interfacial tension [N/cm]

$\sigma^{э}$ = a measure of the heterogeneity of the porous pack

σ_{wW} = interfacial tension at water and glass wall surface, dynes/cm

σ_{oW} = interfacial tension at oil and glass wall surface, dynes/cm

σ_{wo} = interfacial tension at water and oil surface, dynes/cm

ρ = density [ft^3/lb]

$\Delta\rho$ = density difference between water and oil [ft^3/lb]

τ = shear force in Chapter 2, [psi]

τ = tortuosity in Chapter 4, dimensionless

Subscript

1 = horizontal direction

2 = downward direction

3 = upward direction

b = blob

down = downstream

h = horizontal direction

i = phase name

L = longitudinal direction

n = integer

o = oil

p = particles

r = radial direction

ro = oil relative

rw = water relative

so = snap off

v = vertical direction

T = transverse direction

up = upstream

w = water

wt = transverse water flow

x,y,z = x, y and z directions

x_1, y_1 = coordinate of the flow starting point

x_2, y_2 = coordinate of the flow ending point

TD = transverse dispersion

TM = transverse mixing

α = component of species

VITA

Shengkai Duan was born in Qianjiang City, China, in September, 1972. In July 1993, he received the degree of Bachelor of Science in Petroleum Engineering from the Xi'An Petroleum Institute, China. In August 1993, he joined China National Offshore Oil Corporation (CNOOC) Shanghai, Ltd., as an assistant reservoir engineer and was assigned to work on a composite geological research of East China Sea. In July 1998, he started to work as a reservoir engineer in charge of reservoir simulation and welltest analysis on Xihu and Taibei structures in East China Sea. In January 2002, he joined petroleum engineering department at University of Louisiana at Lafayette and received the degree of Master of Science in petroleum engineering. In August 2003, he joined the Craft & Hawkins petroleum engineering department at Louisiana State University. He is currently pursuing his study towards a doctoral degree in reservoir engineering. He is also a member of the Society of Petroleum Engineers.